DESIGN AND DEVELOPMENT OF A RADIO FREQUENCY ENERGY HARVESTER FOR LOW-POWER SENSORS

A THESIS SUBMITTED TO
THE BOARD OF CAMPUS GRADUATE PROGRAMS INFORMATICS INSTITUTE
OF
MIDDLE EAST TECHNICAL UNIVERSITY
NORTHERN CYPRUS CAMPUS

BY

HURİYE ÖZDEMİR

IN PARTIAL FULFILLMENT OF THE REQUIREMENTS FOR THE DEGREE OF
MASTER OF SCIENCE
IN
SUSTAINABLE ENVIRONMENT AND ENERGY SYSTEMS PROGRAM

JANUARY 2019

Approval of the Board of Graduate Programs

Prof.Dr. Gürkan Karakaş
Chairperson

I certify that this thesis satisfies all the requirements as a thesis for the degree of Master of Science.

Assoc.Prof.Dr. Ceren İnce
Program Coordinator

This is to certify that we have read this thesis and that in our opinion it is fully adequate, in scope and quality, as a thesis for the degree of Master of Science.

Assoc.Prof.Dr. Tayfun Nesimoğlu
Supervisor

Examining Committee Members

Prof. Dr. Sadık Ülker
Electrical and Electronics Engineering Dept.,
European University of Lefke

Assoc.Prof.Dr. Tayfun Nesimoğlu
Electrical and Electronics Engineering Dept.,
Middle East Technical University–Northern Cyprus Campus

Assoc.Prof.Dr. Volkan Esat
Mechanical Engineering Dept.,
Middle East Technical University–Northern Cyprus Campus

I hereby declare that all information in this document has been obtained and presented in accordance with academic rules and ethical conduct. I also declare that, as required by these rules and conduct, I have fully cited and referenced all material and results that are not original to this work.

Name, Last Name: HURİYE ÖZDEMİR

Signature :

ABSTRACT

DESIGN AND DEVELOPMENT OF A RADIO FREQUENCY ENERGY HARVESTER FOR LOW-POWER SENSORS

Özdemir, Huriye

M.Sc., Department of Sustainable Environment and Energy Systems Program

Supervisor : Assoc.Prof.Dr. Tayfun Nesimoğlu

January 2019, 136 pages

This thesis presents a systematic design and implementation of a rectenna. As a beginning, a receiving antenna is proposed. In the design of the receiving antenna, a fractal topology is utilized to widen the antenna bandwidth. Moreover, a rectifier circuit with a proposed dual-band matching technique is realized to aggregate the DC power. Ultimately, the broadband fractal antenna and the proposed dual-band rectifier circuit have been assembled to realize the rectenna. In addition, a simple RF spectrum study and a field measurement are conducted to obtain a better understanding of the available electric field density in the Middle East Technical University–Northern Cyprus Campus. Finally, the energy harvesting capability of the proposed rectenna has been verified in both controlled environment (laboratory) and ambient. As a result of the laboratory measurements, the proposed rectenna yields the highest RF-to-DC conversion efficiency of 51.9% when the total power density of the two tone signal is 11.1 μW/cm^2. As a result of the ambient measurements, the proposed rectenna features an open-voltage in the range of 195–417 mV in the ambient when the highest electric field densities are 4.137 V/m and 1.818 V/m from the standards of GSM-900 and 3G (UMTS), respectively.

Keywords: Electromagnetic energy harvesting, broadband fractal antenna, dual-band rectifier circuit, rectenna, RF spectrum measurements.

ÖZ

DÜŞÜK GÜÇTE ÇALIŞAN SENSÖRLER İÇİN BİR RADYO FREKANSI ENERJİ HASATLAYICI DEVRE TASARIMI VE GELİŞTİRİLMESİ

Özdemir, Huriye
Yüksek Lisans, Sürdürülebilir Çevre ve Enerji Sistemleri
Tez Yöneticisi : Assoc. Prof. Dr. Tayfun Nesimoğlu

Ocak 2019, 136 sayfa

Bu tez, bir doğrultucu antenin sistematik tasarımını ve uygunlamasını sunmaktadır. İlk olarak, alıcı antenin bant genişliğini arttırmak için fraktal topoloji ile tasarımına yer verilir. Bunun yanında, önerilen çift bantlı empedans uyumlaştırma özelliğine sahip bir doğrultucu devresinin tasarımı ele alınır. Son olarak, geniş bantlı alıcı anten ile önerilen doğrultucu devre enerji hasatlayıcı devreyi gerçekleştirmek için birleştirilir. Bunlara ek olarak, Orta Doğu Teknik Üniversitesi - Kuzey Kıbrıs Kampüsü'ndeki mevcut elektriksel alan yoğunluğunun belirlenmesi için yapılan ölçümler ve sonuçları sunulur. Önerilen doğrultucu anten hem laboratuvarda hem de dış ortamda bulunan RF sinyalleri ile test edilir. Laboratuvar ölçümlerinin sonucunda, doğrultucu antenin, iki ton RF sinyalinden gelen ve toplam güç yoğunluğunun 11.1 μW/cm^2 olduğu bir test düzeneğinde, sağlayabildiği en yüksek dönüşüm verimliliği % 51.9 olarak kaydedilmiştir. Dış ortamdaki ölçümler sonucunda, doğrultucu antenin elektriksel alan yoğunluklarının 4.137 V/m ile 1.818 V/m arasında değiştiği bir dış ortamda, 195 mV ile 417 mV arasında değişen yüksüz çıkış voltajı sağladığı kaydedilmiştir.

Anahtar Kelimeler: RF enerji hasadı, geniş bantlı fraktal anten, doğrultucu devre, elektromanyetik enerji hasatlayıcı, elektriksel alan ölçümü.

dedicated to my beloved Mom and Dad

ACKNOWLEDGMENTS

First and foremost, I would like to express my deepest gratitude and appreciation to my supervisor Assoc. Prof. Dr. Tayfun NESİMOĞLU whose support, patience and understanding have contributed considerably to my academic life as a graduate student. As my supervisor, He always provided me with intellectual freedom in my work and supported in all my endeavors, which of those have made this thesis possible. His valuable guidance and expert advice have been invaluable throughout all stages of this thesis. I am also thankful to him for teaching me many lessons when I was an undergrad student. Through his work-ethics, positive attitude, and professionalism, He sets an example of excellence as a mentor and researcher.

I would like to thank all the Professors in the Department of Electrical and Electronics Engineering of METU-NCC, their positive attitude and professionalism have contributed considerably to me as a graduate assistant.

I would like to thank my thesis committee members, Prof. Dr. Sadık ÜLKER and Assoc. Prof. Dr. Volkan ESAT, for reviewing my thesis.

I would like to extend my sincerest appreciation to Kemal Hoca (KILIÇ) for his valuable supports.

I would like to extend my sincerest gratitude to;

• Prof. Dr. Özlem AYDIN ÇİVİ, Feza Turgay ÇELİK and Damla ALPTEKİN for helping me in Middle East Technical University (Ankara Campus) Anechoic Chamber measurement.

• Elburuz KÖKSOY and Birol BAKAY for helping me in Information Technologies and Communication Authority (BTHK, Ankara) Anechoic Chamber measurement.

• Salih KOCADAL from The Information Technologies and Communication Authority (BTHK, Northen Cyprus) for helping me spectrum measurement in Middle East Technical University Northern Cyprus Campus (METU-NCC).

I acknowledge scientific research project under grant number of BAP-FEN-18-D-4 in Middle East Technical University Northern Cyprus Campus (METU-NCC) for funding my research.

I acknowledge Radio Frequency and Telecommunications Laboratory (RFTL) of METU-NCC.

Besides, thanks to all Marvel movies, especially Doctor Strange, for giving me endurance during my thesis.

Finally, but certainly not least, many thanks to my family for their endless love, supports and caring through all my life.

TABLE OF CONTENTS

LIST OF TABLES

LIST OF FIGURES

LIST OF ABBREVIATIONS

AC	Alternating Current
AUT	Antenna Under Test
BDR	Bandwidth Dimension Ratio
DC	Direct Current
DECT	Digital Enhanced Cordless Telecommunications
DUT	Device Under Test
EM	Electromagnetic
EMF	Electromagnetic Field
FBW	Fractional Bandwidth
GSM	Global System for Mobile Communications
HB	Harmonic Balance
HPBW	Half–Power Bandwidth
IBW	Impedance Bandwidth
IF	Iteration Factor
IoT	Internet of Things
IO	Iteration Order
ISM	Industrial, Medical, and Scientific
LSSP	Large Signal Scattering Parameters
LTE	Long Term Evolution
MN	Matching Network
RF	Radio Frequency
RFIDs	Radio-Frequency Identifiers
SC	Smith Chart
SMA	SubMiniature version A
SWB	Super–Wide Band
SMD	Surface-Mount Device
UHF	Ultra High Frequency
UMTS	Universal Mobile Telecommunications System
UWB	Ultra–Wide Band
WiFi	Wireless Fidelity
WPT	Wireless Power Transmission
WLAN	Wireless Local Area Network
ZBD	Zero Bias Detector

CHAPTER 1

INTRODUCTION

"Science is not a boy's game, it's not a girl's game. It's everyone's game. It's about where we are and where we're going... "

- Nichelle Nichols, *former NASA Ambassador and Star Trek actress*

1.1 Motivation for Present Research

The advancements in electronic systems not only have brought innovations but also have created energy demand. In order to meet growing energy needs, it seems non- renewable energy sources no longer could be used because of their damage to the environment that has motivated the researches to find clean and sustainable energy. The combination of these two notions; growing energy needs and clean & sustainable energy, have created a considerable amount of attention towards ambient energy (power) harvesting (scavenging). Harvesting and recycling of ambient energy have the potential to ensure the creation of sustainable and clean energy, also to develop low-profile and self-powered devices that may harvest energy from renewable sources such as solar, thermal and electromagnetic energy, etc. Between all these energy sources, this thesis will mainly focus on the energy harvesting from electromagnetic sources.

Since Nikola Tesla has proved the first wireless energy transmission through radio waves in the 1890s, he dreamed all devices requiring electrical energy would draw that energy from the ambient. Starting from the Teslas invention of Wireless Power Transmission (WPT) by radio waves, there has been a widespread interest for energy harvesting at Radio Frequency

(RF), covering signals ranging from 3 kHz to 300 GHz. Ambient RF/microwave energy is abundant in the environment as a result of growth in the broadcasting and wireless communication systems that can easily be found in our surrounding. Furthermore, power scavenging from ambient RF sources could be the alternative solution for the battery issues for the microsystems.

1.2 History of the Wireless Power Transfer

"If you want to find the secrets of the universe, think in terms of energy, frequency and vibration "

- Nikola Tesla, *Inventor of the Wireless Power Transfer*

The early history of power transmission by radio waves has begun with the experiment of Heinrich Hertz, which was the demonstration of the electromagnetic wave propagation at in free space. After the Hertzs experiments, Nikola Tesla has created his gigantic coil, called the Tesla coil. The purpose of the coil to transmit power wirelessly over long distances. The experiment of Tesla in Colorado Springs Laboratory has remained as a mystery because there is no specific record which indicates that how much of power generated from the gigantic coil was transmitted over the whether long or short distances or how much of the power was collected [1].

The attempts had continued towards the wireless power transmission, and there was a period, the interests in WPT had dropped because it has been noticed that only the significant amount of power transmission could be practically realized by using only electromagnetic energy with very short wavelengths. However, at that times, there was no device to generate an electromagnetic power at very short wavelengths, which profoundly has affected the experiments for WPT [1]. In the late 1930s, the developments of klystron tube and most importantly the microwave cavity magnetron had enabled to generate electromagnetic power (microwave power) at the desired wavelengths [2].

The microwave power generation has opened a period of the modern history of the free-space power transmission. The generation of the microwave power has gained significant attention since it has enabled not only to transfer power more efficiently but also to realize

several applications such as radar and communication systems [2].

During the modern history of the free-space power transmission period, many researchers and the companies have involved in the developments of the microwave power transmission to improve the amount of the transmitted power over the distance in an efficient way. For example, in the earlier period of the free-space microwave power transmission, a first complete microwave power transmission system was demonstrated at Raytheons Spencer Laboratory in May 1963. The Direct Current (DC) power of 100 W was successfully aggregated from the magnetron, providing 400 W of continuous wave power and then the retrieved DC power was utilized to power-up a DC motor. The overall DC–DC efficiency of the complete microwave power transmission system had been recorded as approximately 13%. The conversion of microwave power into a usable DC power has led the creation of the microwave-powered helicopter concept which was the first attempt to realize a wirelessly powered-up electronic platform. After many trials, the first rectifying antenna, known as rectenna, was built-up. The first rectenna consists of 28 half-wave dipole antennas, and each of the dipoles is connected to a bridge rectifier circuit including semiconductor diodes. The DC power of 7 W was collected from the first rectenna with the overall RF-to-DC conversion efficiency of 40%. In order to enhance the output DC power, the rectenna had been modified, and then the aggregated output power of 270 W was obtained from the rectenna, which was enough to actuate the helicopter rotor. As a result of the attempts, at the first time, in 1964, the flight of the microwave- powered helicopter had been achieved. It was the historical milestone of the conversion of the electromagnetic energy to a usable DC power [1].

After the first wirelessly powered-up electronic platform, the RF/microwave energy transfer and energy harvesting have gained significant attention over the years, as a result of this, there have been countless attempts and efforts which have carried out the idea of energy harvesting from the Microwave/RF signals.

1.3 Thesis Outline

The work embodied in this dissertation has been organized as follows:

Chapter 2 reviews a general structure of an Energy-Enabled Sensor Platform and provides a comprehensive comparison of the potential energy harvesting sources which can be exploited to produce a useful DC power to create a fully autonomous Energy-Enabled Sensor

platform. Furthermore, it reviews the related works which have been carried out to harvest RF energy. Finally, it gives a system level description of the RF energy harvester which is proposed in this work.

Chapter 3 presents a microstrip patch based fractal antenna. First of all, a detailed step-by-step design method is given in order to obtain a better understanding of the realization of a broadband antenna using a fractal topology. Next, a prototype of the proposed antenna is fabricated, and then the simulation results of the return loss, radiation pattern, and gain are validated with measurement results.

Chapter 4 provides a comprehensive review of a rectifying element, which is selected as Schottky-diode in this work. It compares the performance of the three different kinds of Schottky-diode, which are commonly exploited as a rectifying element in the literature. The laboratory measurements are conducted for the performance comparison of the Schottky-diodes which include the conversion loss, the RF-to-DC conversion efficiency, and the output DC voltage. Moreover, the simulations are carried out to enlighten the effect of a frequency, an input RF power, and a load resistance value on an input impedance of a rectifier circuit including Schottky-diode.

Chapter 5 presents a step-by-step design method for a dual-band matching network for a voltage doubler rectifier circuit. This chapter investigates and proposes a matching technique for a rectifier circuit. Finally, in this chapter, the voltage doubler rectifier circuit with the proposed matching network is fabricated, and then the performance of the rectifier circuit is discussed and verified with the measurements results.

Chapter 6 presents a rectenna which consists of the proposed fractal slotted antenna and the proposed rectifier circuit. In this chapter, first of all, the RF energy harvesting capability of the proposed rectenna is evaluated with the dedicated source. The aggregated output DC voltage is utilized to power-up a low power temperature sensor. Secondly, the available frequency bands and the feasibility of RF energy harvesting in METU NCC, Güzelyurt/Northern Cyprus is investigated with RF spectrum and electric field measurements. Finally, the performance of the rectenna regarding the DC output voltage is explored in the ambient.

Chapter 7 concludes the research done in this thesis, gives the contributions of the study and recommends some future works to enhance the rectenna performance.

CHAPTER 2

WIRELESSLY POWERED SENSOR PLATFORMS

"If you know you are on the right track, if you have this inner knowledge, then nobody can turn you off... no matter what they say "

- Barbara McClintock, *cytogeneticist and winner of the 1983 Nobel Prize in medicine*

2.1 Introduction

Wireless sensors are becoming pervasive with the developments of the Internet of Things (IoT) enabling the transformation of the sensors into the smart objects. Therefore, the wireless sensor network can be easily integrated into the so many different applications. The wireless sensors are exploited in such applications including; to control the current status of the patients in the health-care system [3], structural observations [4], to track the environmental activities [5]. Although the integration of the wireless sensor has been the subject of many application/area, the dependence of their powering-up operation to the batteries has still been a paramount obstacle for the creation of the fully-smart and autonomous objects.

Even there are a few exceptions, for example, passive and chipless Radio-Frequency Identifiers (RFIDs), the power-up operation of the active wireless sensors and IoT devices mostly depend on the batteries for data transmission and communication. Utilization of the batteries in the sensor structure creates troubles due to the fact that batteries have a limited life-span and their maintenance can be costly regarding the vast number of the sensor nodes in the sensor network. Therefore, recharging or replacing the batteries with an alternative energy source is a promising way to overcome the concerns about the power supply issue for the sensor platforms. As a consequence of this, the elimination or recharging of the batteries has brought up arise of the low-power energy demand. Scavenging and recycling of the ambient energy might be the solution for the low-power energy demand ans also they have the po-

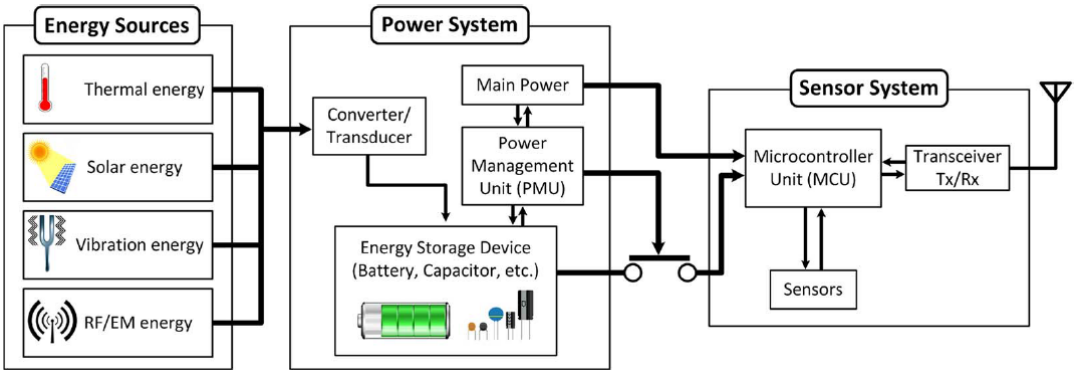

Figure 2.1: General block diagram of Energy-Harvesting-Enabled Wireless Sensor Platform system [7].

tential to ensure generation of sustainable and clean energy, also to develop low-profile and self-powered sensor platforms [6].

A typical block diagram of an Energy- Harvesting Enabled Wireless Sensor platform is depicted in Figure 2.1. In the system, a converter renders the ambient energy in the form of a usable DC power, and then the accumulated DC power is stored into a storage unit. The collected power is efficiently optimized to ensure a duty cycle optimization so as to actuate a micro-controller unit of a sensor and then the operation of the sensor system can be completed with the energy harvested from the ambient sources. Energy harvesting can be utilized to extend the lifetime of the battery which can be periodically recharged. Alternatively, instead of recharging the battery, it can be eliminated from the system by utilizing the harvested energy from the ambient/dedicated sources. As a result of the exclusion of the battery from the system, the sensor platform turns into a completely standalone (battery-less) autonomous operation [7].

2.2 Potential Energy Sources

In order to realize truly autonomous sensor platforms, there are many potential ambient/dedicated sources of energy such as solar, thermal, vibration/mechanical motion, and electromagnetic [8]–[10].

Solar energy is frequently preferred as an energy source, which features a relatively high power. It can generate a power density of 100 mW/cm^2 with the relative conversion efficiency of 15% in the daytime [11]. Although the photo-voltaic technology has improved in terms of usable output DC voltage, and conversion efficiency, however, it features relatively low

conversion efficiency of 2% – 8% in the indoor environment. Besides, as the aggregated amount of power from the solar energy highly depends on the size of the solar panel, therefore, in order to attain sufficient amounts of DC power from ambient solar energy, relatively large solar panel size might be required in the indoor environment. In addition to this, the power generated from the solar energy can be highly inefficient at night time or on a cloudy day [12].

Thermal energy is alternatively exploited as a source of energy. The operation principle of the thermoelectric devices is based on the Thomson effect or the Seebeck effect or in the thermoelectric material in which the temperature difference in the material generates electrical power [13]. The harvested power densities from the thermoelectric source are relatively low, and they merely alter in the range of 10 μW/cm^2 to 1 mW/cm^2. In reality, the thermoelectric effect has the advantage that a circuit voltage can be generated from the temperature difference from a mechanical condition or human body. Besides, it can also be exploited in wearable technologies such as temperature sensor, fitness bands, smart watches, health monitors [9]. As it is reported in [14], the textile covering thermopiles are integrated into human clothes and tested on the human body. As a result of this, the maximum power density of 60 mW/cm^2 in the indoor environment can be generated from a thermoelectric generator, in which the human body is used as the source of heat which is typically 37 ^oC while the ambient temperature is at between 15^oC–27 ^oC.

Vibration/Mechanical motion energy is one of the most commonly exploited sources of energy. Energy harvesting from the piezoelectric effect is based on mechanical strains which are intermittently repeated such as clicking a button, walking or regular motions such as wind and acoustic noises. The power densities of 2 mW and 8 mW can be harvested from typical piezoelectric sole and heel generators, respectively [15]. The harvested power density can be linearly boosted with increasing mechanical strain. For example, as it is reported in [16], the harvested power density of 0.8 W is approximately obtained from low-speed walking whereas the more power density of 1.115 W is acquired at higher speed walking from the piezoelectric transducers. Since the size of the piezoelectric energy harvesters is small and they are lightweight compared to the other kind of transducers, it has an advantage in terms of the integration to the sensors. However, the piezoelectric energy harvesters suffer form featuring a relatively low conversion efficiency due to the fact that the aggregated DC voltage from the piezoelectric transducers is relatively high whereas the generated current is low, which result in low conversion efficiency. Furthermore, due to the high voltage generated by the harvester, the voltage regulator is required to protect the circuitry from voltage overshoots [17].

Electromagnetic (EM) energy is another alternative source of power which can be harvested from both ambient and dedicated source for power up sensor platforms. According to the distance between transmitter and receiver, the electromagnetic energy sources can be separated into two forms: near-field and far-field RF energy harvesters [18].

Energy harvesting/transfer in *near-field* can be implemented if the distance between a transmitter and a receiver (or recharge device) is less than a wavelength of an RF signal. Magnetic resonance and EM induction methods are mostly utilized to produce a DC power so as to wirelessly (re)charge devices [19] – [21]. As it is reported in [22], the power levels of 43.2 (E-field) mW and 146.9 mW (H-field) are harvested by utilizing the electromagnetic energy from the two-way radio in the near field. The potential of the harvested power levels to power up a micro-controller communication and a LED module has been tested, and a full powering up operation of both modules has been achieved through energy transfer in the near field at the operation frequency of 464 MHz.

Energy harvesting in *far-field* can be realized if a transmitter and a receiver (or recharge device) are placed outside a distance of larger than a wavelength of an RF signal. The electromagnetic radiation in the far-field appears in the form of RF/microwave signals, which can be collected by a receiving antenna and then converted into a usable DC power by a rectifying circuit [23].

The intensity of RF/microwave power in the ambient varies between 10 nW/cm^2 –1 W/cm^2. The relatively low power densities of RF energy might be the main drawback of harvesting energy from electromagnetic sources. However, RF power is ubiquitously available in the ambient, due to the numerous wireless communication activities that show a growing trend over the years [2], [7]. In addition to this, RF energy harvester can be easily combined with alternative harvesters utilizing another source of energy such as kinetic energy [24] and solar energy [25] to enhance overall efficiency and an aggregated DC power from an energy harvester. Therefore, power harvesting from RF signals has become more attractive and feasible in powering up low-power sensors or charging a battery.

Since it is essential to optimize an RF energy harvester according to the available ambient power density levels and the existing signals at the wireless and communication frequencies, RF spectrum and power density measurements have been conducted over the frequency band from 300 to 3000 MHz in the suburban and urban areas of several cities [26]–[30]. In the current literature, the surveyed areas generally have been selected to identify the available frequency bands which are mostly encountered in the ambient and also to determine the power

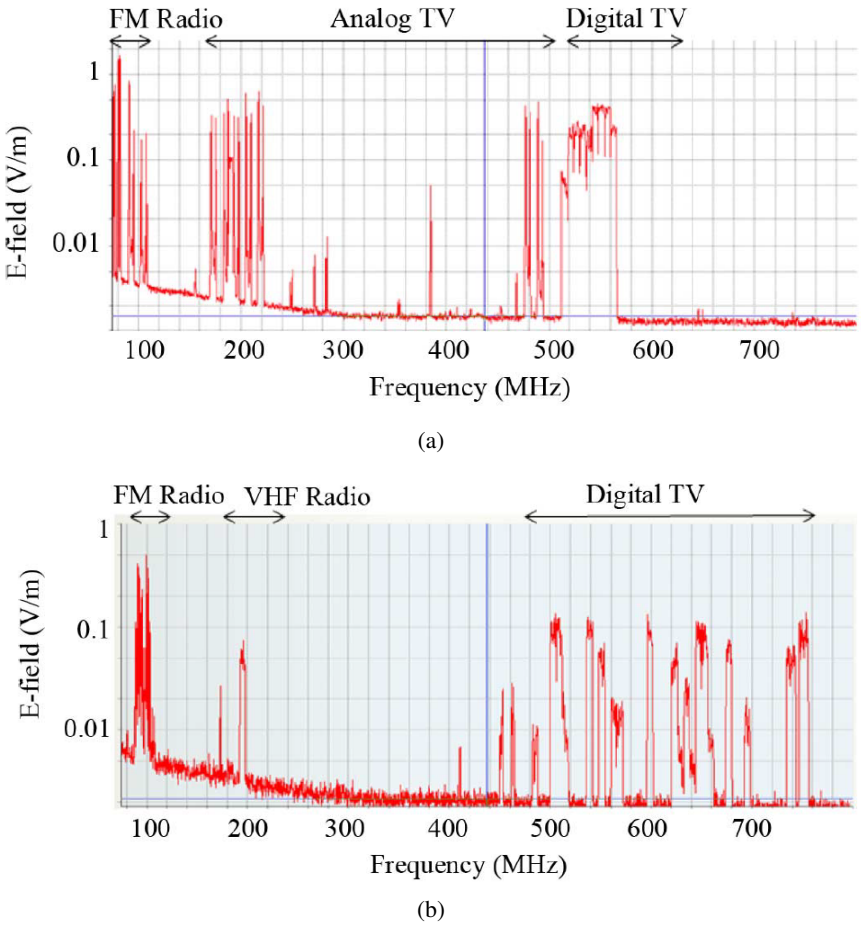

Figure 2.2: (a) Ambient wireless radiation measured in downtown Tokyo, Japan. (b) Ambient wireless radiation measured in Midtown Atlanta [26].

densities of the corresponding frequency bands.

In 2013, RF spectrum measurements covering the frequency range of standards of FM radio, analog-TV, and digital-TV signals were carried out in downtown Tokyo, Japan, and Atlanta, GA, USA [26] in peak workday hours. As it is shown in Figure 2.2, the highest EM radiation intensities are recorded over the frequency bands from 100 to 500 MHz and from 500 to 700 MHz corresponding to the standards of analog-TV and wireless digital-TV broadcasts, respectively.

In [27], a wide-RF spectral campaign was explored in London Underground stations at street level. In this work, the ultra high frequency (UHF) part of the RF frequency spectrum, covering the frequency band of 0.3–3 GHz has been selected. It can be seen from the Figure 2.3, the standards of DTV, GSM900, GSM1800, and 3G are the highest RF power density contributors in the urban and semi-urban environment.

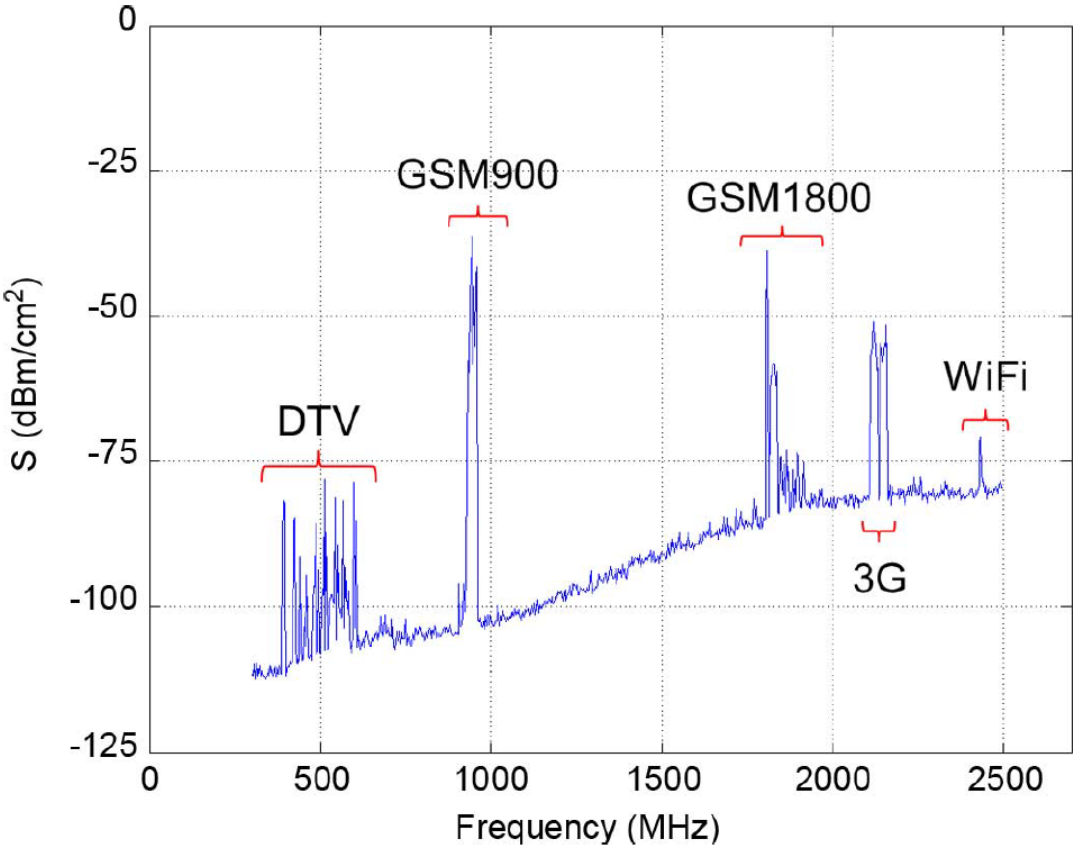

(a)

Band	Frequencies (MHz)	Average S_{BA} (nW/cm^2)	Maximum S_{BA} (nW/cm^2)
DTV (during switch over)	470-610	0.89	460
GSM900 (MTx)	880-915	0.45	39
GSM900 (BTx)	925-960	36	1,930
GSM1800 (MTx)	1710-1785	0.5	20
GSM1800 (BTx)	1805-1880	84	6,390
3G (MTx)	1920-1980	0.46	66
3G (BTx)	2110-2170	12	240
WiFi	2400-2500	0.18	6

(b)

Figure 2.3: (a) Input RF power density measurements outside the Northfields London Underground station. (b) Summary of London RF survey measurements [27].

Available power density (dBm/cm^2) per band and scenario										
DTV	GSM-R		GSM900		GSM1800		3G		DTV/ GSM900	GSM1800/3G
	MTx	BTx	MTx	BTx	MTx	BTx	MTx	BTx		
Commuting by foot										
−94.7 (−85.4)	−119.3 (−105.6)	−115.9 (−97.8)	−97.1 (−82.4)	−62.6 (−51.1)	−110.7 (−93.2)	−69.4 (−57.9)	−90.6 (−72.5)	−68.4 (−58.9)	−62.6	−65.9
Driving around Bristol										
−83.1 (−65.7)	−121.8 (−103.2)	−103.4 (−82.9)	−105.9 (−87.2)	−59.0 (−39.4)	−108.7 (−86.9)	−79.9 (−65.9)	−93.9 (−73.9)	−72.7 (−58.1)	−58.0	−71.9
Commuting by car										
−95.0 (−81.2)	−126.8 (−112.1)	−95.2 (−81.0)	−109.0 (−98.0)	−70.5 (−59.5)	−104.2 (−88.8)	−75.7 (−64.7)	−110.9 (−97.0)	−68.5 (−54.6)	−70.2	−67.7
Commuting by foot/train										
−93.5 (−80.8)	−110.7 (−89.4)	−72.9 (−51.5)	−57.3 (−36.2)	−49.4 (−28.6)	−75.0 (−51.6)	−70.3 (−56.3)	−74.7 (−54.9)	−65.4 (−53.4)	−48.7	−63.5

(a)

Scenario	Duration (h:mins:s)	Average energy, µJ		Total collected energy, mJ	
		DTV/GSM900	GSM1800/3G	DTV/GSM900	GSM1800/3G
walking	0:27:11	0.66	0.31	1.10	0.51
car	0:25:28	0.12	0.20	0.18	0.32
drive loop	1:33:43	1.91	0.84	8.90	0.36
train	1:17:11	16.20	0.54	73.68	2.51

(b)

Figure 2.4: (a) Summary of average and peak power (in brackets) densities measured in the different scenarios. (b) Total energy collected with an antenna having 1.2 m^2 effective area in the different scenarios [29].

Interesting research which explores the RF field measurements in dynamic conditions such as walking, traveling on a train and in a car has been conducted, in 2016, around Bristol, UK [29]. In this work, the frequency band from 500 MHz to 3 GHz has been selected to quantify available RF power density in the ambient. In Figure 2.4, a summary of the averaged RF power densities from different frequency bands in the various realistic and dynamic scenarios and the total accumulated energy by utilizing an antenna having an effective area of 1.2 m^2 are listed. As seen from the results, the highest RF power intensity was observed from the DTV/ GSM 900 standard while traveling by train/foot. Besides, as it is reported, the train scenario features the highest energy of 73.68 μJ that can be collected from the frequency band from 0.88 to 0.96 MHz corresponding to the standard of DTV/ GSM 900.

In [30], a wide-RF spectral campaign was explored in different locations such as station entrance, within the university, museum, subway, park and concert theater, and shopping center within Boston, in 2018. In this work, the RF frequency spectrum, covering frequency band from 0.3 to 3 GHz has been selected. It is targeted to identify and to quantify the power densities from the standards of LTE 730, LTE 740, GSM 850. The highest and the lowest ambient RF power levels in dBm are reported in Figure 2.5 as it can be seen from the results, LTE and GSM frequencies contribute mostly in the RF power levels in the environment.

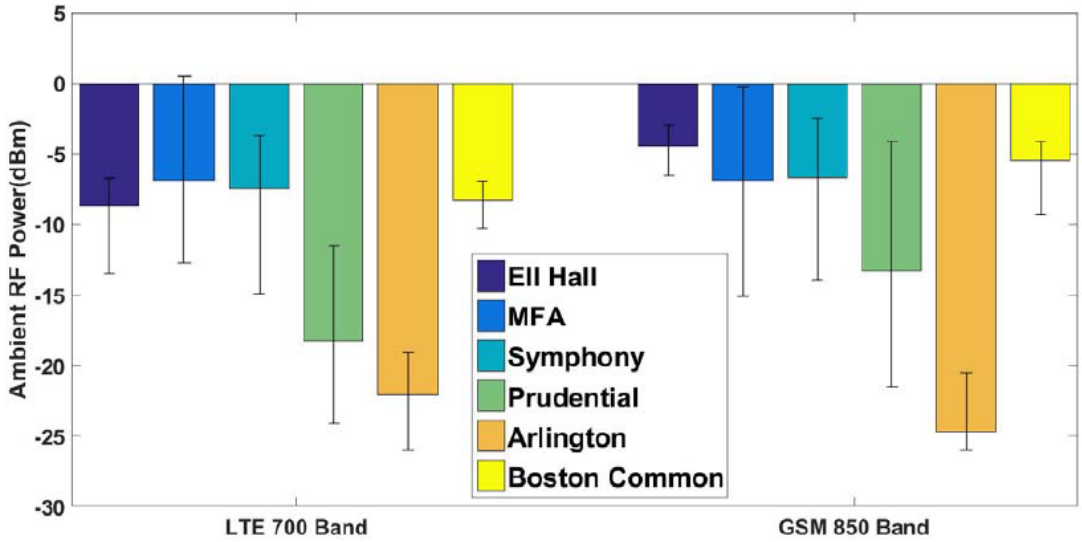

Figure 2.5: Levels of average RF power at subway stations, universities, museums, shopping centers, and parks in Boston [30].

2.3 System Level Design

In this work, the systematic design and development of an RF energy harvester are explored. The proposed RF energy harvester is a single element of integrated antenna-rectifier, which is called "rectenna" or rectifying antenna" in the current literature. The energy harvesting capability of the proposed rectenna is investigated with the incident RF power densities less than 15 μW/cm^2.

The block diagram of the proposed rectenna in this work is illustrated in Figure 2.6. In the first stage; a broadband fractal antenna has been designed to receive arbitrary polarized RF signals. Therefore, in the design of the proposed antenna, it is targeted to collect and harvest RF energy from all available bands both in up-link and in down-link which are given as

- GSM 1800 (Worldwide) U[1] : 1710-1785 MHz D[2] : 1805-1880 MHz
- Universal Mobile Telecommunications System (UMTS)/3G (Most countries) U: 1920-1980 MHz D: 2110-2170 MHz
- Wireless local area network (Wi-Fi) and Industrial, medical, and scientific bands (ISM) (Most countries) 2.400-2.484 GHz

In the second stage; since the coming RF signals from the proposed antenna are in the form of Alternating Current (AC), therefore; the broadband antenna is connected to the proposed

[1] Uplink (mobile-to-base)
[2] Downlink (base-to-mobile)

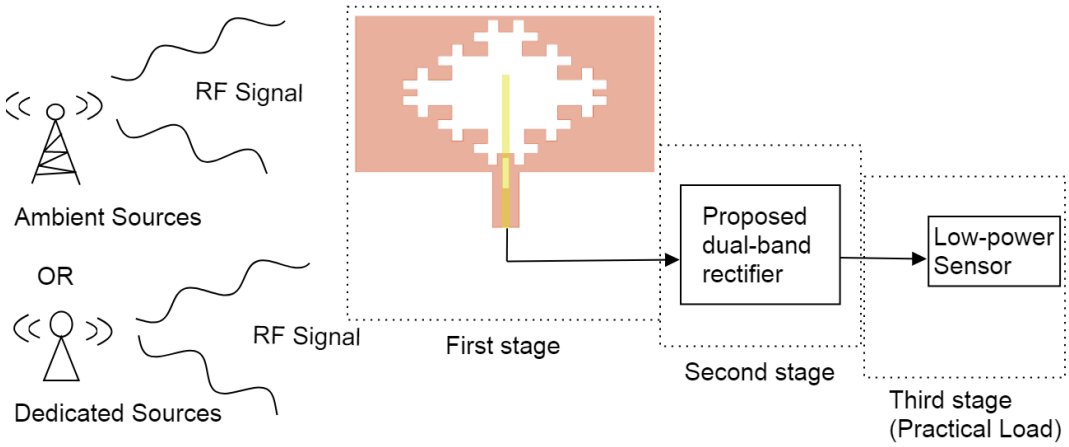

Figure 2.6: The block diagram of the proposed RF energy harvester (Rectenna).

dual-band rectifier circuit to convert the AC signals into a usable DC signal. The proposed rectifying circuit is optimized at a relatively low power level. In this work, "relatively low" power level refers to less than -10 dBm of available RF power at the input of the rectifier circuit. In the last stage, the aggregated DC power at the output of the rectifier is utilized to power-up a low-power temperature sensor (practical load).

2.4 Related Works

Table 2.1 summarizes some of the reported works of RF energy harvesting utilizing a rectenna in the current literature. It is important to notice that the RF-to-DC efficiency of the rectenna given in the papers is listed; however, it is difficult to compare them directly due to the different substrate exploited in the design of both antenna and rectifying circuit, different rectifier circuit topology and technology, and different optimal load values.

Table 2.1: Related works

Ref. (**Year**)	**Antenna Type**	**Rectifier topology** & **Technology**	**Rectenna efficiency (%) @ power available power level at operating frequency**	**Optimal Load value** (Ω)
31 (2011)	Single band at 2.45 GHz	Single series & HSMS2860	63 @ 0.525 mW/cm^2 at 2.45 GHz	1600
32 (2002)	Single band at 5.8 GHz	Single series & MA4E1317	80 @ 100 mW at 5.8 GHz	250
33 (2013)	Dual– band at 915 MHz & 2.45 GHz	Dual–band @ 915 MHz & 2.45 GHz single series & SMS7630	37 @ 1 mW/cm^2 at 915 MHz 20 @ 1 mW/cm^2 at 2.45 GHz	2200
34 (2007)	Dual– band at 2.45 & 5.8 GHz	Dual–band @ 2.45 & 5.8 GHz single series & MA4E1317	65 @ 10 mW/m^2 at 2.45 GHz 46 @ 10 mW/cm^2 at 5.8 GHz)	51.3
35 (2013)	Covering from 1.8 to 2.2 GHz	Dual–band @ 1.8 & 2.45 GHz single series & SMS7630	40 @ 455 μW/cm^2 at 1.8 & 2.45 GHz (dual-tone)	5000
36 (2017)	Triple–band at 900 MHz & 1.8 and 2.1 GHz	Triple–band @ 900 MHz & 1.8 & 2.1 GHz single series & SMS7630	40 @ 500 μW/m^2 at 900 MHz & 1.8 & 2.45 GHz (three-tone RF signal)	10000
37 (2015)	Broadband antenna 0.55 to 2.5 GHz	Four–band @ 900 MHz 1.8, 2.1 & 2.45 GHz voltage doubler & MSS20-141	84 @ 8 μW/cm^2 at 900 MHz & 1.8 & 2.1 & 2.45 GHz (four-tone RF signal)	11000
38 (2016)	Broadband antenna 0.9 to 3 GHz	Six–band @ 550, 750, 900 MHz & 1.85, 2.15 & 2.45 GHz voltage doubler & SMS7630	13 @ 13.6 dBm at 550, 750, 900 MHz & 1.85, 2.15 and 2.45 GHz (six–tone RF signal, indoor condition)	10000–75000
This Work (2019)	Broadband antenna 1.8 to 2.5 GHz	Dual–band @ 1.8 and 2.45 GHz voltage doubler & HSMS2850	51.9 @ 11.1 μW/cm^2 at 1.8 and 2.45 GHz (two–tone RF signal)	1200

CHAPTER 3

FRACTAL ANTENNA DESIGN

"I am happy to be here... "

- Rajeshwari Chatterjee, *One of the First Women Engineer in field of Microwave and Antenna.*

3.1 Introduction

In RF energy harvester, the receiving antenna is an essential element as it is responsible for capturing RF signals from the nearby EM radiating sources. Collecting of the available RF signals from the different sources is crucial to increase the amount of the aggregated DC power at the output of the energy harvester. Therefore RF energy harvester antenna is required to cover all the desired frequency bands with fairly stable radiation pattern and to feature an agreeable gain over the frequency bands. Furthermore, a dual polarization characteristic is another desired feature of the RF energy harvester antenna which should be able to receive RF signals with either horizontal or vertical polarization. In this work, microstrip technology will be exploited in the design of the receiving antenna.

A microstrip patch antenna is commonly exploited in various applications due to low cost, ease of integration to other systems, ease of manufacturing, and low profile. Therefore, microstrip antenna is emerged as an attractive candidate for many different application areas such as mobile communication [39], [40], RFID applications [41], [42], and medical application/telemetry [43]–[45].

The design of the RF energy harvester antenna is a challenging issue to meet the requirements of relatively high gain, dual-polarization, wide impedance bandwidth. In this work, it is aimed to widen the impedance bandwidth of the receiver antenna to cover the most frequently encountered frequency bands are situated around 1800/1900 MHz, 2.1 GHz, 2.4 GHz, 2.45

GHz while keeping the overall antenna size as small as possible.

Various designs and attempts to enhance impedance bandwidth ($S_{11} < 10$ dB) of the antenna with an agreeable radiation pattern and gain have been explored in the current literature such as combining a supersubstrate with microstirp patch antenna [46]–[48], utilizing different resonance modes [49], introducing T-shaped stub [50], loaded stripline [51], and a stepped slotline [52], employing a dielectric loaded structure in a microstrip antenna [53], combining a parasitic element with etched slot line [54]–[56].

Except for the mentioned techniques, etching out a wide slot from the ground plane is an attractive and commonly exploited method to improve the bandwidth of the antenna. Various kinds of wide slots etched out from microstrip patch fed by a coplanar waveguide, or microstrip line have been proposed in the literature. Bandwidth enhancement has been achieved by employing a wide rectangular slot [57], or different slot shapes like triangle or semi-circle [58]-[60].

It is noticed worthy; aforementioned conventional wide slot antennas have achieved a good impedance bandwidth at around the frequency band from 1.8 to 2.5 GHz. Since the dimensions of the antenna profoundly depend on the operation frequency, their overall dimensions change in the range of 85×85 mm to 110×110 mm for the frequency band from 1.8 to 2.5 GHz. However, it might be required to keep the antenna size as small as possible so that it can be conveniently assembled with a wireless sensor platform. Therefore, in order to widen the bandwidth of an antenna while maintaining the size of it, fractal geometry has emerged as a convenient way. Since the space-filling property renders size reduction and the self-similarity property of fractal geometries leads to a broadband or multi-band performance.

In this work, to realize a compact receiver antenna with an agreeable gain, radiation pattern, and dual-polarization over the frequency band, a fractal shape slot is etched out from the antenna ground plane and then the proposed fractal antenna is implemented on a substrate, and finally, the performance of the antenna is verified with the measurements.

3.2 Design Flow for the Fractal Antenna

The steps to success in creating a practical and efficient energy harvester antenna on a substrate are shown in Figure 3.1. The systematic flow of the fractal antenna design will be explained in shortly as includes:

1. Design Initials:

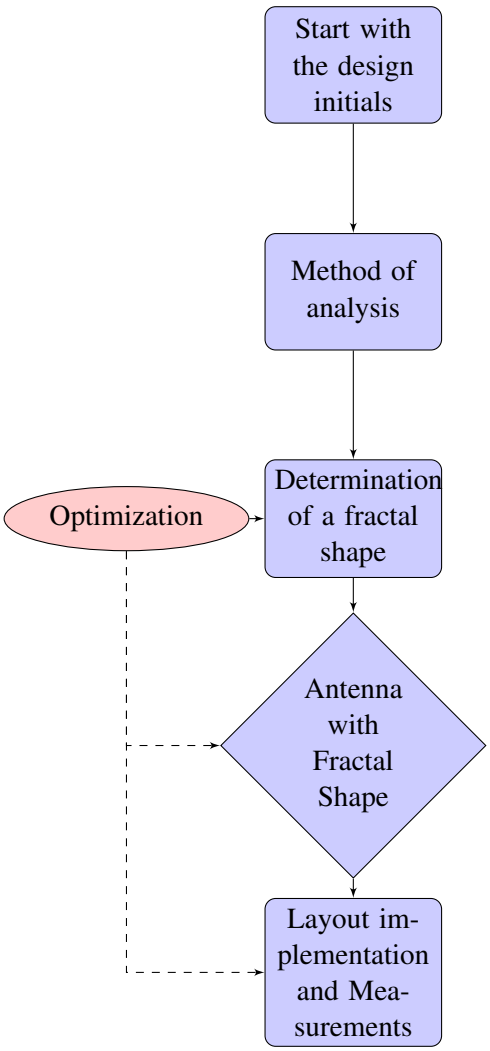

Figure 3.1: Illustration of the design flow for the fractal antenna.

Design initials for the antenna design refer to the substrate and the operating frequency of the energy harvesting antenna. Microstrip antennas can be implemented on a various type of substrates, and their dielectric constants mostly vary in the range of $2.2 \leqslant (\epsilon_r) \leqslant 12$. Selection of the substrate plays an essential role in the performance of the microstrip antenna, a good performance from the antenna can be achieved when the substrate is thick having a relatively lower dielectric constant, in the lower edge of the given range. The implementation of the microstrip patch on such substrate provides a good radiation efficiency, wider bandwidth, and further bound fields are restricted loosely for radiation into space; however, such a substrate is penalized with giving a larger microstrip patch size. In addition to this, thin substrates having relatively high dielectric constants feature smaller patch size at the expense of low radiation efficiency, less bandwidth and closely bound fields, which is more suitable for the microwave circuit in which the radiation from the circuitry is undesired [61].

Due to the fact that the energy harvesting antennas are commonly integrated with the rectifier circuitry, both the antenna and the microwave circuit performance should be compromised to ensure an agreeable performance from the energy harvester (rectenna). In this design, Rogers-4003 is selected as a substrate for the proposed fractal antenna. It has a height (h) of 0.8 mm and relative dielectric constant (ϵ_r) of 3.8 and loss tangent (δ) of 0.0035.

2. Method of analysis:

The development of analytical models to acquire a better insight into the performance of the microstrip antenna is an essential step for the design. There are different kinds of analysis method for the patch antennas, the methods which are mostly followed for the realization of the microstrip antennas are given as [61]:

1. Transmission Line Model

2. Cavity Model

3. Full Wave Models

The Transmission Line Model is the simplest model compared to the other models, and it provides a possible physical understanding however whose accuracy is less than the other methods. There is an alternative to the transmission line model which is the Cavity Model, it can also be exploited to obtain more accurate results. In addition to a good physical understanding; however, it is somewhat complicated. Moreover, The Full Wave Models are more confident, very sophisticated, and they can be utilized for the analysis of arbitrary shapes or single patch elements, infinite and finite antenna arrays, and coupling. Even they feature more certain results for the radiation pattern of the microstrip antenna, they suffer from complexity

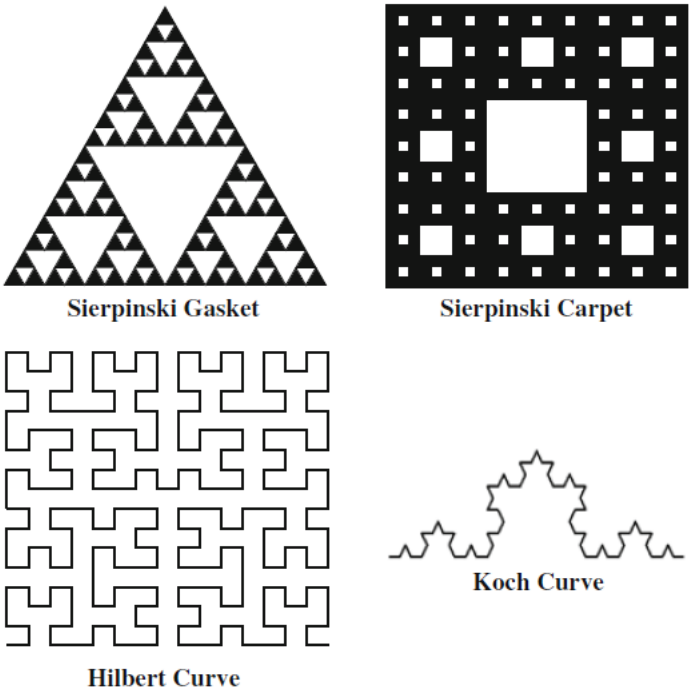

Figure 3.2: Geometry of the well- known fractal shapes [63].

and giving less physical insight [61].

In this design, the cavity model is selected, therefore in the next section, the cavity model is briefly explained so as to obtain the physical dimensions of the proposed antenna initially.

3. Determination of a fractal shape:

The locution of the *fractal* antecedently coined by a well-known mathematician "Benoit Mandelbrot," the meaning of the fractal term is used to break and to create a family of irregular or regular fragments. The complex, self-similar, and convoluted geometries (or patterns) in the nature such as mountains, leaves, trees, snowflakes, clouds, the boundary of cauliflower shape are delineated by using fractal theory [62].

The fractal shapes have been adopted in many areas of engineering and science, one of such branches is electromagnetic engineering. The combination of a fractal shape and electromagnetic theory has attracted attention and led to a several class of scattering, propagation, and radiation from the fractal boundaries which have been still investigating to realize new and promising design schemes for a wide variety of applications. There are some applications in electromagnetic in which fractal theory is exploited such as fractal frequency selective surfaces and filters, fractal electromagnetic band gap structures and high impedance surfaces,

and fractal antenna elements. Recently, the features of a fractal shape such as space filling and self-similarity have gained a lot of attention. The unique properties of the fractal shapes can render an antenna with either wide-band operation and compact size, and further, they can enhance the directivity and gain of an antenna [63].

The well-known fractal shapes mostly exploited in the realization of the antenna design are shown in Figure.3.2. Except for those shapes, a tremendous number of fractal geometries can be generated by using unique features of a fractal shape. However, complicated and convoluted shapes may be a restriction for the fabrication of the antenna. Milling/cutter machines might not be precise while cutting very complex fractal shapes, and a failure in a fractal shape on antenna may result in degradation in the antenna characteristics such as input impedance bandwidth, radiation pattern.

In this design, by considering the fabrication of the antenna with the milling machine, a fractal shape is proposed which is initially similar to the Minkowski fractal.

4. Simulation: As it is mentioned previously, to acquire a better understanding of the radiation mechanism of the microstrip antenna, commercially available *Momentum 3D Planar EM Simulator* from the *Keysight Technologies* which combines full-wave and quasi-static EM solvers is utilized.

5. Layout implementation and measurements: LPKF ProtoMat Milling Machine is used to implement the proposed antenna on Rogers-4003C (PCB board). The reflection characteristic is measured by a R&S ZVB8 Vector Network Analyzer. Both far-field pattern and gain of the proposed antenna are measured in an anechoic chamber.

6. Optimization: Since there is no accurate formula for the realization of the antenna with a fractal shape, therefore optimization is an essential part of the design flow starting from the simulation step. Optimization of each length & width of the dimension of the microstrip antenna have been carried out by means of ADS EM solver from *Keysight Technologies*.

3.3 Fractal Antenna Design

3.3.1 Cavity Model- Determination of the Structure of the Antenna

Microstrip antennas conventionally consist of a metallic patch at the top, a ground plane at the bottom, and a dielectric substrate at between the patch and the ground plane as it is shown in Figure.3.3.(a). Since the dielectric substrate is bounded by electric conductors above and below, microstrip antennas resemble *dielectric-loaded cavity*. Therefore, the cavity model

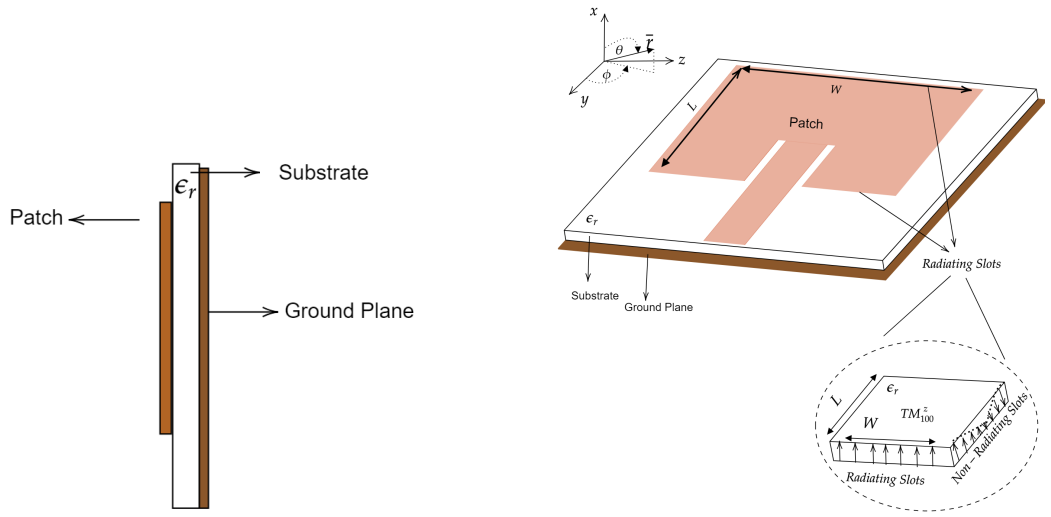

(a) (b)

Figure 3.3: (a) The side view of the microstrip patch antenna (b) The top view of the microstrip patch antenna.

approximation is exploited to evaluate the configuration of the normalized fields within the dielectric and the electric conductor. However, if the microstrip antenna is treated as a lossless cavity, it can not radiate into space. Therefore, in order to make the dielectric-loaded cavity representing an antenna, it is treated as a lossy cavity. Conduction (R_r) and radiation resistances (R_L) are taken into account for the determination of the input impedance of the antenna to make the microstrip antenna similar to a lossy cavity. Furthermore, the microstrip antenna possesses an effective loss tangent, δ_{eff} and a quality factor, Q (δ_{eff}=1/Q) representing the loss mechanism [61].

For the cavity shown in Figure 3.3.(b) which has the bottom and top walls are perfect electric conductor in which the tangential electric fields vanish. In the same manner, the four side walls along the perimeter of the cavity are treated as a magnetic wall, and the tangential magnetic fields vanish along the side walls. Besides, the given model for the cavity is considered while modeling the rectangular microstrip antenna so as to describe the field configurations. Since the height of the substrate is less than a wavelength within the dielectric region,(h « λ_g), the only TM^z field configuration is supported within the cavity [61].

The electric and magnetic field configurations within the cavity shown in Figure 3.3.(b) are associated with the vector potential function, A_z which must satisfy Helmholtz's (or homogeneous vector wave) equation of [61]

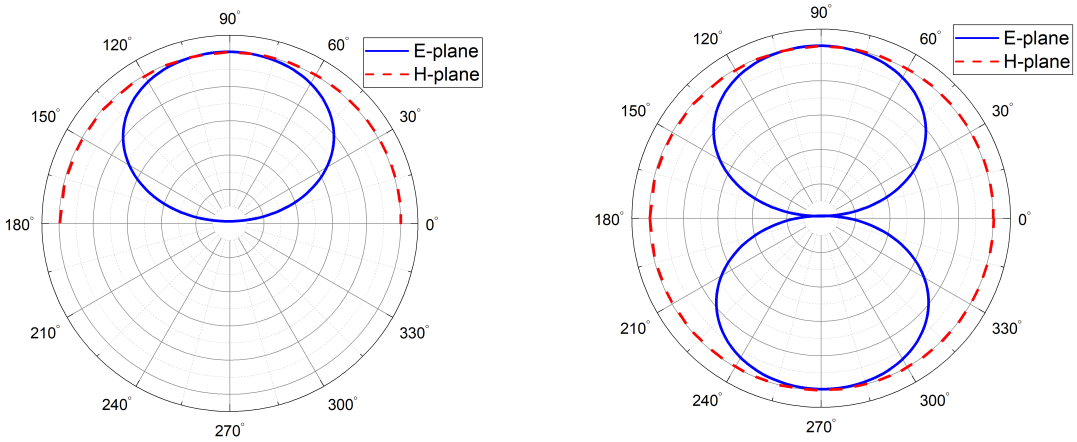

Figure 3.4: The representative illustration of (a) a unidirectional radiation pattern (b) a bidirectional radiation pattern.

$$\nabla^2 A_x + k^2 A_x = 0 \tag{3.1}$$

Both the electric and magnetic field configurations within the cavity can be evaluated with the vector potential function and then corresponding wave numbers and the resonant frequencies of the corresponding TM^z mode can be determined by the boundary conditions. If the boundary conditions are considered for the plane configuration shown in Figure 3.3.(b), the final form of the resonant frequencies for the TM^z mode of the cavity are written as [61]

$$(f_r)_{mnp} = \frac{1}{2\pi\sqrt{\mu\epsilon}}\sqrt{(\frac{m\pi}{h})^2 + (\frac{n\pi}{L})^2 + (\frac{p\pi}{W})^2} \tag{3.2}$$

The four sidewalls of the microstrip patch antenna as shown in Figure 3.3.(b) are characterized as four narrow slots (apertures) in which the fields mainly radiate from each slot. By using the Hygen's principles (the equivalence principle), the equivalent magnetic current density M_s and the equivalent electric current density J_s can be written as given [61]

$$\overline{M_s} = -\vec{n} \times \overline{E} \tag{3.3}$$

$$\overline{J_s} = \vec{n} \times \overline{H} \tag{3.4}$$

In general, the radiation from the slots arises due to the presence of both the magnetic currents and electric current, alternatively, either the magnetic current or electric current on

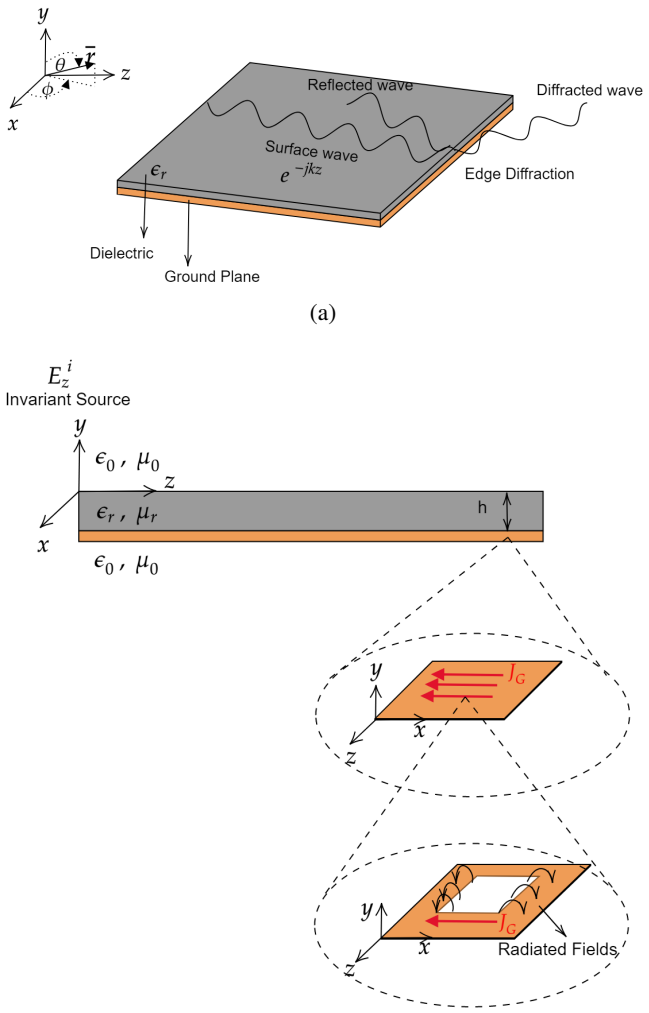

Figure 3.5: The geometry of a dielectric slab waveguide (a) top view (b) side view.

the boundary of the slots [64] as shown in Figure 3.3.(b). In both cases, if the current densities are the phase reversal along the corresponding slot, the broadside radiation pattern is formed in both principal E- plane and H- plane as indicated in Figure 3.4.(a). Since the presence of the ground plane on the other side of the radiating slots, a unidirectional radiation pattern can be realized only one side of the antenna plane (Refer to Figure 3.4.(a)). Since RF signals may be required to be received from both sides of the antenna, for the energy harvesting antenna, the formation of a radiation pattern is mostly desired to be similar to a bi-directional radiation pattern as shown in Figure 3.4.(b). Therefore a dielectric covered ground plane is chosen as an initial geometry of the proposed antenna to achieve a bi-directional radiation pattern. The geometry of the dielectric covered ground plane is shown in Figure 3.5.

The grounded dielectric slab consists of a semi-infinite ground plane and a dielectric which is known as *Surface wave antenna or dielectric radiator*. As shown in Figure 3.5.(a), the surface waves propagate along the ground plane without radiation into space, and then they diffract from the edge of the ground plane. However, if a traveling surface wave along the dielectric slab is disturbed with a discontinuity, it can be configured into a radiated space wave (Refer to Figure 3.5.(b)) [65], [67]. In order to acquire a better insight, first of all, a truncated grounded dielectric slab shown in Figure 3.5.(b) is examined. A lossless dielectric material with a thickness of h and dielectric permittivity of ϵ_r is covered uniformly with a flat ground plane that is placed at only one side of the dielectric. By considering given rectangular coordinate system which is introduced to the dielectric slab as shown in Figure 3.5.(b), it is assumed that the semi-infinite dielectric coated ground plane is excited by an invariant source creating only an incident electric field along $\mp z$ direction. Therefore it is assumed that the waves are propagating only $\mp z$ direction. Besides, to simplify the analysis into a two dimension, it is considered that there is no variation at the direction of $\mp x$ (length in the direction of x is infinite). Therefore, TM^z field configuration is considered inside the dielectric slab waveguide [66].

The electric and magnetic field distribution within and outside dielectric slab can be found through vector potential function A_z. The corresponding A_z given in detailed in [66] is solved by enforcing the boundary conditions that (according to the continuity of the tangential electric and magnetic field) can be summarized and written as $E_x = H_y = H_z = 0$.

From the solution of the A_z, the cutoff frequency for a TM_m^z mode given as [66]

$$f_{c(m)} = \frac{m}{4h\sqrt{\mu_r\epsilon_r - \mu_0\epsilon_0}} \quad m = 0, 2, 4... \tag{3.5}$$

It is apparent that the cutoff frequency of a mode depends on height of the dielectric slab and its electrical constitutive parameters.

From the solution of the A_z, an impedance of the dielectric slab can be evaluated as given [66]

$$Z^{-y} = -\frac{E_z}{H_x} \tag{3.6}$$

It is apparent from (3.6), the impedance of the dielectric slab is inductive which shows that TM^z mode surface waves are supported by inductive surface [66].

Since the dielectric slab supports surface wave propagation and conventional plane surface

waves do not radiate along the constant surface reactance [67] until they reach to end of the ground plane. Therefore to obtain radiation from the dielectric slab, the magnetic field along the direction of $\mp x$ can be varied.

It is apparent that by varying the magnetic field H_x along the direction of $\mp x$ (Refer to Figure 3.5.(b)) includes two contributions;

1) The surface current J_G due to the magnetic field can be disturbed, and then plane surface waves can be transformed into radiated space waves at the boundary of the discontinuities.

2) The impedance/reactance of the dielectric slab can be controlled (Refer to equation 3.6) by altering the stored magnetic and electric energies. As a result of this, the resonance frequency of the cavity can also be adjusted.

It is aimed to ensure the formation of bi-directional radiation from the dielectric slab, a wide slot as shown in Figure 3.5.(b) is introduced on the ground plane. The wide slot is excited by the surface waves, and the slots edges (boundaries) create a discontinuity as shown in Figure 3.5.(b) resulting in radiation from the slots similar to the radiating slots of the rectangular microstrip patch antenna. However, on the contrary to the conventional rectangular microstrip antenna, since one side of the radiated slots is covered with air and the other side of it is coated by both a dielectric and air, a bi-directional radiation pattern can be obtained from the grounded dielectric slab with a wide slot on the ground plane.

In addition to the bi-directional radiation pattern formed by a wide slot, the resonance frequency and correspondingly Q-factor of the cavity can be varied with additional slots on the ground plane which alters the electric current of J_G along the direction of $\mp x$.

The effect of the slots on the resonant frequency and the Q-factor of the dielectric slab can be explained by the perturbation of the cavity wall. In the light of the knowledge given in [68], it is assumed that Figure 3.6.(b) represents a resonant cavity formed by a conductor covering S and enclosing the loss-free region τ. Figure 3.6.(c) shows that a deformation on the original cavity and a conductor covers $S' = S - \Delta S$ and encloses $\tau' = \tau - \Delta\tau$.

It is assumed that $\overline{E_0}$, $\overline{H_0}$ and ω_0 represent the fields and the resonant frequency of the unperturbed cavity (original cavity, Refer to Figure 3.6.(b)) and $\overline{E_p}$, $\overline{H_p}$ and ω_p are the the fields and the resonant frequency of the perturbed cavity as shown in Figure 3.6.(c).

The fractional change in the resonant frequency due to the change in the cavity wall is expressed as [68]

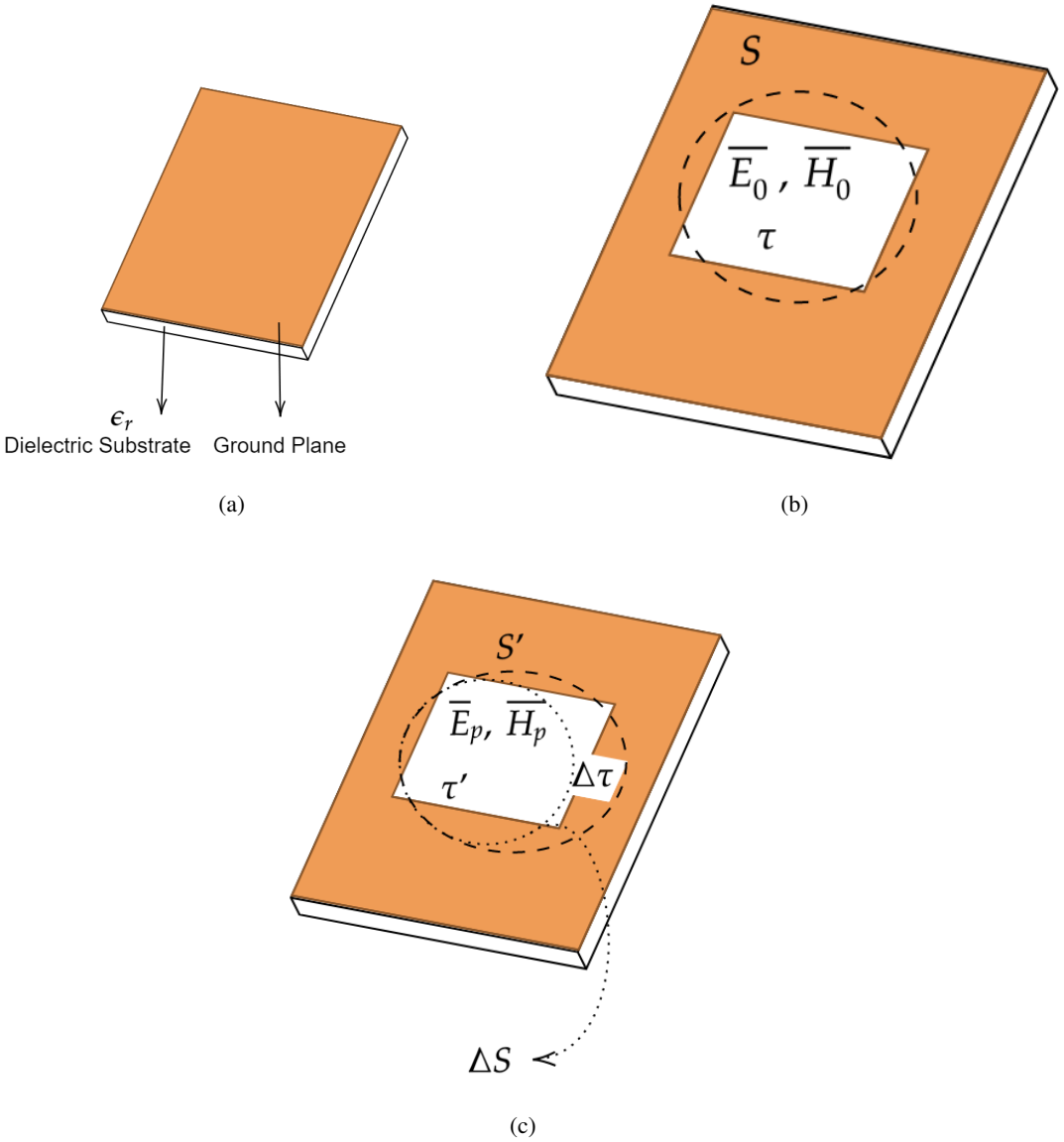

Figure 3.6: The geometry of a (a) dielectric slab waveguide without slot (b) dielectric slab waveguide with slot (a resonant cavity) (c) dielectric slab waveguide with slot and deformation (a perpetuated resonant cavity).

$$\frac{\omega_p - \omega_0}{\omega_0} \cong \frac{\iiint_{\Delta\tau}(\mu|\overline{H_0}|^2 - \epsilon|\overline{E_0}|^2)\, d\tau}{\iiint_{\tau}(\mu|\overline{H_0}|^2 + \epsilon|\overline{E_0}|^2)\, d\tau} \tag{3.7}$$

It is assumed that the denominator of (3.7) indicates the total energy stored due to the presence of the magnetic and electric fields, and the numerator represents the removed electric and magnetic energy by the perturbation. Therefore, if $\Delta\tau$ is small, equation of (3.7) can be expressed in term of the stored and removed energies as follows [68]

$$\frac{\omega_p - \omega_0}{\omega_0} \cong \frac{\Delta W_m - \Delta W_e}{\Delta W_m + \Delta W_e} \tag{3.8}$$

It is apparent from the equations of (3.7)-(3.8), the resonance frequency of such cavity and correspondingly Q-factor may either decrease and increase depending on the position of the cavity perturbation and the geometry of the cavity [68].

In the scope of this work, it is accepted that a fractal shape-slot (the region τ' shown in Figure 3.6.(c)) is small compared to the unperturbed cavity (refer to Figure 3.6.(b) and refer to Figure 3.8 (a)-(d)) and hence, it can create a self-similar perturbation on the cavity walls, therefore a fractal shape-slot alters the stored magnetic and electric energies in the cavity. Therefore, the fractal-slot is introduced on the ground plane of the dielectric slab fed by a microstrip line to obtain bi-directional radiation pattern and to control the resonance frequency and also Q-factor of the antenna as targeting to increase the input impedance BW of the antenna without increasing the antenna size.

In this work, a slot antenna, which is a dielectric slab with a slot on the ground plane and excited by a feed line as shown in Figure 3.8.(a), is selected. Although there are many methods of feeding a microstrip antenna such as open-ended microstrip line, coaxial probe, and proximity coupling [64], [61], in the design of the proposed antenna, open-ended microstrip is selected as a feed line to eliminate the solder on the copper patch which may disrupt the radiation characteristics of the patch antenna. As it is depicted in Figure 3.8.(a), the open-ended microstrip line is attached to the opposite side of the ground plane in which the slot is etched out from the ground plane.

3.3.2 Construction of the Fractal Shape

A various kind of structure based on classical fractals such as Hilbert Curve, Sierpinski Carpet, Koch Curve or irregular shapes also called randomness in fractal such as Random Koch Island, Modified Sierpinski Gasket can be constructed by employing some important proper-

Table 3.1: Self-similarity dimension of the proposed fractal geometry in this work

Fractal Shape	(s) or (IF)	(a) or (IO)	Self Similar Dimension, D
Based on Minkowski fractal	1/3	2	0.631

ties of the fractal shapes as includes [69]:

1. The self-similarity of a fractal shape can be characterized by two factors;

i. The iteration factor (IF) or the scale factor (s) indicates the how much the original (base, zeroth iteration) is scaled in two dimensions.

ii. The iteration order (IO) or the number of self-similar copies (a) describes how many repetition is performed to constitute a fractal shape.

2. The fractional dimension of the fractal geometries, there are several notations such as self-similarity dimension, compass dimension (also called divider dimension), box-counting dimension, Hausdorff's Dimension. More generally, for a self-similar fractal geometry, *the self-similar* dimension can be expressed in terms of the number of self-similar copies and the scale factor as given [62]

$$D = \frac{\log a}{\log(\frac{1}{s})} \tag{3.9}$$

Table 3.1 summarizes the scale factor (s), the number of self-similar copies (a), and Hausdorff's Dimension which are selected for the realization of the proposed fractal geometry in this work.

3.Iterated Function Systems (IFS) can be denoted as a language of fractals [69]. Iterated function systems (IFS) delineate a thoroughly versatile method which is conveniently exploited to generate a wide variety of fractal geometries. The Iterated Function System is defined by a series of Affine Transformation, w, which is expressed in a matrix form given as [69]

$$w\begin{pmatrix} x \\ y \end{pmatrix} = \begin{pmatrix} a & b \\ c & d \end{pmatrix}\begin{pmatrix} x \\ y \end{pmatrix} + \begin{pmatrix} e \\ f \end{pmatrix} \tag{3.10}$$

or equivalent by

$$w(x, y) = (ax + by + e, cx + dy + f) \tag{3.11}$$

The affine transformation, w is controlled by six parameters of a, b, c, d, e, and f which are

real numbers. The parameters of a, b, c, and d control the rotation and scaling whereas, e and f determine the linear translation in two dimensions.

By considering $w_n, n = 1, 2, 3..., N$ be a set of affine transformations given in (3.10), and A_0 be the initial geometry (image). The customization of this set of affine transformations on the initial geometry produces a set of self-similar copies, $(w_n(A_0), n = 1, 2, 3, ..., N)$.

As a final step, the creation of a new geometry is realized by collecting all the scaled, and iterated images result in $w_1(A_0) \bigcup w_2(A_0) \bigcup w_3(A_0)... \bigcup w_N(A_0)$ set of intersection can be represented by

$$W(A) = \bigcup_{i=1}^{i=n} w_n(A_n), \tag{3.12}$$

where W is called as the *Hutchinson Operator*, any of a fractal image can be carved out by recurrently applying W to the previous image.

For example, if the set A_0 indicates the initial geometry, then subset A can be given in the following way

$$A_1 = W(A_0), A_2 = W(A_1), A_3 = W(A_2)..., A_{k+1} = W(A_k) \tag{3.13}$$

An IFS produces an array which converges a final image A_∞ which is denominated as the attractor of the IFS [69].

Figure 3.7 illustrates the Iteration Function System modality for the generating of the proposed fractal shape. In this case, A_0 indicates the initial geometry which is a unit length. As a first step, the five linear transformations are attached to form the first iteration (1^{st}) of the proposed fractal shape, which is similar to the Minkowski fractal. As a next step, the second iteration (2^{nd}) of the proposed fractal shape is attained through six different affine transformations which are applied to A_1. It is important to notice that since the applied affine transformations are different from each other for both A_1 and A_2, the proposed fractal shape can be defined as "Randomness" in fractal geometry [62].

3.3.3 Antenna Configuration with the Proposed Fractal Shape

Figure 3.8 depicts the geometry of the proposed fractal-slotted antenna. An open-ended 50 Ω micro-strip transmission line having dimensions of $L_{feed} \times W_{feed}$ in xy-plane is selected to excite the proposed antenna and attached to the opposite side of the substrate. Besides, the location of the feed line is symmetrically arranged with respect to (x-axis) the centerline of the

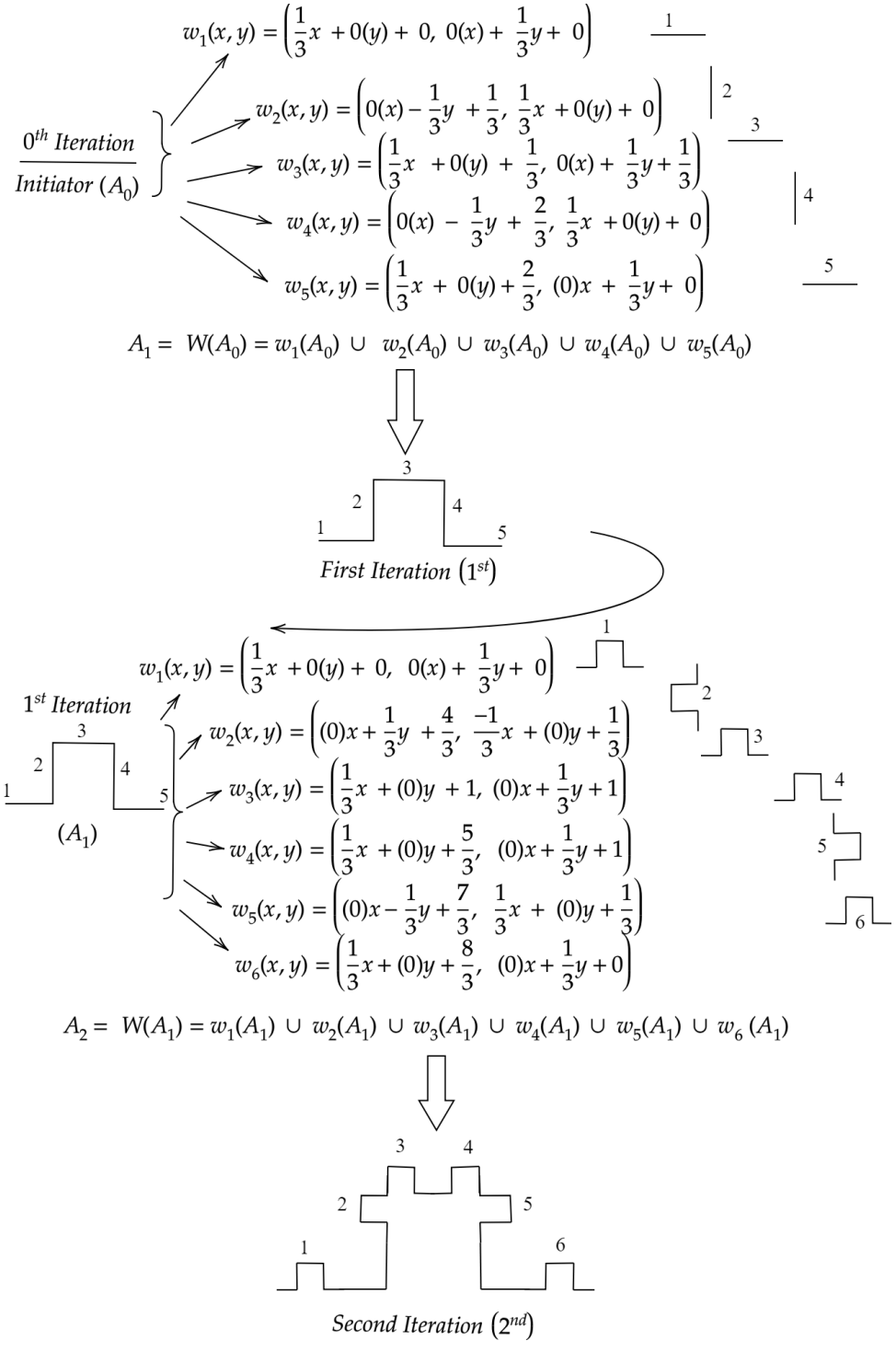

Figure 3.7: The iterated function system (IFS) for the proposed fractal geometry.

fractal shaped slot for each iteration. Since the length of the feed line profoundly affects the excitation of the slots correspondingly both the current distribution and resonant frequency, the length of feed line initially is selected as L_{feed}= (L_G + L_{SMA}) / 2.

The dimensions of the ground plane are approximately selected related to both the dimensions of the zeroth iteration having length and width of $L_{0th} \times W_{0th}$ in xy-plane and the Iteration factor (IO). Initially, the length and width of the of the ground plane are decided as L_G= 1/ (IO)× L_{0th}= 3×L_{0th} and W_G= 1/ (IO) × W_{0th}= 3×W_{0th}, respectively as shown in Figure 3.8.(a). Furthermore, instead of extending the length of ground plane in the direction of +x-axis to the end of the substrate to meet with the feeding line, suitable dimensions of L_{SMA} × W_{SMA} are selected and optimized in order to mount the SubMiniature version A (SMA) connector easily (Refer to Figure 3.8.(a)).

As it is mentioned in the previous section, when the ground plane is excited with the electric field along the x-axis, the surface waves propagate along the ground plane without any disturbance. However, it is expected that after the slots are etched out from the ground plane, the surface current distribution mainly concentrates on the boundary of the slots, and hence the dimensions of the slot ($L_{0th} \times W_{0th}$, zeroth iteration) profoundly determine the surface current distribution (field configuration) and correspondingly the resonant frequency. In order to determine the resonance frequency after the slots are removed (zeroth iteration), it is assumed that the field configurations (modes) along the slots shown in Figure 3.8.(a) are similar to the field configurations along the sides (perimeter) of the rectangular patch antenna. Therefore, to approximate the dimensions of L_{0th} and W_{0th} and to attain the dominant mode with the lowest resonance frequency, the equation given by [61] for the evaluation of the resonant frequencies of the cavity is used. For the plane configuration shown in Figure 3.8.(a) the formula can be rewritten as

$$(f_r)_{mnp} = \frac{1}{2\pi\sqrt{\mu\epsilon}}\sqrt{(\frac{m\pi}{L})^2 + (\frac{n\pi}{W})^2 + (\frac{p\pi}{h})^2} \tag{3.14}$$

As given in [61], if L>W>h, the dominant mode is the TM^z_{100} for the plane configuration as shown in Figure 3.8.(a). In this case, the half-cycle field variation (the half wavelength variation) is observed along the slot of L_{0th}, and since the half-cycle field variation creates the current density with the same magnitude but having opposite direction, the slots along the L_{0th} are accepted as non-radiating slots. On the contrary to this, since there is no field variation along the slots of W_{0th}, the current densities along the W_{0th} have the same magnitude and the same phase resulting in the far-field radiation. Under this condition, the resonant frequency is

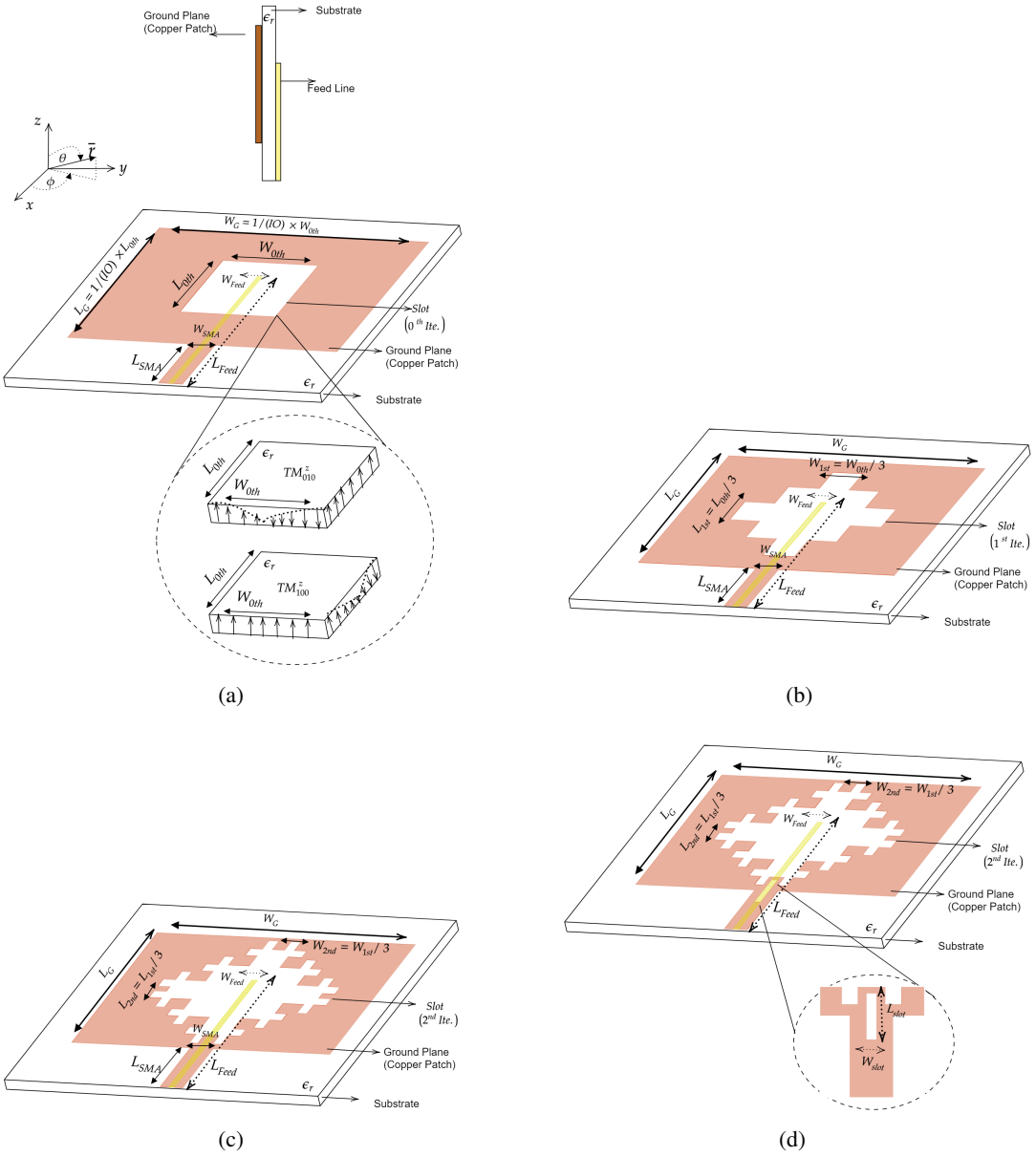

Figure 3.8: (a) The side and top view of the zeroth iteration (b) The top view of the first iteration (c) The top view of the second iteration (d) The top view of the second iteration with ⊔-shaped slot.

evaluated as given

$$(f_r)_{010} = \frac{v_0}{2L\sqrt{\epsilon_r}} \tag{3.15}$$

On the other hand, if W>L>h, the dominant mode is the TM^z_{010} for the plane configuration as shown in Figure 3.8.(a). In this case, the half-cycle field variation (the half wavelength variation) is observed along the slot W_{0th}, and since the half-cycle field variation creates the current density with the same magnitude, but opposite direction, the slots along the W_{0th} are accepted as non-radiating slots. On the contrary to this, since there is no field variation along the slots of L_{0th}, the current densities along the L_{0th} have the same magnitude and the same phase corresponding to the far-field radiation. Under this condition, the resonant frequency is evaluated as given

$$(f_r)_{001} = \frac{v_0}{2W\sqrt{\epsilon_r}} \tag{3.16}$$

It can be seen from equations of (3.15)-(3.16), the half wavelength variation along the one dimension of the slots (along L_{0th} or W_{0th}) is required to obtain a resonant at the corresponding frequency, whereas the radiation is mainly due to the other dimension in which there is no field variation along the corresponding dimension.

In the determination of the radiating and the non-radiating slots (L_{0th} and W_{0th}) for the zeroth iteration, the feed line position is first considered. Since the location of the feed line is centered at along the W_{0th} as shown in Figure 3.8, the distributed fields along the W_{0th} and the feed line may create interference which may result in the degradation in the far-field radiation pattern. Therefore, in order to avoid any interference, and to obtain a broadside radiation pattern, it is aimed to form radiation from the slots along the L_{0th} as shown in Figure. 3.8 (a) and hence the case of W>L>h is considered. In this case, it is accepted that the mode of TM^z_{010} along the proposed slots (zeroth iteration) is excited and hence the current densities along the slots of L_{0th} (in both the principal H- and E- plane) mainly contribute the far-field radiation.

As it is shown in Figure 3.9, as the number of IO increases since the electrical length increases seen by the surface current, and hence it is expected that the first resonance frequency due to the zeroth iteration shifts towards to the lower frequency side of the frequency spectrum. Furthermore, the length of each slot after the corresponding iteration can be approximately adjusted as $\lambda_g/2$ at the frequencies of interest (1.8, 2.1, and 2.45 GHz) to obtain

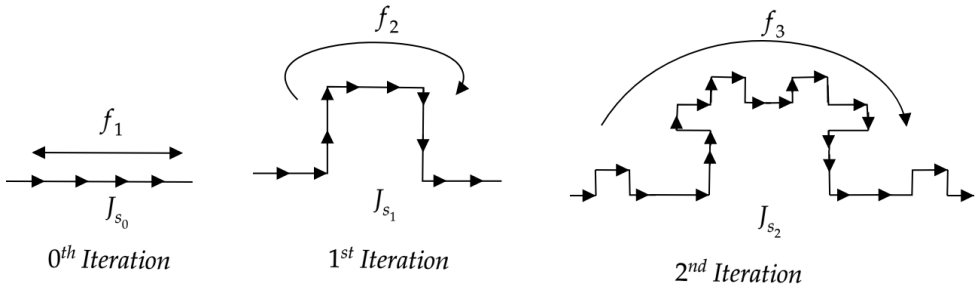

Figure 3.9: The implementation of the fractal geometry in the antenna.

distinct resonants by employing the fractal shape.

By considering both cases, first of all, the dimensions of the initial slot (zeroth iteration) are approximated by targeting to obtain a first resonant at the frequency band of 2.6-2.75 GHz. In order to attain the resonant frequency at around 2.6-2.75 GHz, the equation of (3.16) is used to determine both W_{0th} and L_{0th}, whose values are initially selected as 30 mm and 25 mm, respectively.

After the determination of dimensions of the initial slot (zeroth iteration), the first and the second iterations are employed to the antenna as shown in Figure 3.8.(b) and Figure 3.8.(c), respectively. As it is depicted in Figure 3.8.(d), the ⊔-shaped slot is etched out from the part of SMA connector to improve the return loss of the antenna over the desired frequency band from 1.8 to 2.5 GHz.

After many optimizations and trials, to acquire the best return loss, a reasonably stable radiation pattern and an agreeable gain from the proposed fractal-shaped slot antenna, all the parameters are optimized as given in Table 3.2. After the determination of the dimensions in the simulation, the proposed antenna is implemented on the Roger4003c substrate, Figure 3.10 indicates the fabricated prototypes of the proposed antenna for each iteration.

It should be noticed that as the iteration order increases both the structure of the proposed fractal shape and the realizable dimensions of the higher iterations become quite complicated, and further the fabrication of the antenna with the milling machine becomes more challenging therefore the iteration order is kept in the second order with the dimensions given in Table 3.1.

In the next sections, both the effect of the fractal-shaped slot and ⊔-shaped slot on the performance of the antenna regarding bandwidth, return loss and radiation pattern will be discussed.

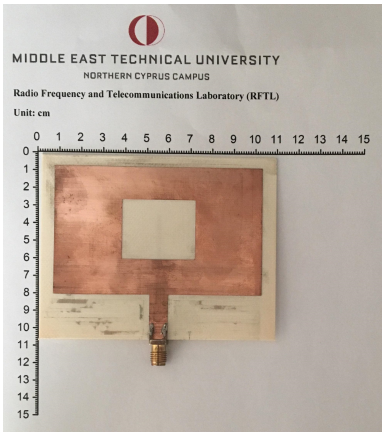

(a)

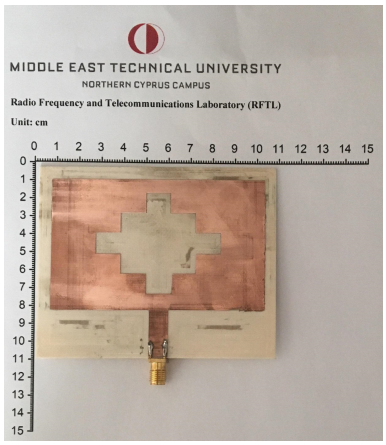

(b)

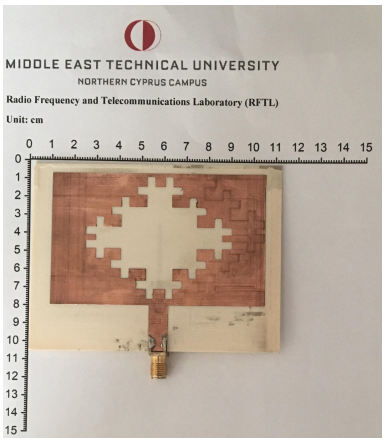

(c)

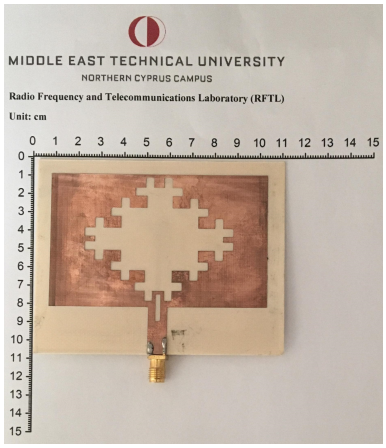

(d)

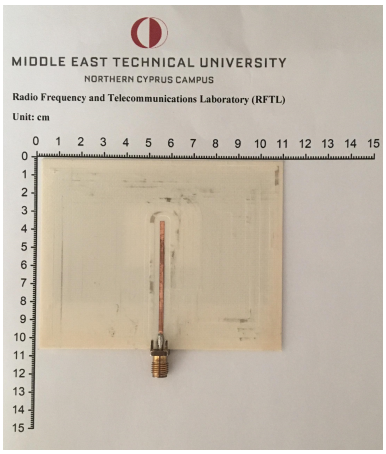

(e)

Figure 3.10: The fabricated prototypes of the antenna with the proposed fractal-shaped, top view of the (a) Zeroth iteration (b) First iteration (c) Second iteration (d) Second iteration with ⊔-shaped slot (e) back side view of the antenna.

Table 3.2: Optimized parameter values for the proposed fractal slotted antenna.

Parameter	Value (mm)
W_G	76.99
L_G	47.45
W_{feed}	1.65
L_{feed}	46.36
W_{0th}	27.25
L_{0th}	22.20
W_{slot}	1.65
L_{slot}	9.53
W_{SMA}	1.65
L_{SMA}	16.77

3.4 Performance Evaluation of the Proposed Fractal Antenna

3.4.1 Return Loss Evaluation

After the proposed fractal shape has been embodied into the antenna, both the simulated and the measured reflection coefficient (S_{11}) for the different iteration orders are given in Figure 3.11.(a) and Figure3.11.(b), respectively. In addition to this, the Smith Chart plots are provided as shown in Figure 3.11.(c) and Figure 3.11.(d) to observe the effect of iteration orders on the input impedance of the proposed antenna.

For the zero (0^{th}) iteration, it can be observed from Figure 3.11.(a) and Figure 3.11.(b), the lateral length of W_{0th} determines the initial resonance frequency. W_{0th} has the dimension of 27 mm, which is approximately required length for the half wavelength variation ($\lambda_g/2$) for the surface current to generate a resonant at between the frequencies of 2.6-2.8 GHz. The first resonant frequency after the zeroth iteration is achieved and recorded as $f_{r1,0^{th}(simu.)}$=2.75 GHz and $f_{r1,0^{th}(meas.)}$= 2.85 GHz from the simulation and the measurement results, respectively.

After the first iteration (1^{st}), as the IO increases, the first resonance ($f_{r1,0^{th}}$) frequency slightly shifts towards the lower side of the frequency spectrum. And then, after the first iteration, the new resonance frequencies can be observed. The first resonance frequency is recorded as $f_{r1,1^{st}(meas.)}$= 2.32 GHz, $f_{r1,1^{st}(simu.)}$= 2.28 GHz from the measurement and the simulation results, respectively. At the same time, the second resonant occurs at the frequency of $f_{r2,1^{st}(meas.)}$= 3.83 GHz which can be observed from the measurement result whereas the second resonant is barely observed from the simulation result. Nevertheless, the simulated S_{11} for the second resonance frequency is less than -7 dBm at the frequency of $f_{r2,1^{st}(simu.)}$=

3.77 GHz, which is very close to the measurement result. Furthermore, according to the measurement results, after the first iteration, the difference between the first ($f_{r1,1^{st}(meas.)}$) and the second ($f_{r2,1^{st}(meas.)}$) resonance frequency is less than one octave.

It is worth to notice that as the IO increases form the zero (0^{th}) iteration to the first iteration (1^{st}), the first measured resonance frequency after the zeroth iteration decreases by 17.1%. At the same time, the lateral length (W_{0th}) of the fractal shape increases by 35.6% as the IO order increases from the zero (0^{th}) iteration to the first iteration (1^{st}).

Besides, the ratio between the resonance frequencies can be defined as

$$r = \frac{f_{rn,IO}}{f_{rn+1,IO}} \quad n = 1, 2... \tag{3.17}$$

where $f_{rn,IO}$ is the first resonance and $f_{rn+1,IO}$ is the second resonance at the corresponding IO.

So, using (3.17), the ratio between the resonance frequencies of the first iteration can be expressed as $r = \frac{f_{r1,1^{st}(meas.)}}{f_{r2,1^{st}(meas.)}}$ and it is found as r= 0.605.

After the second iteration (2^{nd}), as the IO increases, both the first and second resonance frequencies, established in the first iteration, relocate to the lower side of the frequency spectrum as shown in Figure 3.11. There is an interesting observation of the frequency displacement after the second iteration, as seen in Figure 3.11, the second resonance frequency in the 1^{st} iteration rapidly shifts towards the lower side of the frequency spectrum, so the second resonance for the 2^{nd} iteration is established in the frequency band of interest (shown in Figure 3.11, green encircled rectangle). The first resonance frequency in the 2^{nd} iteration is recorded as $f_{r1,2^{nd}(meas.)}$= 1.93 GHz, $f_{r1,2^{nd}(simu.)}$= 1.82 GHz. And the second resonance in the 2^{nd} iteration is given as $f_{r2,2^{nd}(meas.)}$= 2.57 GHz, $f_{r2,2^{nd}(simu.)}$= 2.62 GHz.

Furthermore, as the IO increases form the first (1^{st}) iteration to the second iteration (2^{nd}), the first and second resonance frequencies, established in the 1^{st} iteration, drops by 16.8% and 32.9%, respectively. At the same time, the lateral length of the fractal shape (after the 2^{nd} iteration) increases by 50.6% when the similarity dimension of the fractal is 0.631. Similarly to the first iteration results, the difference between the $f_{r1,2^{nd}}$ and $f_{r2,2^{nd}}$ is less than one octave in both the simulation and the measurement results. Moreover, using (3.17) the ratio between the resonance frequencies of the second iteration can be expressed $r = \frac{f_{r1,2^{nd}(meas.)}}{f_{r2,2^{nd}(meas.)}}$ and it is given as r= 0.751.

As it can be seen from the simulated result of the second iteration without ⊔-shape slot, the return loss varies in the range of -15 to-20 dBm over the frequency band from 2 GHz

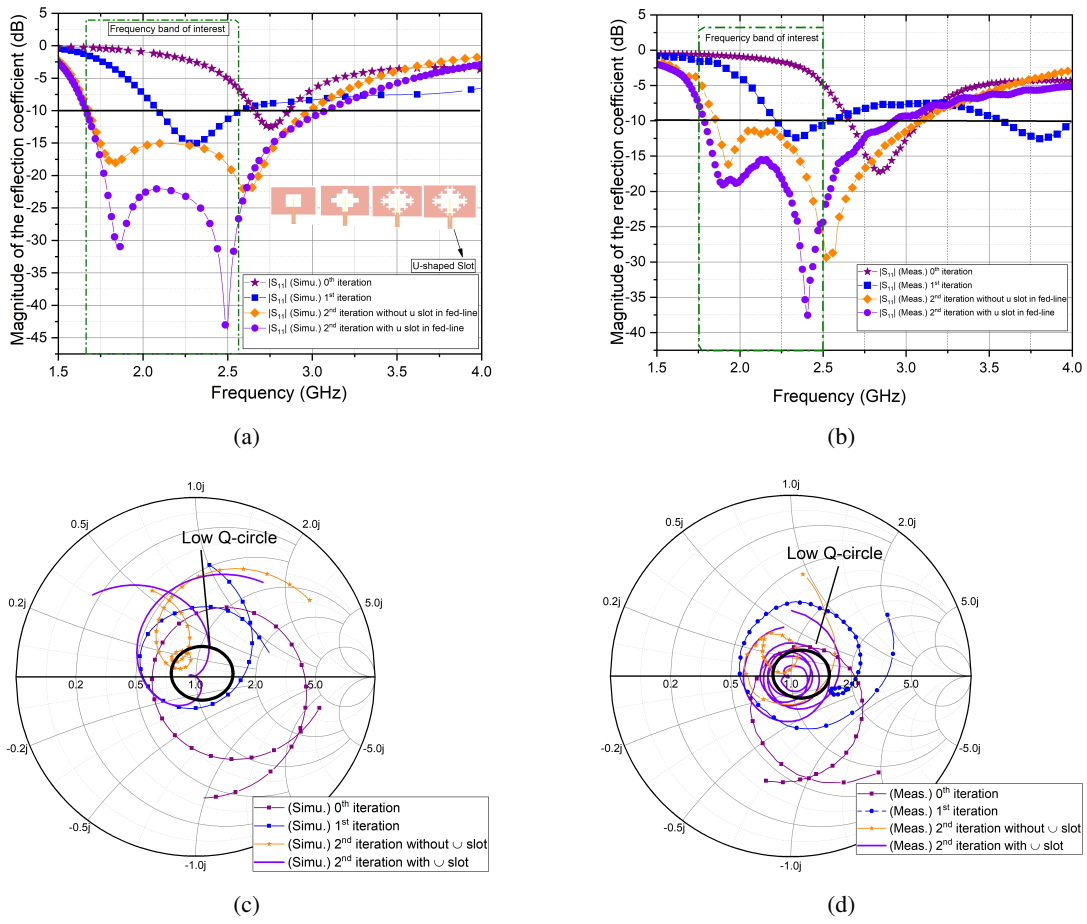

Figure 3.11: (a) The simulated results of 0^{th} & 1^{st} & 2^{nd} Iteration without ⊔-shaped slot in Fed-Line and & 2^{nd} Iteration with ⊔-shaped slot in Fed-Line (b) The measured results of 0^{th} & 1^{st} & 2^{nd} Iteration without ⊔-shaped slot in Fed-Line and & 2^{nd} Iteration with ⊔-shape slot in Fed-Line (c) Simulated input impedance of the antenna on Smith chart (d) Measured input impedance of the antenna on Smith chart.

to 2.4 GHz. As it is assumed that the return loss in the simulation may go up to the -10 dBm in the practical measurement, it is aimed to bring down the S_{11} below the - 20 dBm. Therefore, ⊔-shape slot has been etched out from the feed-line part of the ground plane (SMA part) as shown in Figure.3.8.(d) so as to improve the magnitude of reflection coefficient over the entire frequency band of 1.8 - 2.5 GHz. As it is observed from the input impedance of the antenna (refer to Figure 3.11 (c)), it posses inductive reactance at the frequency band of interest. Therefore, a narrow ⊔-shape slot is selected yielding capacitive reactance, so that it can alleviate the inductive reactance of the proposed antenna over the frequency band from 1.8 - 2.5 GHz. So then, it brings the input impedance of the antenna very close to the center of the SC over the desired frequency band. As it is observed from both simulation and measurement results, show in Figure 3.11 (a)-(d), a simple ⊔-shape slot enhances the capacitive coupling between the feed line and the fractal geometry resulting in improvement in S_{11}.

In the light of the reflection coefficient results, the resonance frequency lowering phenomenon of the fractal shape is acquired. Moreover, in the scope of this work, the resonance frequency ratios (r=0.605 from the 1^{st} iteration, r= 0.751 from the 2^{nd} iteration) are found as closely to the self similar dimension (D = 0.631) of the proposed fractal shape.

In addition to the resonance frequency lowering feature of the fractal shape, in order to investigate the effect of the fractal shaped-slot on the antenna bandwidth, both the Impedance Bandwidth (IBW) and the Fractional Bandwidth (FBW) of the antenna are calculated for different iteration orders by using well-known formula as given

$$f_c = \frac{f_1 + f_2}{2} \tag{3.18}$$

$$IBW = f_2 - f_1 \tag{3.19}$$

$$FBW = \frac{IBW}{f_c} * 100 \tag{3.20}$$

where f_1 and f_2 represent the frequencies which are taken for a target S_{11} = -10 dB, and also f_c is the center frequency. The corresponding simulated and the measured results for the both IBW and FBW are listed in Table 3.3.

As it is observed from the Table 3.3, both the simulated and measured results show that as the IO increases, both IBW and FBW of the antenna enhance. The measured results demonstrate that the antenna with 2^{nd} iteration without ⊔-shaped slot has IBW as large as 1205 MHz

Table 3.3: Summarized results for both the impedance bandwidth (IBW) and fractional bandwidth (FBW) of the antenna

Antenna with IO	$f_1(MHz)$				$f_2(MHz)$				IBW (MHz)				$FBW(\%)$			
	Simu.		*Meas.*		*Simu.*		*Meas.*		*Simu.*		*Meas.*		*Simu.*		*Meas.*	
$0^{th}ite.$	2656		2660		2852		3085		196		419		7.11		14.4	
$1^{st}ite.$	2086 (Lower)	– (Upper)	2225 (Lower)	3580 (Upper)	2561 (Lower)	– (Upper)	2545 (Lower)	3995 (Upper)	475 (Lower)	– (Upper)	320 (Lower)	415 (Upper)	20.4 (Lower)	– (Upper)	13.4 (Lower)	11 (Upper)
$2^{nd}ite.witohut \sqcup -slot$	1681		1885		2981		3090		1300		1205		55.8		48.4	
$2^{nd}ite.with \sqcup -slot$	1666		1790		3061		2930		1395		1140		59.1		48.3	

or FBW of 48.4% whereas the antenna with 2^{nd} iteration with ⊔-shaped slot posses IBW of 1140 MHz and FBW of 48.3%. As it can be seen from the measured results, the effect of the ⊔-shaped slot on IBW is negligible since both the antenna before and after the ⊔-shaped slot feature same FBW. In addition to this, since the FBW is accepted as a criterion indicating whether antenna has a wide-band operation or not, the proposed antenna with the FBW of 48.3% can be categorized as a broadband antenna.

At that point, it is important to notice that as the physical dimensions of the antenna depend on the operating frequency and permittivity of the substrate and also the frequencies taken as targeting $S_{11} = -10$ dB differ from one design to another, the comparison of for the compactness of the antenna with respect to the bandwidth may not be fair. Therefore, in order to make equitable comparisons, the bandwidth dimension ratio (BDR) is defined in ultra-wideband/super-wideband (UWB/SWB) antenna design. BDR ratio indicates that "how much operating bandwidth (in percentage) can be provided per electrical area unit" and it can be evaluated as [59]

$$BDR = \frac{IBW}{\lambda_{width} \times \lambda_{length}} \tag{3.21}$$

where the λ_{withd} and λ_{length} are the wavelength of the lower-end operating frequency which is taken as a target $S_{11} = -10$ dB. And the unit of BDR is $\%/\ \lambda^2$.

Although the proposed antenna is not categorized as an ultrawideband antenna, it can be accepted as a wide-band antenna. In addition, since the self-similarity feature of the fractal shape is exploited to reduce the size of the antenna especially along the length, BDR ratio can be pointed out. The proposed antenna has the BDR ratio of 103.56 ($\%/\ \lambda^2$) when the electrical dimensions of the proposed antenna is $0.53\lambda_{width} \times 0.88\lambda_{length}$.

Furthermore, as it is noted in the previous section since the fractal shape on the ground plane profoundly alters the stored magnetic and electric energy inside the dielectric-loaded cavity, the Q-factor of the cavity is expected to change with the fractal shape perturbation. The gradual decrease in the Q-factor can be observed by looking at the measured Smith Chart

results (refer to Figure 3.11 (d). The measurement results have verified that as the IO increases, the resonance loops on the SC get tighter and approach to the low Q-circle on SC. As a result of this, fractal shape yields a gradual decrease in the Q-factor of the resonance resulting in an agreeable enhancement for the IBW (or FBW) of the antenna.

Ultimately it can be seen from the return loss results, the BW enhancement phenomenon of the proposed fractal shaped-slot has been verified with the measurements. Furthermore, the operating frequency of the proposed antenna is significantly improved, and the aim for covering all the frequency bands starting from 1800/1900 MHz, 2.1 GHz, 2.4 GHz, 2.45 GHz corresponding to standards like GSM, UMTS, ISM, WLAN, respectively is achieved. As the return loss of the antenna only describes the matching condition of the antenna with the feed line, the electromagnetic behavior of the antenna is also examined to acquire a better insight. Therefore, in the next section, the electromagnetic characteristics of the antenna such as gain, radiation pattern, and surface current distribution will be explored.

3.4.2 Gain, Surface Current Distribution and Radiation Pattern Evaluation

Both the radiation pattern and the gain measurement of the antenna are carried out at the frequencies of 1800 MHz, 2100 MHz, and 2450 MHz in the anechoic chamber. The setup for the gain measurement is shown in Figure 3.12. Rohde & Schwarz HF906 Double-Ridged Waveguide Horn Antenna is used as a Transmitter antenna (T_x), and the proposed fractal slotted microstrip antenna (Antenna Under Test, AUT) is used as a receiver (R_x), and it is aligned with the T_x.

The normalized radiation patterns of the zeroth, first, and second (without and with ⊔-shaped slot) are given in Figure 3.13 – 3.24. It is noteworthy, it is assumed that the grounded side of the antenna is accepted at the +x direction and the dielectric covered side is at -x-direction. Also, all radiation patterns in the both principal E- and H- plane for each iteration show slight asymmetry and ripples. This situation can be attributed to the small fabrication failure in the fractal shape, alignment mismatch with the transmitter antenna as well as the metallic part of the connecting cable causing reflection.

For the radiation pattern of the antenna with the 0^{th} and 1^{st} iteration, the dipole-like radiation characteristic is barely observed at the frequency of 1800 MHz whereas the formation of the radiation pattern is more dipole-like at the frequencies of 2100 MHz and 2450 MHz. As it is seen from the results, the radiation pattern of the antenna becomes more similar to the dipole-like radiation in E-plane whereas it becomes more likely to omni-directional ra-

diation in H-plane as the iteration order increases for all frequencies of interest. Moreover, bi-directional and broadside radiation patterns are fairly observed at each iteration order and at all frequencies. Furthermore, as it can be observed from the Figure 3.21- 23, the antenna with 2^{nd} order with ⊔-slot provides fairly stable bi-directional radiation pattern at the frequencies of interest.

The 3-dB beam-width of the antenna for each iteration is summarized and given in Table 3.4. The proposed antenna with 2^{nd} IO having ⊔-slot features half-power beam-width of 90^o, 84^o and 71^o in the simulation, whereas the measured half-power beam-width are recorded as 61.6^o, 77.7^o and 97.2^o at the frequencies of 1800, 2100, and 2450 MHz, respectively. Although the radiation patterns in y-z and x-z plane tilt, the field is still efficiently strong at the desired direction ($\mp x$) .

From the simulations, a considerable surface current is concentrated on the fractal boundary at the desired frequencies as it is expected. It indicates that the fractal boundary effectively provides the path for electric current at the frequencies of interest. The vertical component of the surface current mainly contribute to the co-polarization radiation as well as the cross-polarization radiation is due to the horizontal component of the surface current. It can be observed from Figure 3.22–24, both the co-polarization and cross-polarization levels in the radiation pattern of the proposed antenna are high. The reason is that the fractal boundary efficiently sets symmetrical paths for surface current in both vertical and horizontal direction, which results in comparable co-polarization and cross-polarization levels. Even though high-level cross-polarization is an undesirable radiated field, in most energy harvesting antenna, the cross-polarization may be required so that the antenna is able to receive either vertically or horizontally polarized RF signals. Therefore, high-level co-polarization and cross-polarization have shown that the proposed antenna is dual polarization [70].

In addition to radiation patterns, the gain of the proposed antenna was measured at the frequencies of interest. The simulated and measured realized gains of the proposed antenna are plotted in Figure 3.25. The proposed antenna yields realized gains of 2.44 dBi, 2.89 dBi, and 4.43 dBi in the measurements whereas it features gains of 4.19 dBi, 4.47 dBi, and 4.49 dBi in the simulations at the frequencies of 1800 MHz, 2100 MHz, and 2450 MHz, respectively. The gain results of 1800 MHz and 2100 MHz was unexpected. The reason of difference between simulation and measurement results might be the losses due to the feed line.

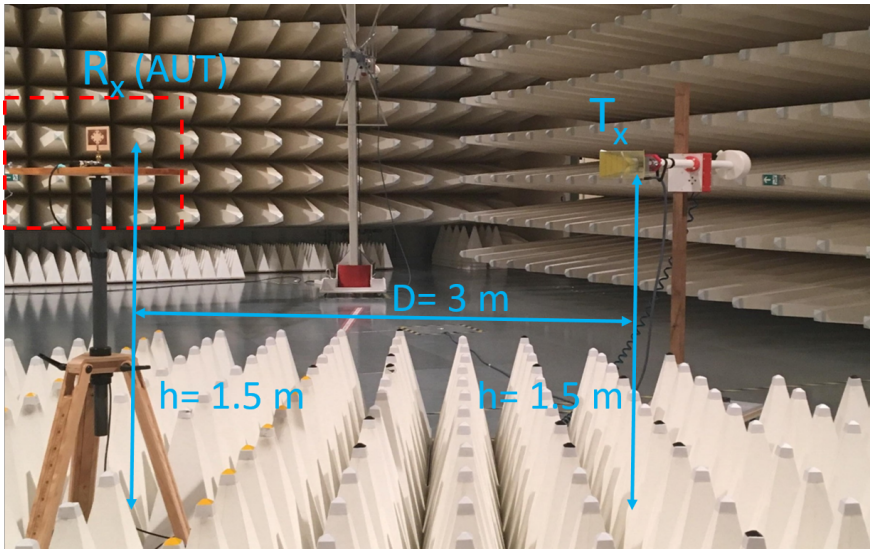

Figure 3.12: The anechoic chamber measurements of the proposed antenna.

Table 3.4: Summarized results for the half–power bandwidth (HPBW) of the antenna

Antenna with IO	**1800 MHz** (°)		**2100 MHz** (°)		**2450 MHz** (°)	
	Simu.	**Meas.**	**Simu.**	**Meas.**	**Simu.**	**Meas.**
$0^{th} ite.$	72	62	70	55.7	70	49.8
$1^{st} ite.$	86	56.5	81	54.9	74	92.9
$2^{nd} ite.$	90	57.5	84	109	72	85.8
$2^{nd} ite. with U-slot$	90	61.6	84	77.7	71	97.2

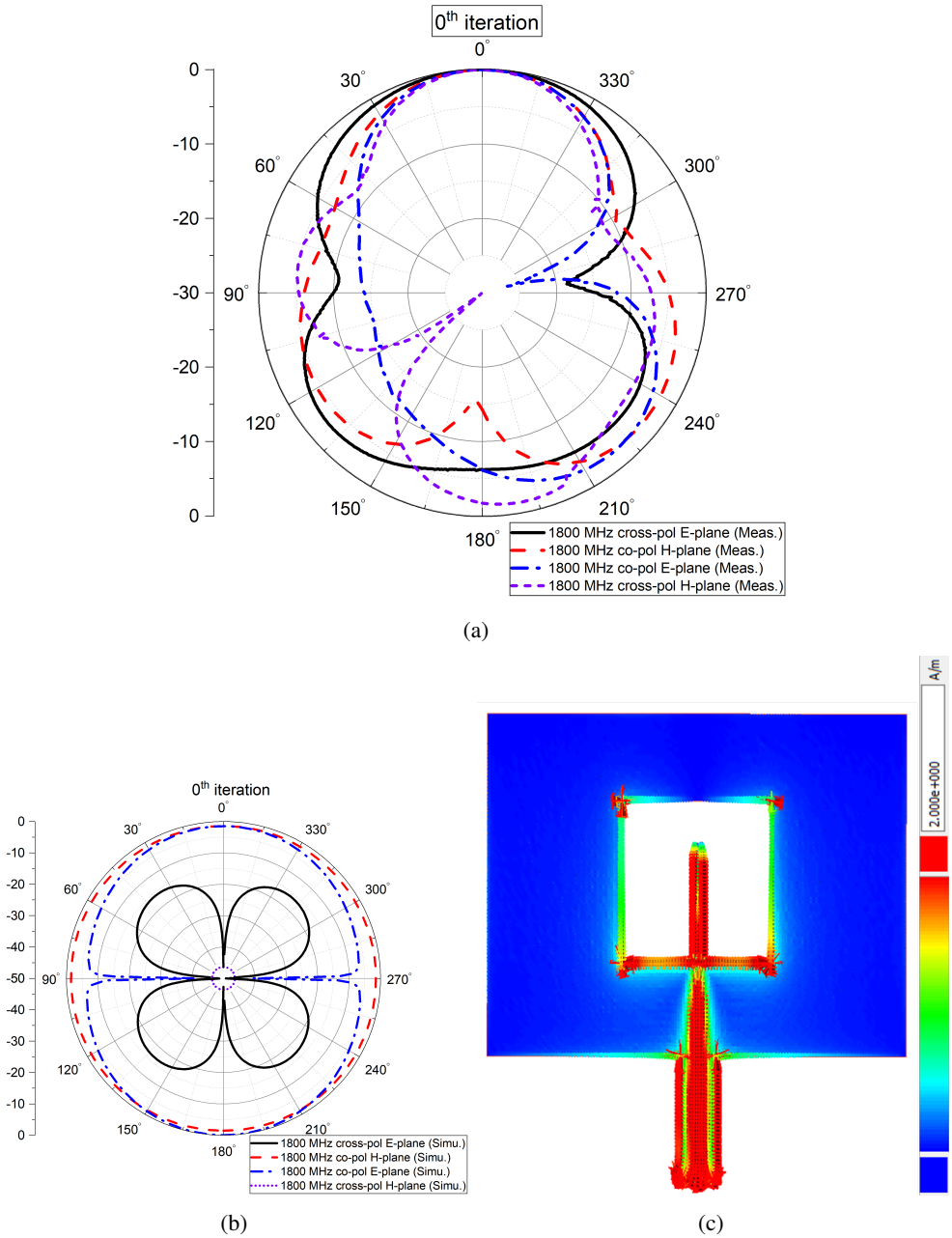

Figure 3.13: The radiation pattern of the zeroth iteration in the both x-z (H) plane and y-z (E) plane (a) measured results (b) simulated result (c) surface current distribution at 1800 MHz.

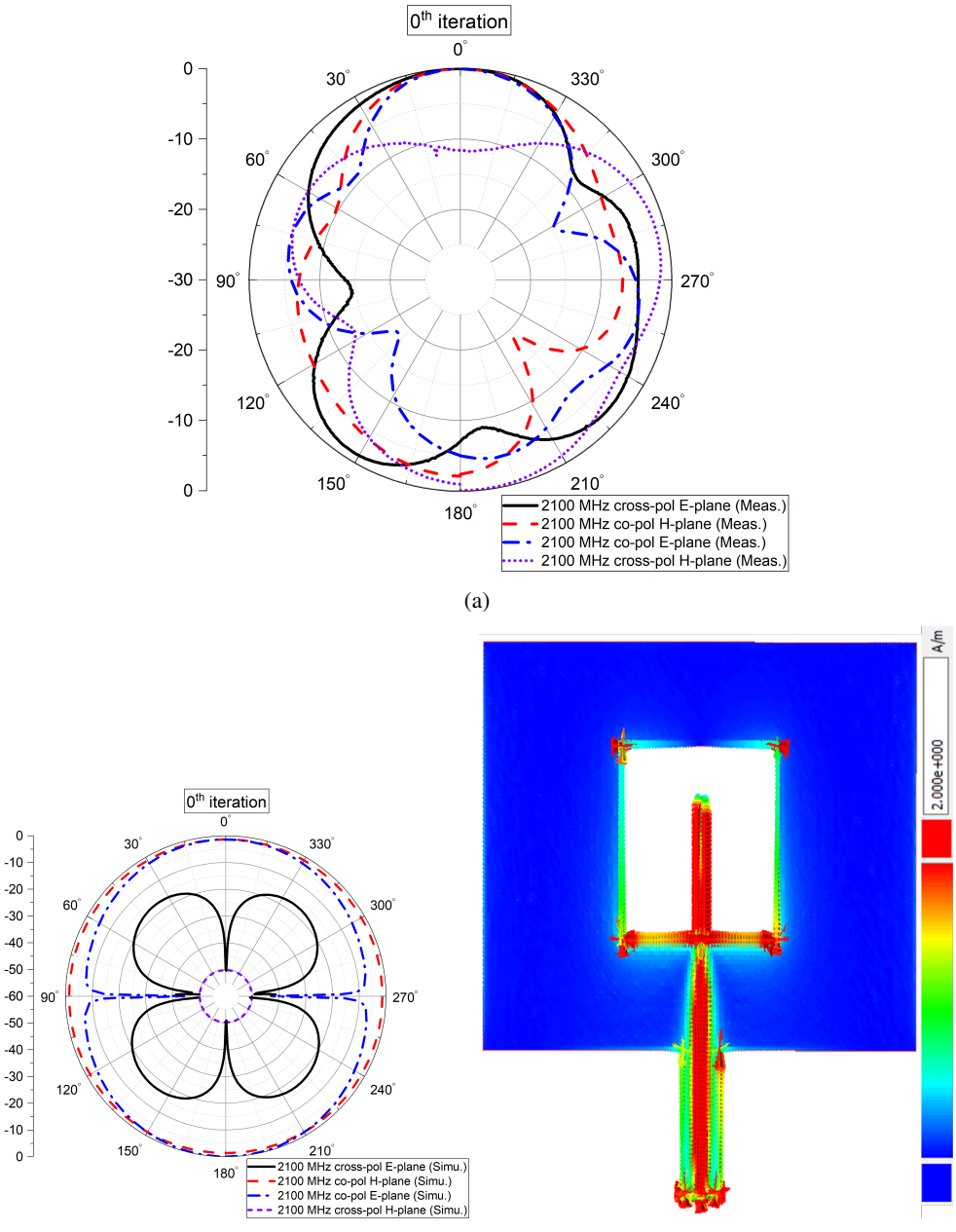

Figure 3.14: The radiation pattern of the zeroth iteration in the both x-z (H) plane and y-z (E) plane (a) measured results (b) simulated result (c) surface current distribution at 2100 MHz.

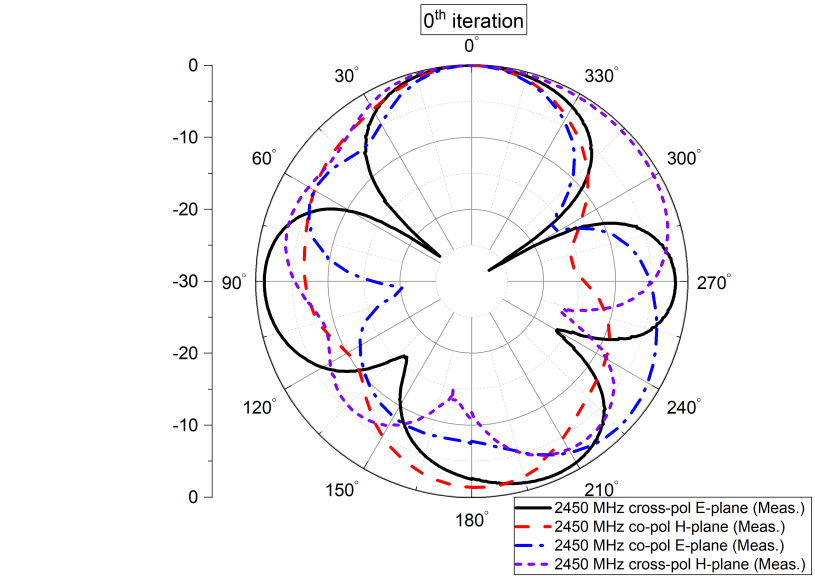

(a)

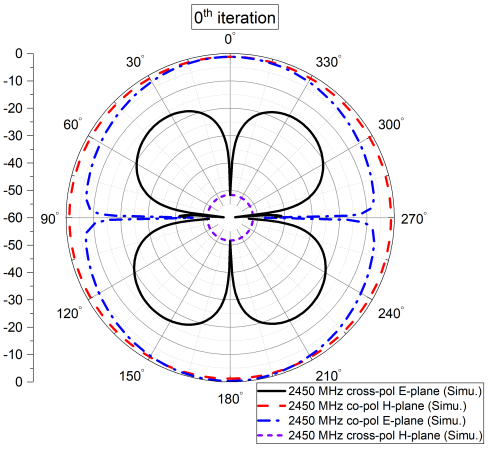

(b)

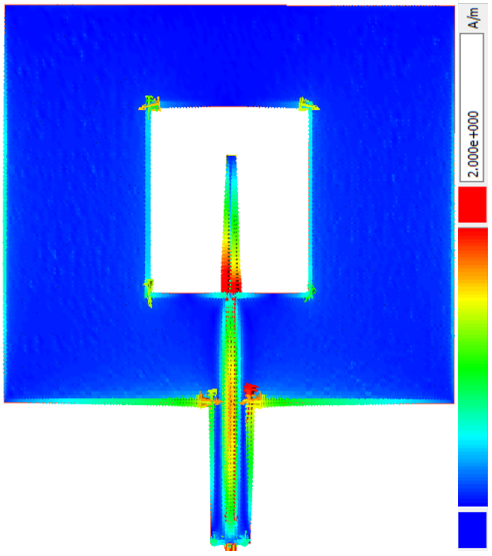

(c)

Figure 3.15: The radiation pattern of the zeroth iteration in the both x-z (H) plane and y-z (E) plane (a) measured results (b) simulated result (c) surface current distribution at 2450 MHz.

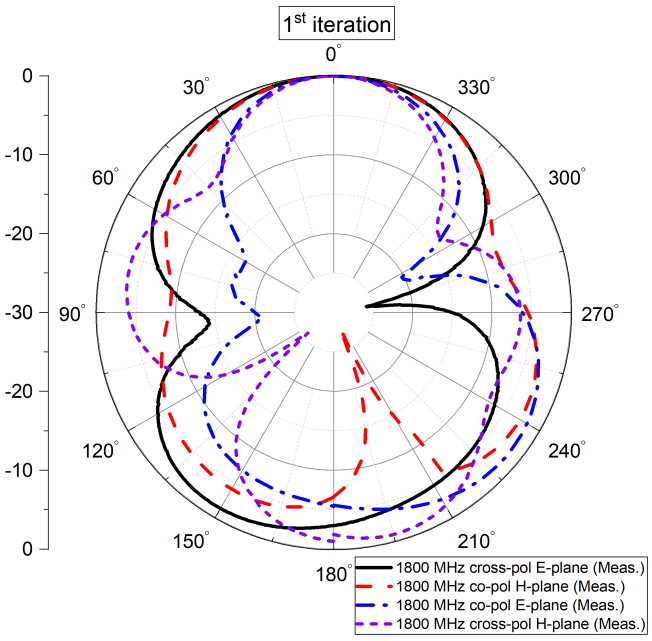

(a)

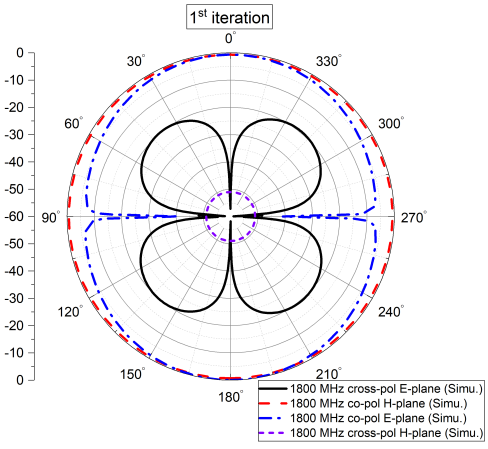

(b)

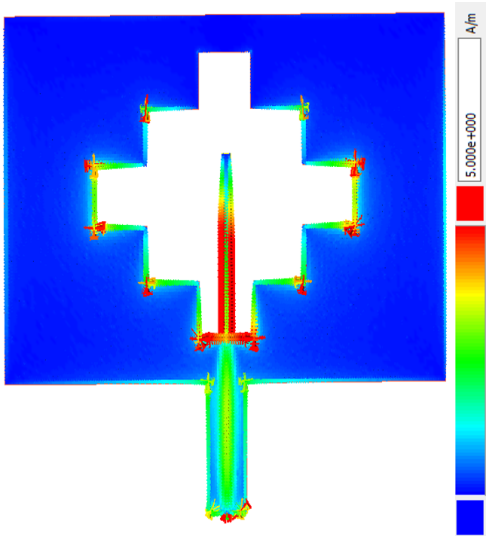

(c)

Figure 3.16: The radiation pattern of the first iteration in the both x-z (H) plane and y-z (E) plane (a) measured results (b) simulated result (c) surface current distribution at 1800 MHz.

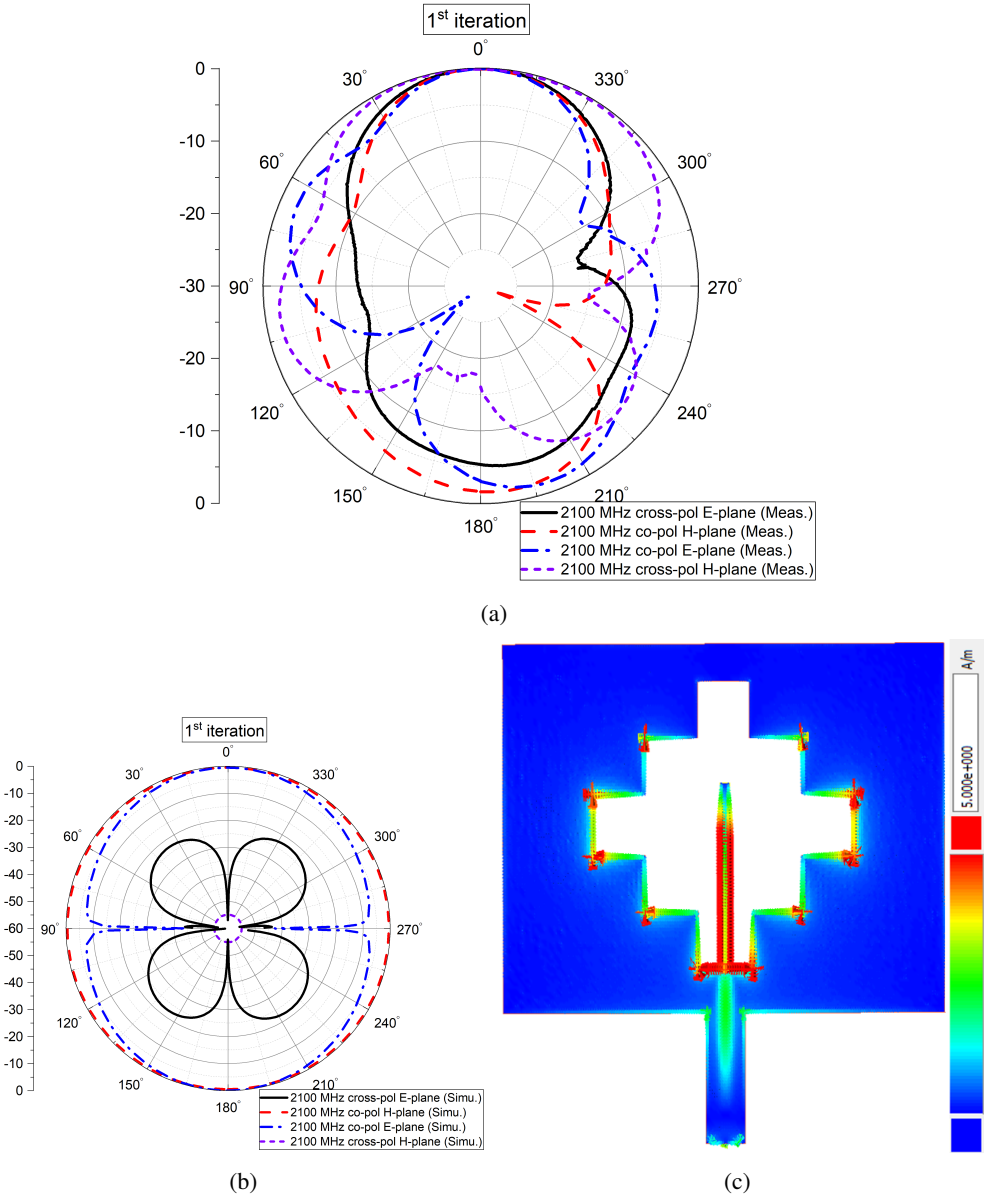

Figure 3.17: The radiation pattern of the first iteration in the both x-z (H) plane and y-z (E) plane (a) measured results (b) simulated result (c) surface current distribution at 2100 MHz.

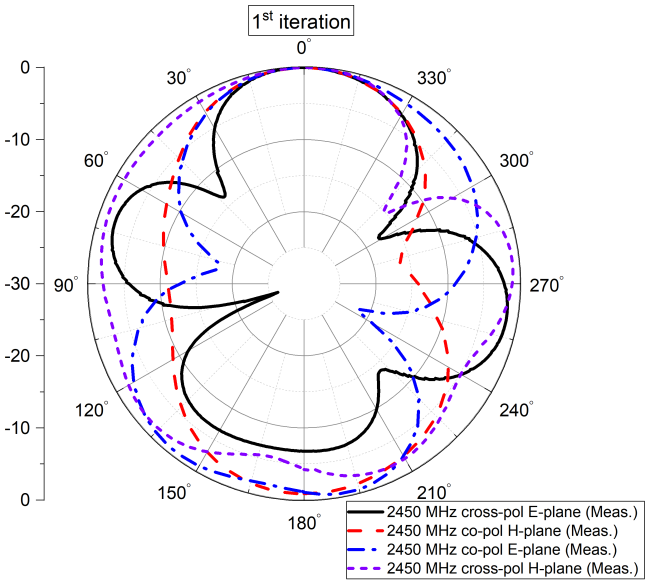

(a)

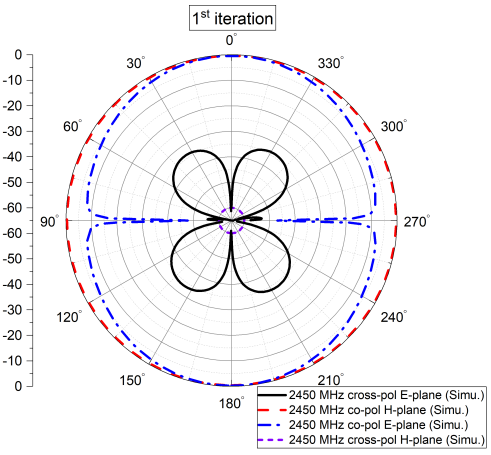

(b)

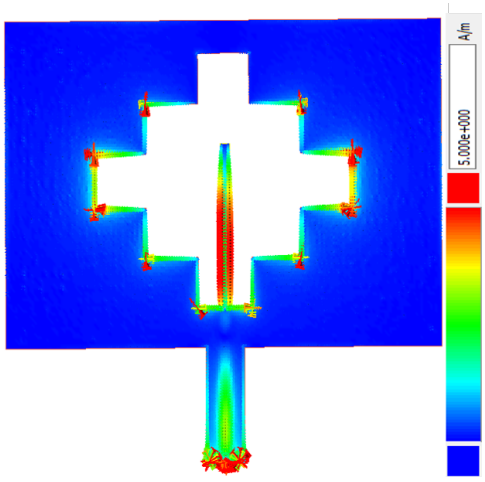

(c)

Figure 3.18: The radiation pattern of the first iteration in the both x-z (H) plane and y-z (E) plane (a) measured results (b) simulated result (c) surface current distribution at 2450 MHz.

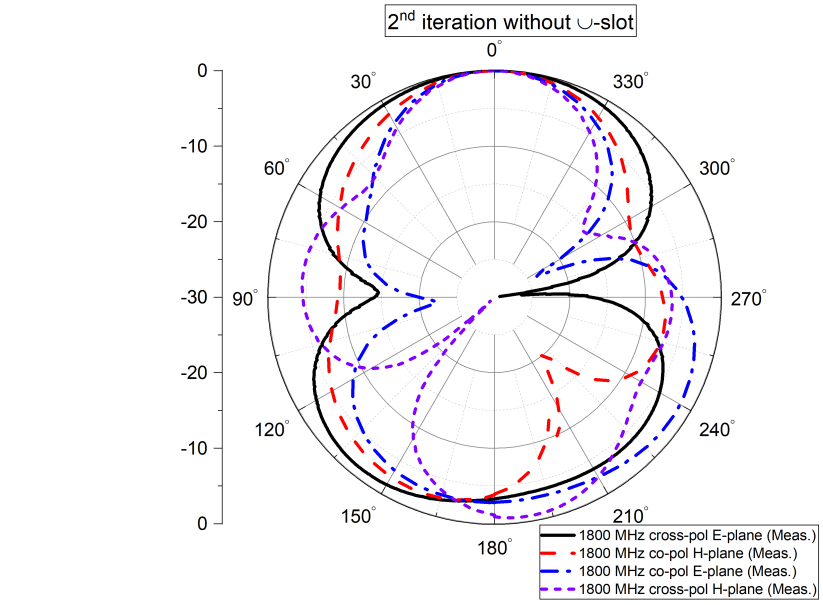

(a)

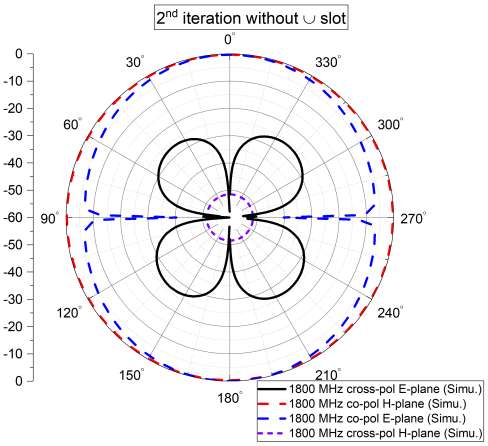

(b)

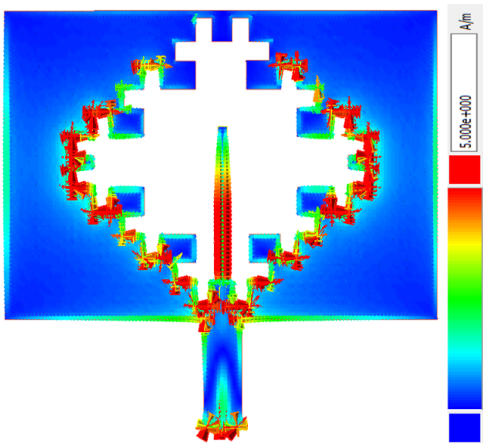

(c)

Figure 3.19: The radiation pattern of the second iteration without ⊔-shape slot in the both x-z (H) plane and y-z (E) plane (a) measured results (b) simulated result (c) surface current distribution at 1800 MHz.

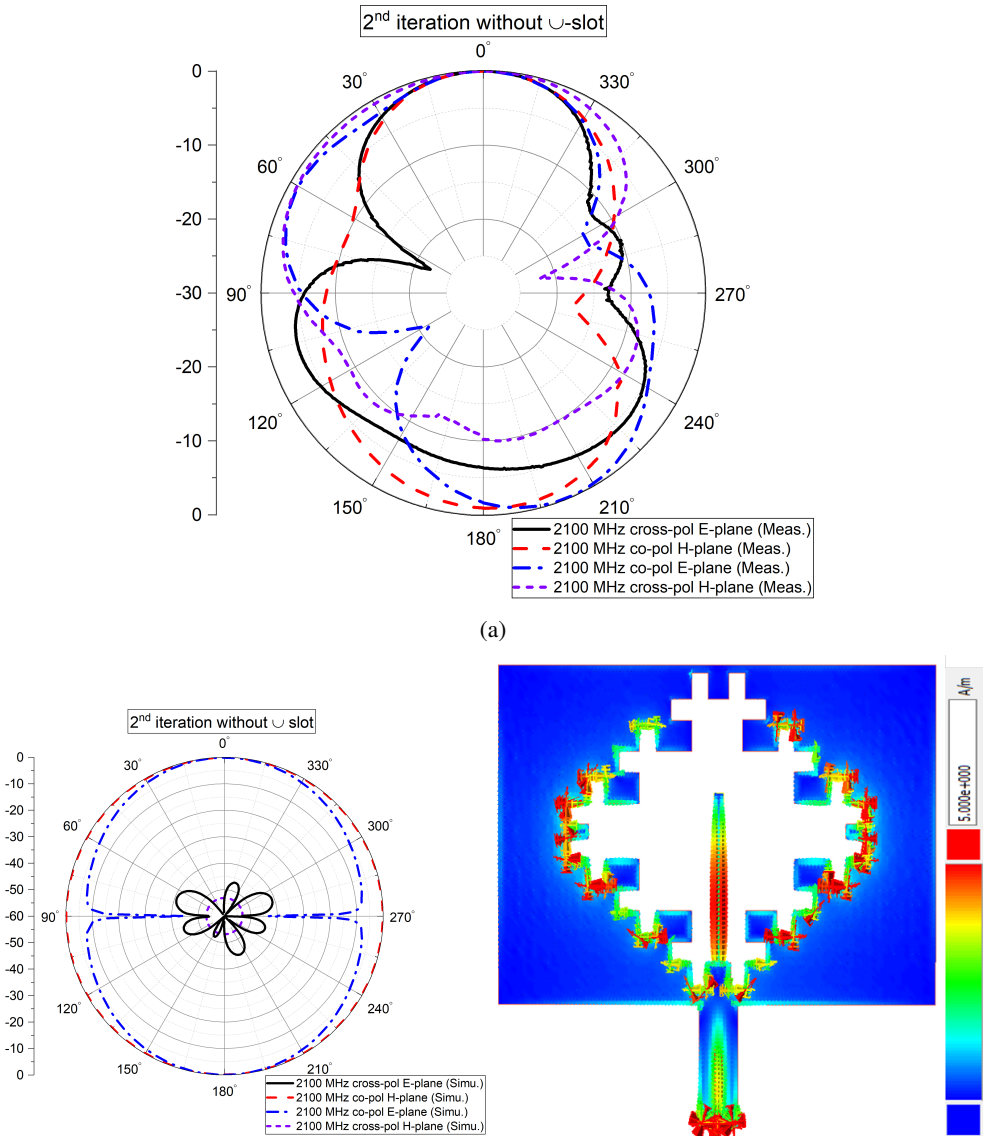

Figure 3.20: The radiation pattern of the second iteration without ⊔-shape slot in the both x-z (H) plane and y-z (E) plane (a) measured results (b) simulated result (c) surface current distribution at 2100 MHz.

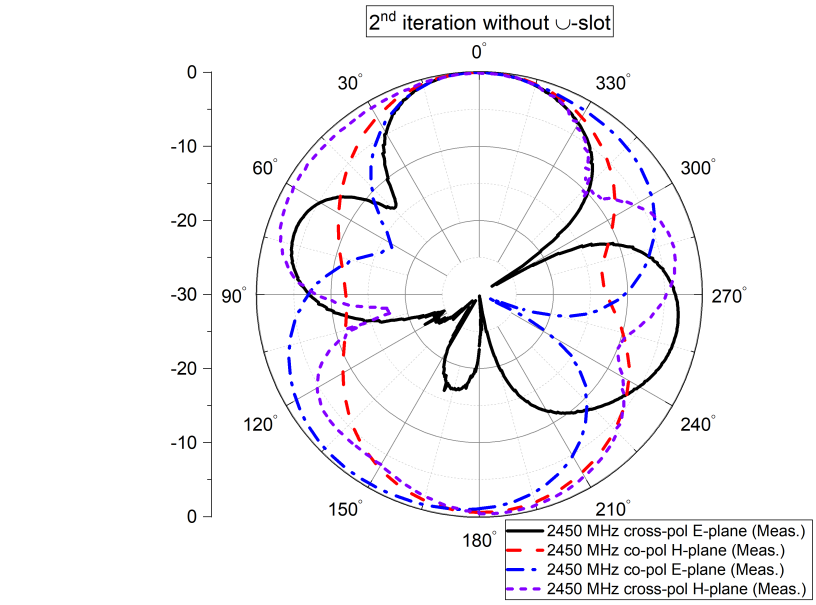

(a)

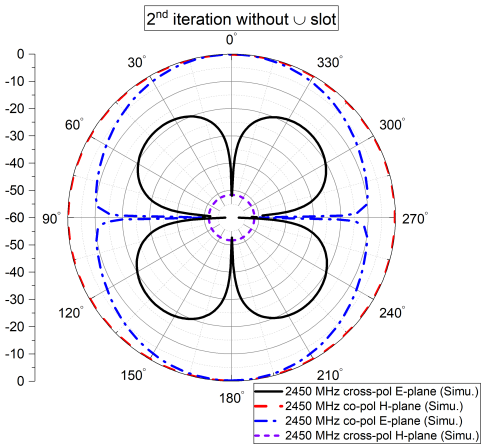

(b)

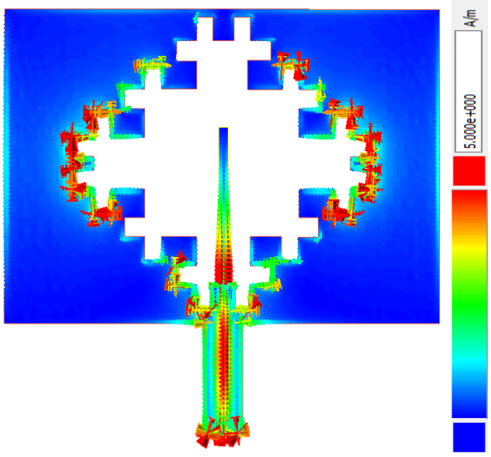

(c)

Figure 3.21: The radiation pattern of the second iteration without ⊔-shape slot in the both x-z (H) plane and y-z (E) plane (a) measured results (b) simulated result (c) surface current distribution at 2450 MHz.

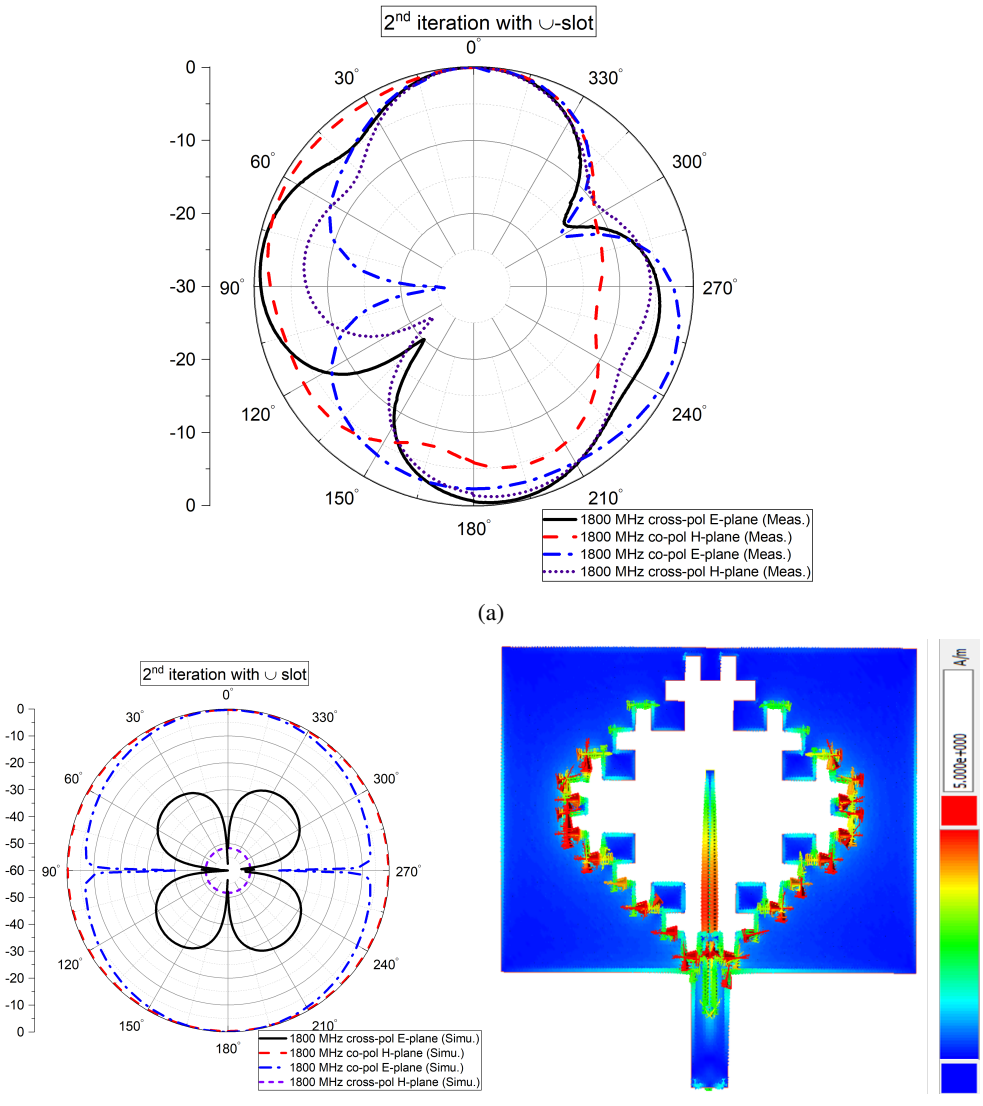

Figure 3.22: The radiation pattern of the second iteration with ⊔-shape slot in the both x-z (H) plane and y-z (E) plane (a) measured results (b) simulated result (c) surface current distribution at 1800 MHz.

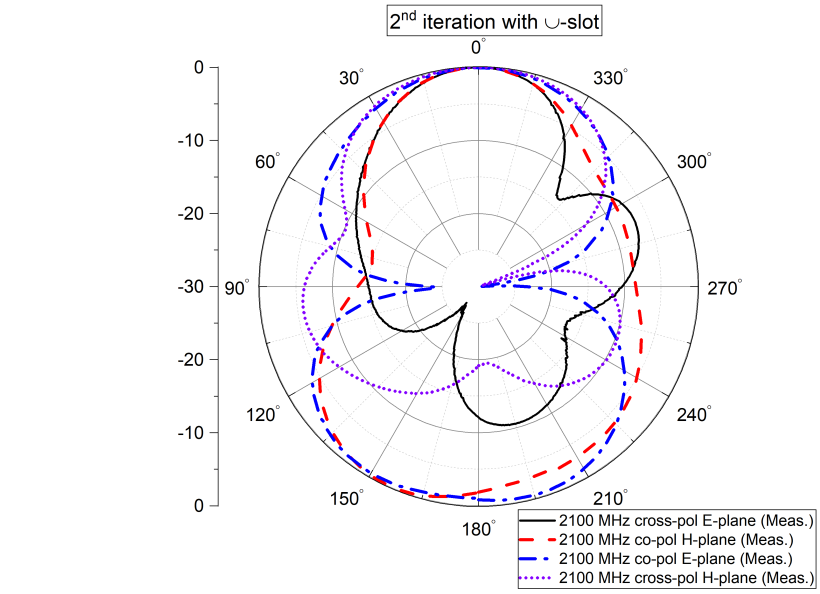

(a)

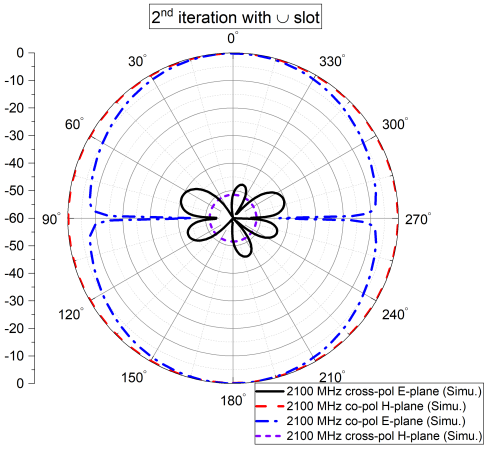

(b)

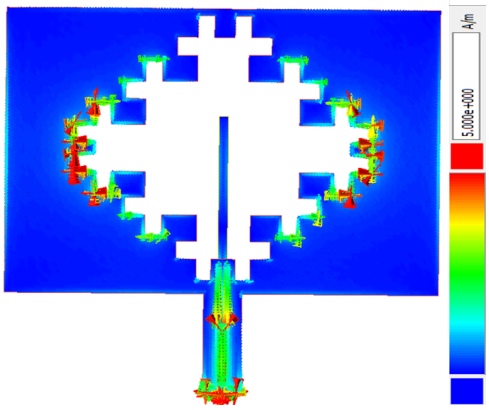

(c)

Figure 3.23: The radiation pattern of the second iteration with ⊔-shape slot in the both x-z (H) plane and y-z (E) plane (a) measured results (b) simulated result (c) surface current distribution at 2100 MHz.

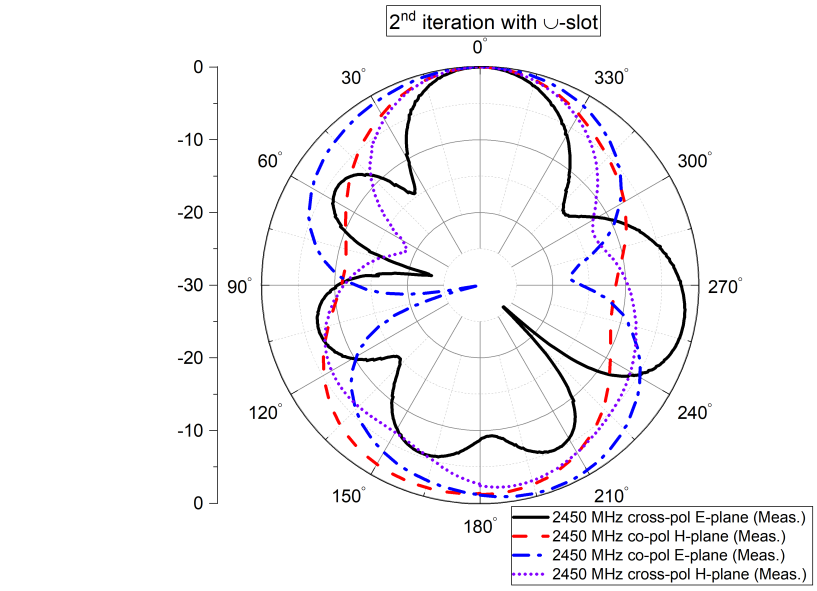

(a)

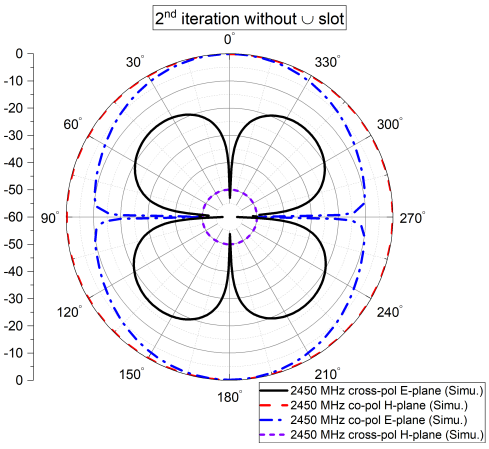

(b)

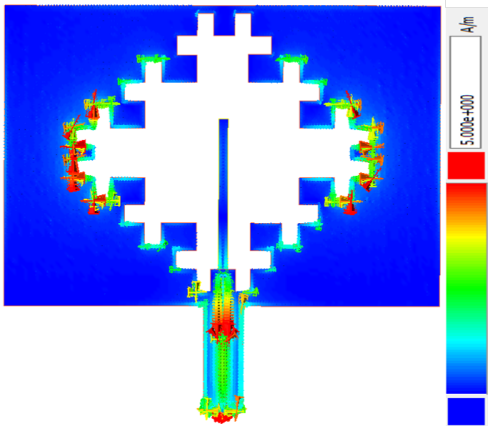

(c)

Figure 3.24: The radiation pattern of the second iteration with ⊔-shape slot in the both x-z (H) plane and y-z (E) plane (a) measured results (b) simulated result (c) surface current distribution at 2450 MHz.

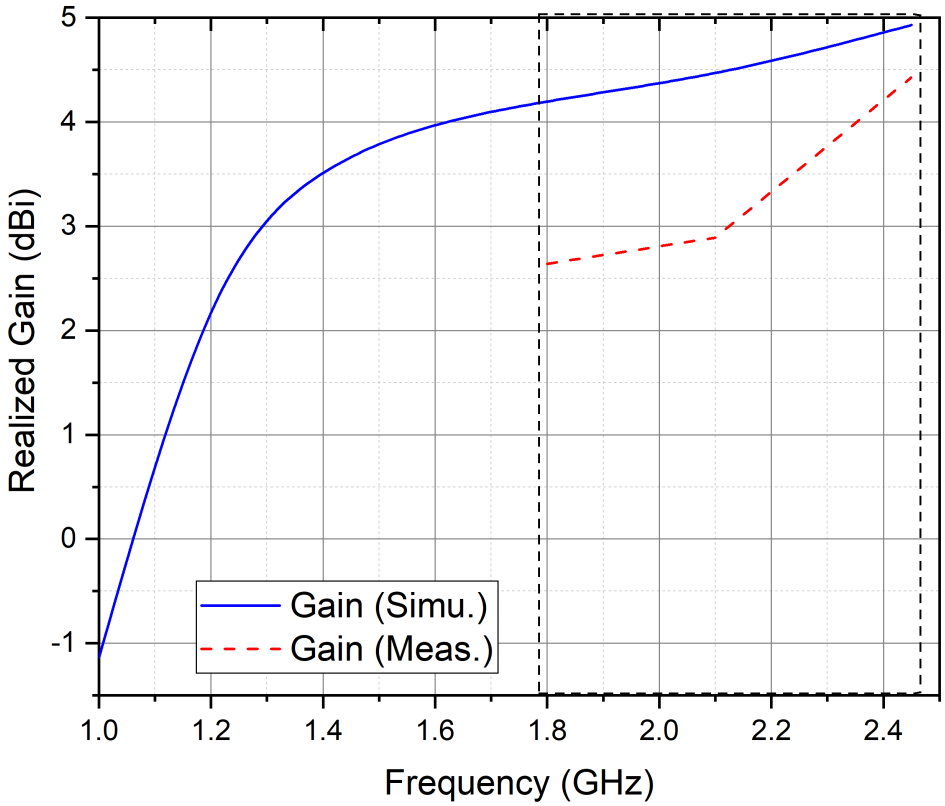

Figure 3.25: Simulated and measured realized gains.

CHAPTER 4

FUNDAMENTALS OF MICROWAVE RECTIFICATION AND RECTIFIER CIRCUITS

"I was taught that the way of progress was neither swift nor easy "

- Marie Curie, *physicist, chemist, and the first women to win the 1903 Nobel Prize in Physics and the 1911 Nobel Prize in Physics*

4.1 Introduction-Microwave Rectification

RF signals collected by the antenna is in the form of Alternating Current, AC with a sinusoidal waveform, and its polarity periodically changes between a positive value to a negative value in every half-cycle with respect to time. A voltage/current in the form of an AC cannot be utilized to power-up most electronic devices such as batteries, sensors and DC-DC step-up ICs. Therefore, an AC voltage/current has to be converted into a Direct Current, DC, which is in the one direction meaning its polarity does not alternate with respect to time. The conversion of an RF signal with a frequency of 300 MHz to 300 GHz to a DC power can be defined as a Rectification of Microwave Energy (or Radio Frequency Energy). The rectification of an RF signal is an essential stage of the RF energy scavenging system chain.

The conversion of an RF signal, coming from the receiving antenna, into a rectified DC power can be achieved utilizing a Schottky- diode which is commonly exploited as a rectifying element in an RF energy harvesting system.

When an RF signal reaches to the junction of the Schottky- diode due to its inherently non-linear characteristic, a variety of spectral components: 1) DC, 2) fundamental frequency and 3) harmonics of the fundamental frequency are produced at a certain level at the output of the rectifying device [71]. Figure 4.1 depicts a simple half-wave RF-to-DC converter consisting

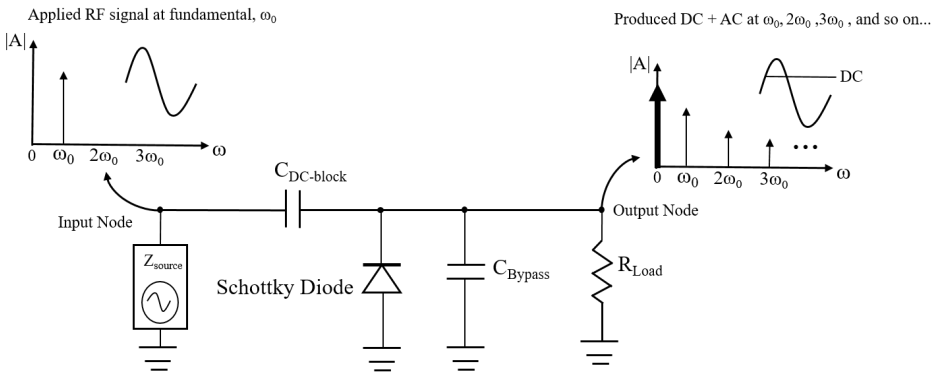

Figure 4.1: The schematic of a parallel connected Schottky-diode and the spectral components at the output node.

of a Schottky- diode.

In the scope of the RF-to-DC rectification for this work, a Schottky- diode is exploited as well. Therefore, an adequate understanding is required for the followings:

1) Both the physical and electrical characteristic of it will be shortly explained to obtain a good understanding of the inherent of a Schottky-diode.

2) The non-linear behavior of a Schottky-diode which determines the RF-to-DC conversion efficiency will be explained in the level of theory.

3) A simple experiment will be given to understand the effect of both fundamental and electrical parameters of a Schottky- diode on the conversion loss, the RF-to-DC conversion efficiency, and the DC voltage at the output. The experiment aims to demonstrate which parameter of a Schottky- diode plays a vital role in the RF-to-DC efficiency. A good understanding is required for both to chose a suitable Schottky- diode and to optimize the RF-to-DC efficiency in an enhanced way.

4) The RF input impedance of the Schottky- diode (in the meantime the Schottky- diode-based rectifier circuit) profoundly shows a non-linear behavior; therefore it should be determined to realize a matching network. Hence, both the theoretical analysis and the simulated input impedance of the Schottky- diode will be given further.

In this chapter, it is worth to notice that all the simulations of the Schottky- diode are carried out by means of Advance Design System (ADS). Two different kinds of simulator have been utilized: 1) Large Signal S-Parameter (LSSP), in order to find the large signal input impedance of the Schottky- diode and the rectifier circuit 2) Harmonic Balance (HB) simulator, to determine the level of the rectified DC component, the fundamental frequency and the

harmonics of the fundamental frequency at the output of the rectifying circuit, respectively.

4.2 Fundamental Properties and Electrical Characteristic of a Schottky- Diode

Schottky barrier diodes are used most often for the microwave rectification. The formation of a Schottky barrier is a metal-to-semiconductor that makes a Schottky- diode is preferable in the microwave frequencies over the other types of diodes like p-n junction diodes to be exploited in the RF Energy Harvester.

4.2.1 Fundamental Properties of a Schottky - Diode

1. Fast recovery: The existence of a metal-to-semiconductor junction in a Schottky- diode is an advantage concerning a current flow which involves only the majority-carriers (n-type or p-type), so as it is called as a "majority-carrier" device. That is to say, for an n-type Schottky- diode, the forward current emerges from the flow of the electrons from the n-type semiconductor to the metal, in the same manner, for a p-type Schottky- diode, it arises with the movement of the holes from the p-type semiconductor to the metal. Therefore gradual and arbitrary recombination of the majority-carriers (n-type or p-type) does not take place in the junction of a metal-to-Semiconductor as it happens in the p-n junction. In the p-n junction, the minority charges are accumulated and a substantial amount of time is required to remove the charges under the sudden changes in forward-biased to reversed-biased, or vice versa, from the p-n junction. Therefore, being a majority-carrier device makes a Schottky-diode very attractive in the microwave frequencies in which the fast switch response is required. The recovery time for a Schottky-diode can be downscaled less than few pico-seconds when the transition of the forward-biased to reverse-biased occurs instantly [72].

2. Low barrier height: Barrier height of a diode is an essential property since it profoundly determines the forward voltage drop on a diode. A Schottky junction can be fabricated by varying barrier heights whereas, for a p-n junction, the barrier height is often unaltered. Therefore, Schottky junction provides another advantage over a p-n junction; a forward voltage can be substantially reduced by the formation of a Schottky barrier with lower barrier height when it is compared to a p-n junction [72]. As it is extended in [73], various types of barrier heights are available for a Schottky- diode. Notably, a Schottky- diode with low barrier or zero bias detector (ZBD) barrier can be conveniently selected as a rectifying element particularly at the level of low RF power densities.

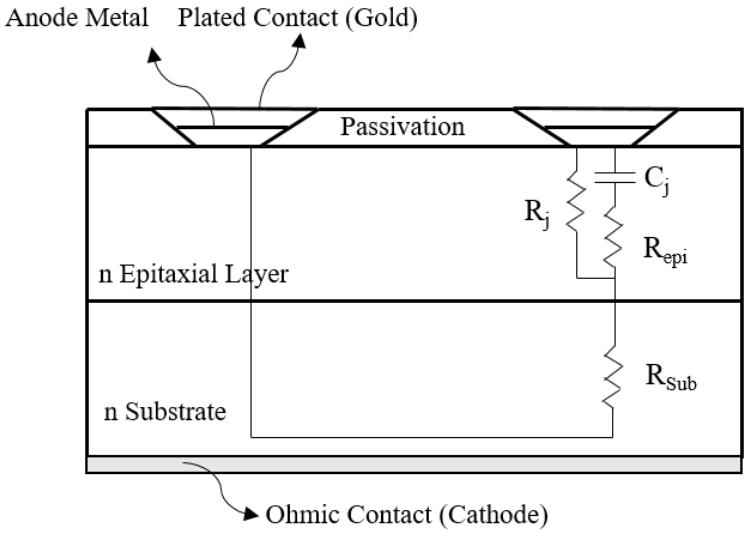

Figure 4.2: Cross-section of a Schottky- diode.

4.2.2 Electrical Characteristic of a Schottky - Diode

A Schottky junction is manufactured by the coating of a proper barrier metal on a substrate such as Gallium Arsenide (GaAs) or Silicon (Si) which is called as an epitaxial semiconductor layer. The performance and stability of a Schottky- diode over the varying conditions can be enhanced by creating a passivation zone that is resulted from when a silicon-based Schottky-diode is passivated with silicon nitride and silicon dioxide, or both, as seen in Figure 4.2.[1]

The equivalent circuit parameters of a Schottky Barrier Diode is depicted in Figure 4.3 in which C_p and L_p denotes the plastic-package parasitics. The effects of the package parasitics can be alleviated by a suitable impedance matching circuit. However, the effects of the other equivalent circuit parameters are mostly inherent and altering with the RF power levels, and their effects on the input impedance of a Schottky-diode, RF-to-DC conversion efficiency, and the rectified DC power cannot be easily tuned out by a matching network.

4.2.2.1 *Junction capacitance*

The depletion region of a Schottky-diode is formed between the doped semiconductor region and the metal layer as seen in Figure 4.2. Due to the depletion layer is an insulator and it distinguishes two conductive layer, it can be treated as a parallel-plate capacitor. So, C_j

[1] Figure is drawn by the author using the information given in [74]

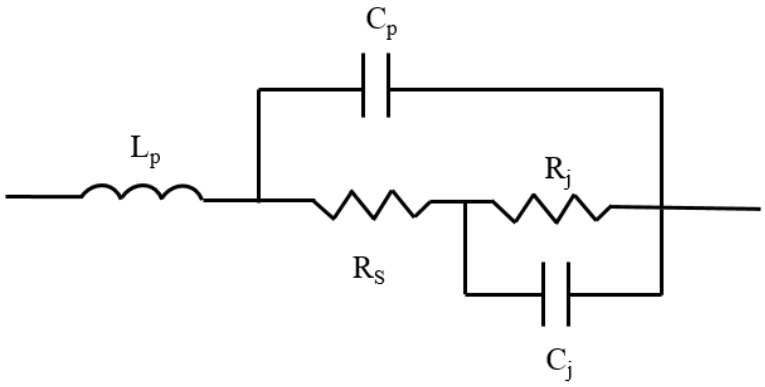

Figure 4.3: Circuit equivalent of a Schottky- diode.

represents the capacitance of the depletion region of a Schottky-diode, also known as parasitic junction capacitance and the value of it can be approximated as given in [75]:

$$C_j = A\sqrt{\frac{q\varepsilon_0\varepsilon_s N_D}{2(V_{bi}+V_j)}} \tag{4.1}$$

where A represents the active area of the Schottky- diode, q is the magnitude of the electronic charge, ε_s is the dielectric constant for the semiconductor layer, ε_0 depicts the dielectric constant of the free space, N_D is the density of the doping profile, V_{bi} is the built- in voltage of the Schottky- diode and V_j is the voltage which is applied on a Schottky junction.

As it can be seen from (4.1), C_j is affected by many parameters, even though doping profile, dielectric constant of the semiconductor, and built-in voltage are adjusted in an effective way to reduce the value of it, however, the effect of the applied voltage will dominantly alter its dynamic value. That is to say, when a Schottky- diode is exploited as a rectification device, the capacitance value will increase in the level of low RF power densities which results in highly capacitive input impedance at low-level RF power whereas, while the RF power level increasing, the capacitance value of C_j will start to decrease.

4.2.2.2 *Series Resistance*

Another critical parameter of a Schottky- diode is parasitic series resistance R_s.

$$R_s = R_{epi} + R_{sub} = \frac{L}{q\mu_N N_d A} + 2\rho_s\sqrt{\frac{A}{\pi}} \tag{4.2}$$

where, L indicates the thickness of the epitaxial layer, q is the charge of the electrons, μ_N

is the mobility of electrons (for n-type, for p-type of Si, it is the mobility of the holes), N_d represents the density of doping for the epitaxial layer, A is the area of the Schottky contact, ρ_s is the resistivity of substrate. As it can be seen from (4.2), the series resistance of a Schottky-diode inherently changes with both properties of an epitaxial layer and a substrate. It cannot be tuned out and alleviated by an impedance matching network. Besides, R_s does not have a contribution to the rectified DC power. An RF power is just dissipated on R_s in the form of heat, therefore R_s is a crucial parameter for the characterization of an RF-to-DC conversion loss [76].

4.2.2.3 *Junction resistance*

The last important parameter of a Schottky- diode is the junction resistance R_j, also known as a video resistance. It can be qualified as given [77]:

$$R_j = \frac{nkT}{q}\left(\frac{1}{i_b + i_s}\right) \tag{4.3}$$

where n is ideality factor, T is a temperature in Kelvin, i_b is the applied bias current, i_s is the saturation current. R_j is treated as an effective resistance and which creates junction losses while the input RF signal at the fundamental frequency is converting to the rectified DC power. Therefore, the junction losses due to the R_j alter with the frequency. Besides, R_j plays a crucial role in optimal load resistance selection. As it can be seen in (4.3), R_j changes with the bias current, at low RF power levels which means bias current is very low, R_j posses high values, which results the optimal load resistance value is also high in ohm(s). In the same manner, when RF power levels increase, bias current to the Schottky- diode junction also increases which results in lower values in junction resistance and optimal load resistance in ohm(s) [76].

4.2.2.4 Approximation of the Schottky- diode parameters on conversion loss

In order to comprehend the effects of the given parameters all together on conversion loss, a useful approximation is given as [78]:

$$L = 1 + \frac{R_s}{R_j} + \omega^2 C_j^2 R_s R_j \tag{4.4}$$

As it can be seen from (4.4), as the operating frequency increases, the conversion loss is expected to increase rapidly. On the other hand, R_j dominantly influences the conversion loss

since R_j profoundly depends on the bias current levels meaning that it can be directly related to the input power so then the conversion loss increases as the input power levels increases. As it can be seen from the contribution of the R_j to the conversion loss, "zero bias Schottky-diodes" should be used rather than other types. In order to reduce the conversion loss in a Schottky- diode, a low value of both R_s and C_j is required. However, manufacturing of both R_s and C_j with low values is not an easy task as it is seen from (4.1) and (4.2), both parameters of a Schottky- diode shows reverse relationships in terms of their dependents [77].

4.2.3 Nonlinear Analysis - Behavior of the Schottky- Diode Under Small and Large Signal Condition

In RF circuit design, non-linear components such as a bipolar junction transistor, a field-effect transistor, and a Schottky/p-n junction diode have been approximated to describe their electrical behavior and their output components under two conditions [79],[80];

1. *Large Signal Approximation* : If an externally applied voltage on the non-linear element is in the form of AC signal having so "large" fundamental component, called as *Large Signal*. Under the large signal condition, the electrical characteristics and the output components (DC and AC) of the non-linear elements are approximated in more "linear" regime in the Current vs Voltage (or any other representative curve i.e. Input power vs. Voltage, Base-Emitter Voltage vs. Collector Current etc.) curve of the corresponding component as shown in Figure 4.4.

2. *Small Signal Approximation*: If an externally applied AC voltage on the non-linear element has a "small" fundamental component, the signal is called as *Small Signal*. Under the small signal condition, the electrical parameters and the output components of the non-linear element are evaluated in "slightly non-linear" regime in the Current vs. Voltage (or any other representative curve, i.e. Input power vs. Voltage, Base-Emitter Voltage vs. Collector Current etc.) curve of the corresponding component as shown in Figure 4.4.

As a beginning, the non-linear behavior of a Schottky- diode will be concisely explained with the exponential relationship between current passing through the Schottky-diode and an externally applied voltage on the diode which can be expressed as given in [71]:

$$I_{diode} = I_s(e^{\frac{V_b}{nV_t}} - 1) = I_s(e^{\frac{(V_b external - R_s I_{diode})}{nV_t}} - 1) \tag{4.5}$$

where I_s represents the saturation current of the Schottky- diode, V_b is the voltage across the Schottky barrier, which is equal to a voltage applied externally to the Schottky- diode minus the voltage drop across the series resistance R_s of the diode, n indicates the diode ideality

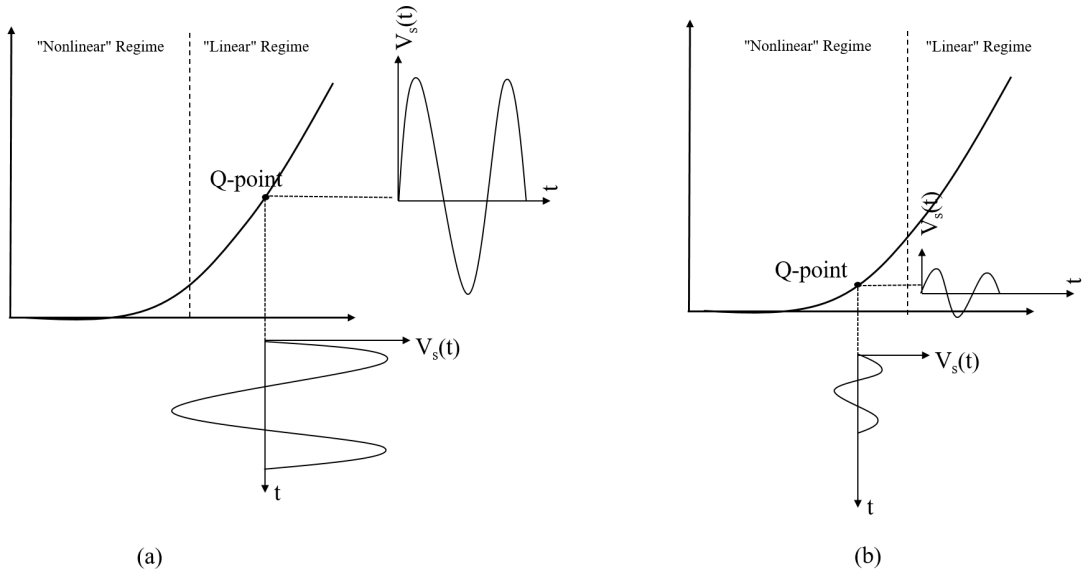

Figure 4.4: The representative I-V curve of a diode (a) operating under large signal condition (b) operating under small signal condition.

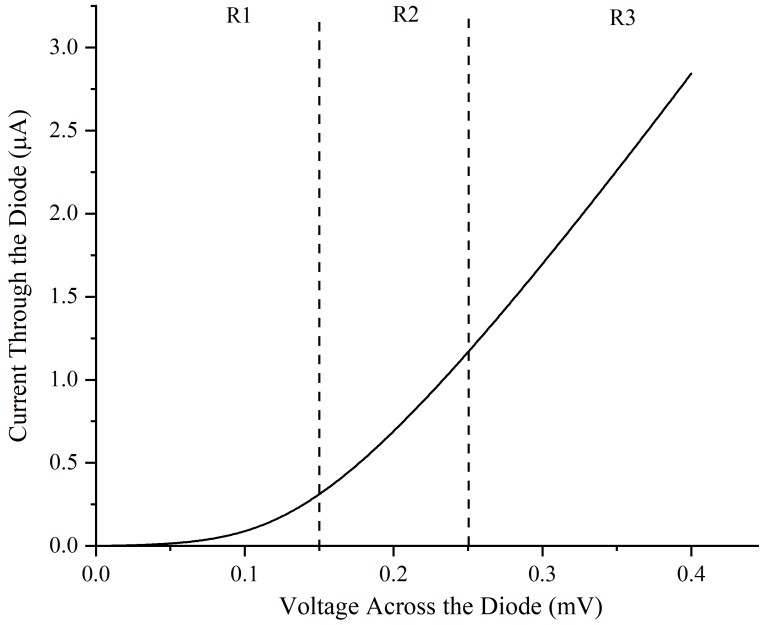

Figure 4.5: The simulated I-V characteristic of a HSMS 2850 model Schottky- diode.

Table 4.1: Schottky- diode parameters

Schottky- diode Type	R_s (Ω)	C_j (pF)	V_f (mV)	V_{br} (V)
HSMS 2860	6	0.18	250	7
HSMS 2850	25	0.18	180	3.8
SMS 7630	20	0.14	150	2

factor, V_t is the thermal voltage of the diode. As it can be seen from (4.5), it is expected that when the externally applied voltage is increased, the rate of the current passing through the diode grows exponentially. It can also be verified from the simulated I-V curve of a HSMS 2850 model Schottky-diode, shown in Figure 4.5.

The relationship between an externally applied input signal (RF) and a produced output signal (DC) can also be clarified by the I-V curve of a Schottky- diode. It can be divided into the three regions as it is shown in Figure 4.5 [81] & [82];

1. *Region 1 (R1)* : The first region is called as "Square Law" region. In this region, the quadratic curvature can be observed. That means the produced output signal (DC) predominately grows with the square of the available input power (RF) at the junction of the Schottky-diode. In this region, as the produced DC voltage in the diode internally determines the Q-point of the non-linear device, the behavior of the Schottky-diode in R1 is also called a "Zero Bias" operation.

2. *Region 2 (R2)* : In this region, as the proportionality of the input signal to the output signal is between quadratic and linear, the second region is called a "Transition" region.

3. *Region 3 (R3)* : In the last region, the output signal grows linearly with the input signal; therefore, it is called a "Linear" region. In this region, the diode behaves primarily as a switch, and the series resistance losses become more dominant compared to the other two regions.

If a small signal is applied on the Schottky- diode, the operation of the Schottky- diode is dependent on these first two regions, R1 & R2, and hence the RF-to-DC conversion efficiency is expected to increase as the operation of the diode closes to the third (R3) region. On the other hand, if a Schottky- diode is biased with the large signal amplitude, it is forced to operate at the third region, R3. As a consequence of this, even though the aggregate DC output voltage increases with the available input power since the series resistance losses are dominant at the third region, the RF-to-DC conversion efficiency is expected to decrease as input power increases [81].

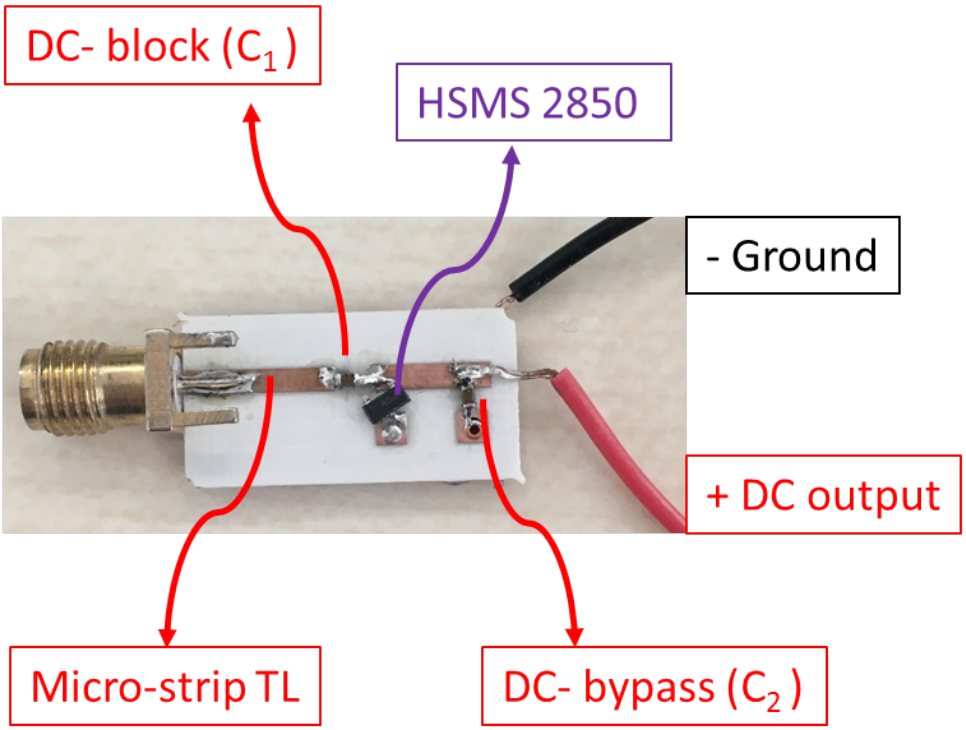

Figure 4.6: Schottky-diode detector with HSMS-2850 model.

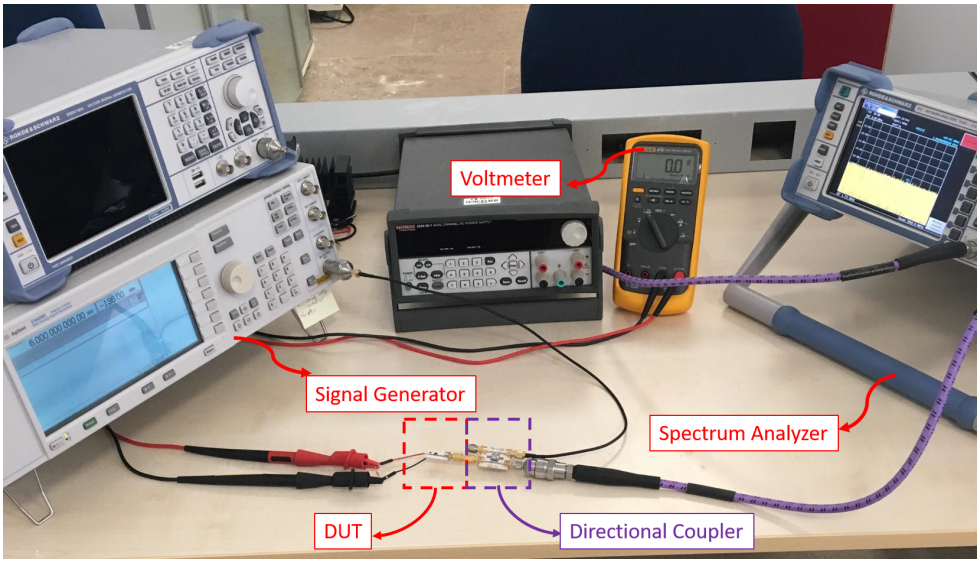

Figure 4.7: The setup for the loss characterization measurements for the Schottky-diode.

4.2.4 An Experimental Study for Schottky- Diode Choice

In order to obtain more specific understanding; how the diode parameters affect the RF-to-DC conversion loss, the RF-to-DC conversion efficiency, and the output DC voltage, an experiment was conducted with a simple detector circuit (Refer to Figure 4.6). The Schottky- diode of HSMS 2850, HSMS 2860 and SMS 7630, which are mostly exploited as a rectification device in the current literature, are selected for the laboratory measurements.

The Schottky-diode parameters for each corresponding diode are given in Table 4.1. Three identical Schottky-diode detector circuit has been implemented on the Roger4003C substrate as depicted in Figure 4.6. A 50 Ω Micro-strip transmission line with the width value of 1.8 mm and the length value of 8 mm has been inserted to mount the SMA connector at the input of the detector circuit. The surface-mounted device (SMD) capacitors with the value of C_1=4700 pF and C_2=4700 pF from Murata have been used as DC block and DC bypass capacitors, respectively. It is worth to notice; there is no matching network which has been inserted at between feed line and diode.

To determine the RF-to-DC conversion loss, the RF-to-DC conversion efficiency, and the output DC voltage for the different model of the Schottky- diodes, the experimental procedure steps as follows:

1. Three identical measurement setups have been built-up as seen Figure 4.7. It is important to notice that there is no externally applied DC bias to detector circuits while taking the measurements.

2. The Device Under Test (DUT) refers to the detector circuit as shown in Figure 4.6. The directional coupler of Mini Circuit with the model number of BCDA-10-25 has been inserted at between DUT and the spectrum analyzer. As there is no matching network at between 50 Ω feed line and the detector circuits, the reflected power from the input of the detector circuits should be observed at the different power levels for the Schottky-diode detector circuits. Therefore, by using the directional coupler, it is aimed to monitor the power flow through the input of the rectifier circuits as the signal generator power is swept.

3. The signal generator (Agilent E4428C) was connected to the input port of the directional coupler, and the power is swept at the frequency of 1.8 GHz.

4. The spectrum analyzer (R&S 2VL) is used to measure the amount of the received power as a function of frequency at the coupled - forward terminal of the directional coupler. The coupling value of the directional coupler has been taken from the data-sheet [83] and then the

input power flowing to the rectifying circuit is evaluated according to the data-sheet value. It is observed that as there is no matching network, there is a lot of reflected power from the input of the rectifying circuit to the input of the signal generator. Therefore, the presence of the power monitoring step is essential if there is no matching between the 50 Ω input of the signal generator and the rectifying device.

5. The output DC voltage is measured with voltmeter (Fluke) as the signal generator power is swept.

6. Since there is no input match between DUT and the signal generator (and Directional Coupler), the RF power coming from the source reflects in different amounts as the RF power at the signal generator changes. Therefore, the available power at the input of the detector circuit is considered instead of power available at the source. The conversion loss is evaluated as given:

$$L = \frac{P_{in}}{P_{DC,dBm}} \tag{4.6}$$

where P_{in} indicates the available input power at the input of the detector circuit in dBm, $P_{DC,dBm}$ is the DC power in dBm which can be expressed as follows:

$$P_{DC} = 10 \times \log_{10}(\frac{V_{DC}^2}{R_L} \times 10^3) \tag{4.7}$$

where V_{DC} is the measured output DC voltage on the load and R_{load} is chosen as 10 kΩ for all detector circuits. The purpose of the load at the order of kΩ is to easily detect the DC voltage on the load at the low power levels.

As a starting point, Figure 4.8 indicates the conversion loss as a function of available power at the input of the detector circuits. As it can be seen from the measurement results, the conversion loss for the HSMS 2860 is lower compared to other types at the both low and high RF input power levels. As the HSMS 2860 has a lower series resistance value than the other types and the junction capacitance for three types of Schottky-diodes are almost the same, lower conversion loss from the model of HSMS 2860 is well expected.

On the other hand, there is a very interesting observation compared to the conversion loss of the SMS 7630 and HSMS 2850. Since both the series resistance and the junction capacitance of the SMS 7630 is slightly lower than the HSMS 2850 (Refer to Table 4.1), it was expected that the conversion loss in SMS 7630 is less than HSMS 2850. However, there is a slight difference between the conversion loss of those two Schottky-diodes. On the contrary to the

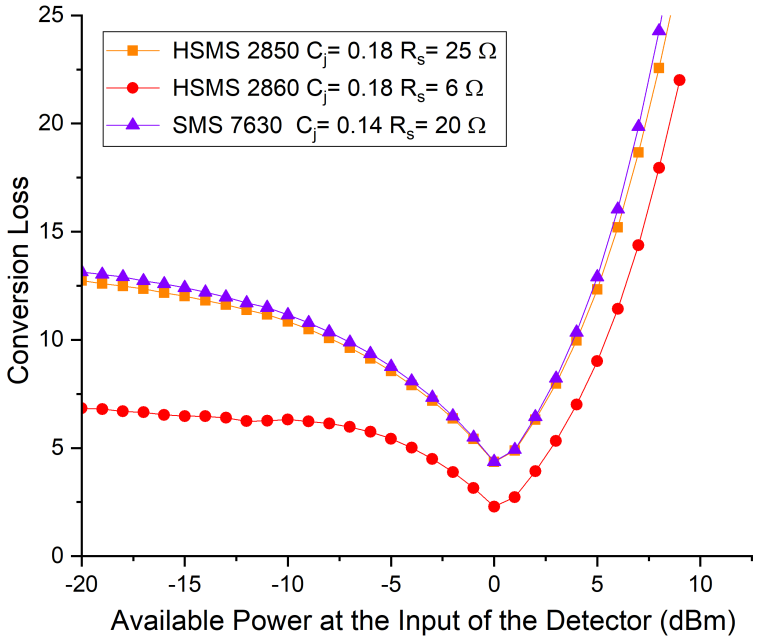

Figure 4.8: Measured RF-to-DC conversion loss as a function of the available power at the input of the detector at 1.8 GHz when R_{load}=10 kΩ.

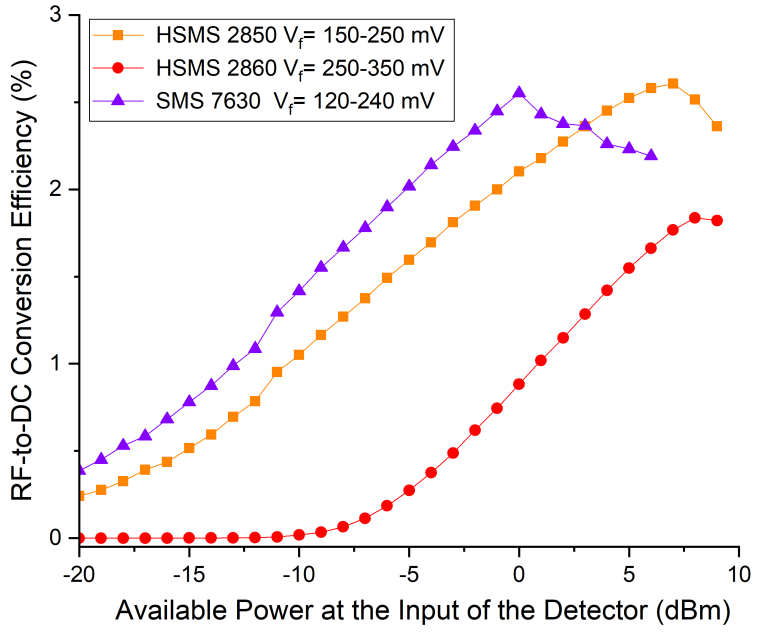

Figure 4.9: Measured RF-to-DC conversion efficiency as a function of the available power at the input of the detector at 1.8 GHz when R_{load}=10 kΩ (without matching network).

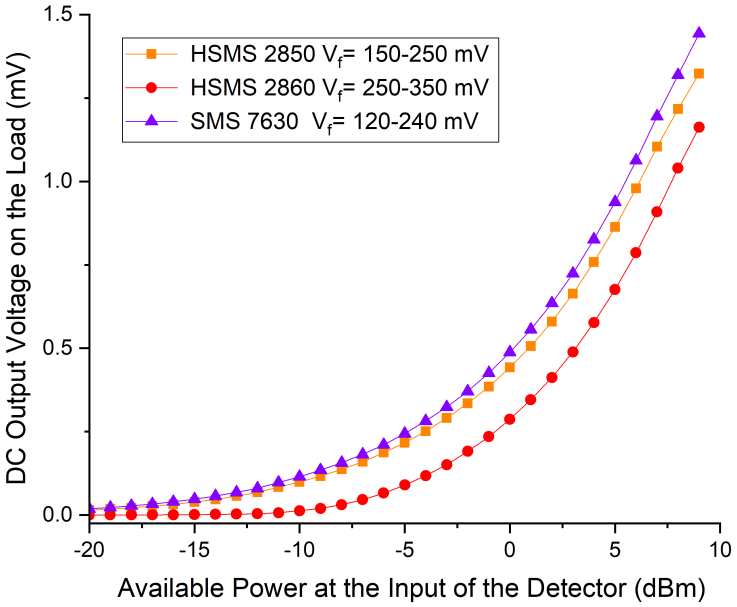

Figure 4.10: Measured output voltage on the load as a function of the available power at the input of the detector at 1.8 GHz when R_{load}=10 kΩ (without matching network).

expectations, as it is observed from the conversion loss curve, SMS 7630 features a little bit more conversion loss. Even though the measurements are repeated several times for both detector circuit with SMS 7630 and HSMS 2850, this unforeseeable measurement result might be due to the SOT-package manufacturing.

As it is seen from the Figure 4.8, HSMS 2860 gives the lowest RF-to-DC conversion loss among the other types; however, comparison of the conversion losses between the diodes are not enough to evaluate the performance of the Schottky-diodes as a rectifying element. Therefore, the conversion efficiency and the output DC voltage levels also should be investigated to choose the best suitable Schottky-diode as a rectification device.

The conversion efficiency can be evaluated for as follows:

$$\eta_{RF-DC} = \frac{P_{DC}}{P_{in}} = \frac{V_{DC}^2}{P_{in} R_{Load}} \tag{4.8}$$

where P_{DC} is the DC output power, P_{in} is the RF power to the input of the detector, V_{DC} is the output DC voltage, R_{Load} is the load resistance.

Figure 4.9 indicates the RF-to-DC conversion efficiency as a function of the available input power at the detector circuit for the different types of diodes. As it can be observed from the measurements, the RF-to-DC conversion efficiency (with no matching condition) of the detector circuit realized with SMS 7630 is higher than the others. The reason is that the

forward voltage of the diode is lower than the other type of Schottky-diodes. Even though HSMS 2860 has the lowest RF-to-DC conversion loss, the HSMS 2860 features the lowest RF-to-DC conversion efficiency since it has the highest forward voltage drop. In the same manner, the output DC voltage of the Schottky-diodes (shown in Figure 4.10) is profoundly determined by the forward voltage drop.

Further observation of the RF-to-DC conversion efficiency is that the verification of the assumption done in the section of 4.2.3. As it is seen from Figure 4.9, the RF-to-DC conversion efficiency shows the increasing trend while the available input power increases, however, at one point in the high power region, it starts to decrease as it is expected from the non-linear analysis of a Schottky-diode.

In addition to the non-linear analysis, the point in which the RF-to-DC efficiency starts to decrease can be determined by "Breakdown voltage." Breakdown effect can be explained as in which the voltage on the diode junction surpasses the breakdown voltage V_{br} of the Schottky-diode, at that point RF-to-DC conversion efficiency is expected to decreases with increasing input RF power [84].

As a results of the measurement of the Schottky-diodes, even the electrical parameters of a Schottky-diode C_j and R_s have an impact on the RF-to-DC conversion efficiency, the conversion loss, and the output DC voltage, the RF-to-DC conversion efficiency, and the output DC voltage is profoundly determined by the forward voltage, V_f of the Schottky-diode.

4.2.5 Input Impedance Analysis of a Schottky- Diode

The input impedance analysis of a Schottky- diode plays an essential role in order to design an impedance matching network. Therefore, how the input impedance of the diode and diode based-rectifier circuit changes with the design parameters such as frequency, load value, diode's parameters, and input power levels, should be understood in the level of the measurements, theory, and simulations. There are different ways to determine the input impedance of a diode as following in the subsections;

4.2.5.1 Source-pull Measurements

Source-pull measurement is an experimental procedure in order to obtain an input impedance of a diode. The setup of a source-pull measurement is shown in Figure 4.11 in detail. The method can mainly be described as the impedance of the source seen by the diode (DUT) and the input RF power at the fundamental frequency are varied with a "computer-controlled

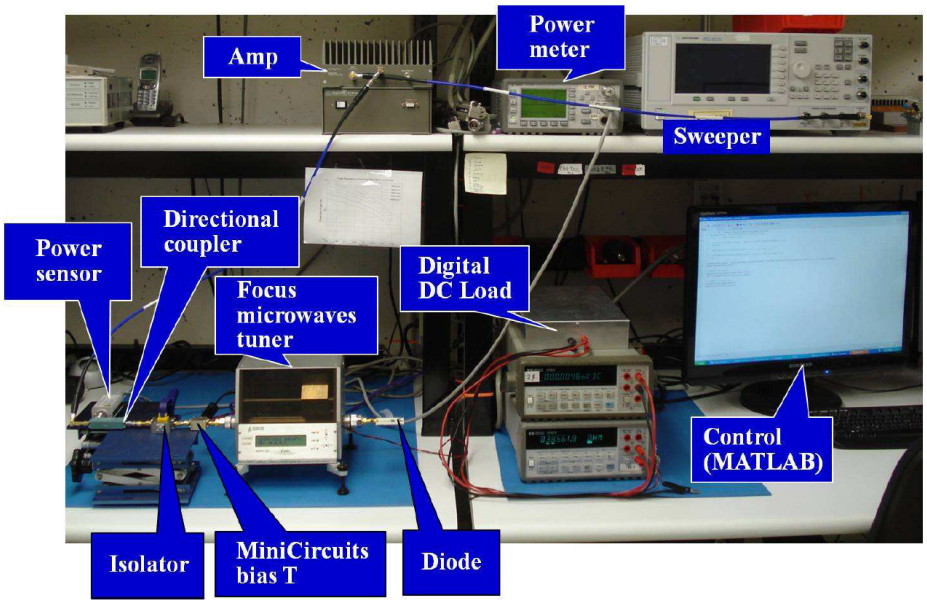

Figure 4.11: Photograph of the source-pull measurement setup [85].

tuner" at the same time, the aggregated DC voltage across the load is measured and the resulted input impedance of the diode/rectifier circuit can be observed on Smith Chart [85].

Even though source-pull measurement has an advantage since the input impedance contours of the diode can be observed at the points in which the diode operates efficiently, the measurements are not an easy task. Besides, the method has limitations such as the implementation of the pre-matching network and TRL (Thru, Reflect, Line) calibration sets require rigorous standardization. The other limitation of the source-pull technique is the value of maximum RF power at the input of the diode. At the high levels of the RF power, the evaluations of the input impedance of a diode are complicated and not reliable [85].

4.2.5.2 Time Domain Analysis - Theoretical approach

The complex input impedance (or RF impedance) of a Schottky- diode can be derived from the time domain analysis. As a starting point, in order to derive the RF impedance of a Schottky-diode following assumptions are given [84]:

1. The input impedance of the diode at the DC and harmonic frequencies are neglected (accepted as infinite at DC and harmonic frequencies)

2. The input RF signal is accepted as only consisting of the fundamental frequency component.

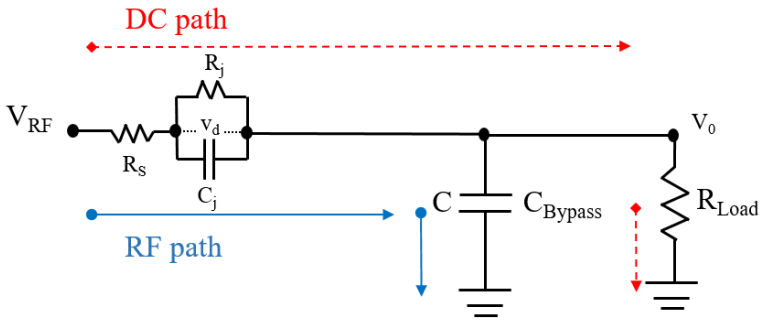

Figure 4.12: Series diode circuit with the equivalent circuit of the Shottky–diode .

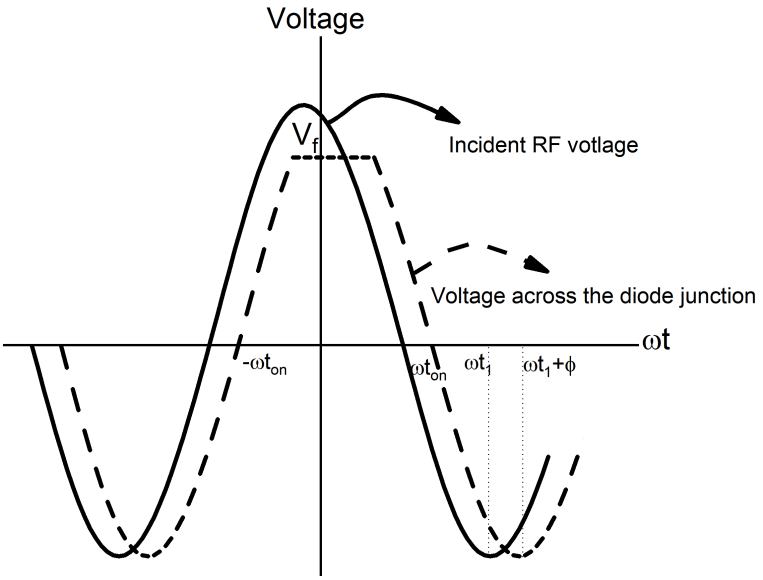

Figure 4.13: Time-domain waveform of the diode.

3. The produced harmonic components across the intrinsic diode junction are neglected.

4. The forward voltage drop across the Schottky- diode junction (V_f) is constant during the period in which the diode current conducts in the forward direction.

5. The bypass capacitor (Refer to Figure 4.12) is accepted as an ideal short-circuits at the corresponding frequency of interest in the time-domain analysis.

The time-domain waveform of the diode voltage shown in Figure 4.13. Due to the junction capacitor of the diode, there is a phased delay (ϕ) between incident RF signal and the voltage across the diode. The incident RF signal can be denoted as follows [84]:

$$V_{RF} = V_{RF1}\cos(\omega t) \tag{4.9}$$

$$v_d = \begin{cases} v_{d0} + v_{d1}\cos(\omega t) & \text{If Diode is turn-off} \\ V_f & \text{If Diode is turn-on} \end{cases} \tag{4.10}$$

where V_{RF} is the input RF signal at the input of the series diode which consists of only the fundamental frequency components of (V_{RF1}). v_d is the voltage across the intrinsic diode junction as indicated in Figure 4.14. v_{do} and v_{d1} are the DC and the fundamental frequency components of the voltage of the diode at the junction, respectively.

The DC and RF signals follow the practical paths which are separated with the blue and red line as shown in Figure 4.12. The RF current passing through the diode can be expressed as:

$$i_{RF} = I_s(e^{(V_{RF1}-V_0)/V_t} - 1) \tag{4.11}$$

where V_t is the thermal voltage and V_0 is the voltage across the load which can also denoted as:

$$V_0 = I_{load}R_{load} \tag{4.12}$$

By substituting (4.12) into the (4.11), the diode current can be evaluated in terms of the input RF voltage across the diode and can be given as:

$$i_{RF} = I_s(e^{(V_{RF1}\cos(\omega t-V_0)/V_t} - 1) \tag{4.13}$$

As it is mentioned before, when the RF signal is applied to the diode; the DC, fundamental, and harmonics are generated by the diode. Therefore, the exponential form of the current should be expressed as the sum of the DC, fundamental, and harmonics. A good way to approximate the exponential form of the diode current as a sum is to use the Bessel's function series expansion. It can be denoted as given in [86]

$$e^{\cos(\omega t)} = \overbrace{\underbrace{B_0(x)}_{\text{DC component}} + \underbrace{2\sum_{i=1}^{\infty} B_i(x)\cos n\omega t}_{\text{fundamental and harmonics}}}^{\text{sum of the DC, fundamental, and harmonics}} \tag{4.14}$$

where $i = 1$ the term indicates the fundamental frequency $i = 2$ represents the second harmonic of the fundamental frequency and so on. As it is assumed at the beginning of the analysis, since the harmonics are neglected, by using (4.14), the total current flowing through the diode can be denoted as:

$$I_{total} = \underbrace{I_{DC}}_{\text{DC current}} + \underbrace{2I_s e^{-V_0)/V_t} B_1(\frac{V_{RF1}}{V_t}) \cos \omega t}_{\text{fundamental}} \tag{4.15}$$

The RF input impedance of the diode at the fundamental frequency is expressed as:

$$Z_{in} = \frac{V_{RF1}}{2I_s e^{-V_0)/V_t} B_1(\frac{V_{RF1}}{V_t}) \cos \omega t} \tag{4.16}$$

As it can be seen from (4.16), the input impedance of the diode mainly depends on the incident RF power level, load resistance value (refer to (4.12)), and the operating frequency.

4.2.5.3 Large Signal Scattering Parameters and Harmonic Balance

The simulation of Large Signal Scattering Parameters (LSSP) is commonly exploited to compute the input impedance of a Schottky- diode (or non-linear circuit element). The LSSP simulation tool of ADS evaluates Large-Signal S-parameter for non-linear circuits using the Harmonic Balance (HB) technique. Since the harmonic balance solution takes account the harmonics effects of the non-linear circuit, not only the variation of the input impedance of the diode but also the RF-to-DC efficiency, the output voltage can be determined using both LSSP and HB simulations with varying input power levels.

Large-Signal S-Parameters can be expressed as the ratio of the reflected and incident waves as Small Signal S-Parameters [87]:

$$S_{ij} = \frac{B_i}{A_j} \tag{4.17}$$

where A_j and B_i represent the incident and reflected wave, respectively. Further, they can be expressed as :

$$A_j = \frac{V_j + Z_{0j} I_j}{2\sqrt{R_{0j}}} \tag{4.18}$$

$$B_i = \frac{V_i + Z_{0i}^* I_i}{2\sqrt{R_{0i}}} \tag{4.19}$$

where V_i and V_j represent the Fourier coefficients of the voltages at the corresponding ports i and j at the fundamental frequency. I_i and I_j represent the Fourier coefficients of the currents at the corresponding ports i and j at the fundamental frequency. Z_{0i} and Z_{0j} represent the reference impedances at the corresponding ports i and j and R_{0i} and R_{0j} indicate the real parts

of the Z_{0i} and Z_{0j}. Large Signal S-parameters and the input impedance at the reference port can be extracted using Harmonic Balance which calculates the currents and voltages at the corresponding port(s).

4.3 Schotky Diodes as a Rectifier Circuit

A rectifier circuit is an essential part of a rectenna since it predominantly determines the overall RF-to-DC conversion efficiency. The choice of the rectifier topology is a challenging issue for the energy harvester. As it is shown in [81], when the number of Schottky- diode in the rectifier configuration is increased, the RF-to-DC conversion efficiency decreases since the diode losses increase. On the other hand, as the number of Schottky–diode increases, the aggregated DC voltage increases.

As it is for every design, there are trades off between the output DC voltage and the RF-to-DC conversion efficiency. Therefore, the configuration of the Schottky-diode based rectifier circuit can be chosen based on a system level requirements such as whether DC output voltage is required in high level or it is utilized directly to the load, or it will be amplified by the DC-DC step-up converter.

In the scope of this thesis, a voltage doubler rectifier will be considered, and hence, the operation principle and the input impedance analysis of a Schottky- diode based voltage doubler are summarized in the following subsections:

4.3.1 The Operation Principle of a Voltage Doubler

In Figure 4.14, a voltage doubler rectifier which consists of two series diode oriented so as to double the output DC voltage is depicted. The working principle of the voltage doubler is given as in the following. As a beginning, it is necessary to make the consequent assumptions;

1. Diodes in the given circuit are close to ideal; they have zero current in the reverse direction, and they perfectly conduct in the forward direction; however, they have a non-zero threshold voltage, $V_{f,diode}$. Moreover, they are identical regarding the electrical properties.

2. The DC-block and -bypass capacitors are considered as an ideal open- and short- circuit at the corresponding frequency of interest.

3. The rectifier circuit operates under steady-state condition.

4. RF power coming from antenna to rectifier input is fixed, and it produces a perfect sinusoidal voltage having a constant amplitude, V_{in} at both negative and positive cycle of the

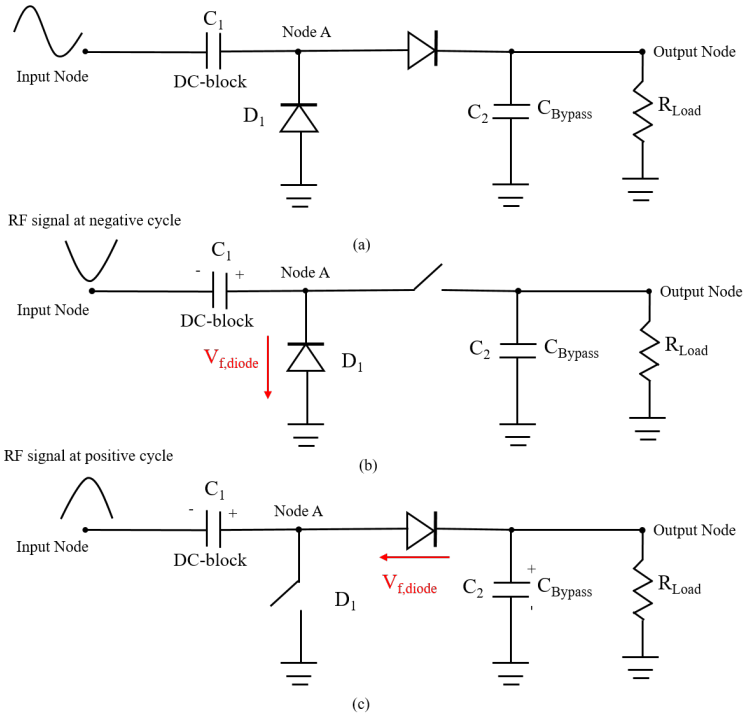

Figure 4.14: The schematic of (a) a voltage doubler (b) operation of the voltage doubler when the input signal at its negative cycle (c) operation of the voltage doubler when the input signal at its positive cycle.

sinusoidal signal.

When RF signal at its negative cycle, the first diode, D_1, conducts (behaves as a short-circuit) to charge the input capacitor of C_1. At the peak of the negative cycle of the input signal, the amplitude of the voltage on the C_1, at the node A, is equal to V_{in} - $V_{f,diode}$. Since the polarization of the input signal and the voltage on the capacitor is the same, there is no discharge path for the C_1, it maintains the value of V_{in} - $V_{f,diode}$, and acts as an additional power supply connected series with the input signal. At the moment, D_2 turns on via the voltage at the node A.

When RF signal changes its cycle from negative to positive cycle, D_1 acts as an open circuit (Reversed - biased, see Figure 4.14). D_2 starts to conduct (Forward - biased) and to charge up C_2 via the voltage on C_1 plus the value of the input signal voltage. The transition from conducting state to non-conducting state of the diodes does not occur instantaneously, the voltage on the C_2 gradually increases to the value of 2*(V_{in} - $V_{f,diode}$) and eventually flows through the load while the input signal completes its full cycle of operation. However, the voltage on the load is dependent on the value of the load resistance, R_{load} which determines

the amount of current drawn out from the C_2.

4.3.2 Input Impedance Analysis of a Voltage Doubler Rectifier- LSSP simulation

The input impedance analysis of a voltage doubler will be given in two ways as follows:

4.3.2.1 Closed-form Derivation of the Voltage Doubler

In [88] a very useful analysis of a voltage doubler is given regarding the closed- form equation for the input impedance and the rectifier efficiency. The input impedance of the voltage doubler is studied for two separate cases. The input impedance of the voltage doubler *Before Breakdown* as given [88]:

$$Z_{in,B_{br}} = \frac{\pi R_s}{(2\theta_{on} - sin2\theta_{on}) + jR_sC_j\omega(2\pi - 2\theta on + sin2\theta_{on})} \tag{4.20}$$

The relationship between $V_{in,Before-breakdown}$, θ_{on}, C_j, and V_f is expressed as followings:

$$V_{in,Before-breakdown}cos\theta_{on} = V_f + \frac{V_0}{2} \tag{4.21}$$

$$C_j = C_{j0}(1 + \frac{V_0}{2V_f})^{-M} \tag{4.22}$$

The input impedance of the voltage doubler *After Breakdown* as given:

$$Z_{in,A_{br}} = \frac{\pi R_s}{(2\theta_{on} + 2\theta_{br} - sin2\theta_{on} - sin2\theta_{br}) + jR_sC_j\omega(2\pi - 2\theta on - 2\theta_{br} + sin2\theta_{on} + sin2\theta_{br})} \tag{4.23}$$

The relationship between $V_{in,After-breakdown}$, θ_{on}, θ_{br}, and V_f is expressed as followings:

$$V_{in,After-breakdown}cos\theta_{on} = V_f + \frac{V_0}{2} \tag{4.24}$$

$$V_{in,After-breakdown}cos\theta_{br} = V_{br} - \frac{V_0}{2} \tag{4.25}$$

where M is the grading coefficient represent doping profile of the Schottky- diode, θ_{on} represents the phase of the input signal when the diode is conducted, θ_{br} is the phase of the input signal when the input signal surpasses the breakdown voltage of the diode.

It is important to notice that in subsection 4.2.5.1, the input impedance of the diode is derived regarding the amplitude of the input RF power and the voltage on the load. As it

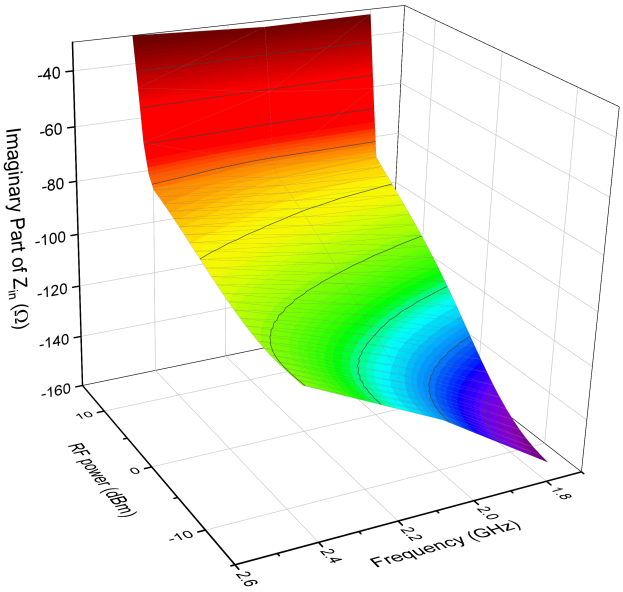

Figure 4.15: Simulated imaginary part of the input impedance of the voltage doubler as a function of input power and frequency when R_{load}=1 kΩ.

can be seen from the closed-form derivation dependents, the closed-form equation for the input impedance analysis gives a more insightful understanding of the input impedance. Another important conclusion from the closed-form derivation is the relationship between Z_{in} and its term starting with $jR_sC_j\omega$; this relation indicates that the imaginary part of the input impedance profoundly depends on the frequency and the electrical parameters of the diode.

As it is indicated in (4-20)- (4-25), the non-linear relationship between the parameters of θ_{on}, V_0, $V_{in,Before-breakdown}$, and $V_{in,After-breakdown}$ can be solved by means of mathematical programs such as MATLAB. As it is stated in [88] in order to solve the non-linear input impedance equations, the RF-to-DC efficiency should be approximated and also the reflected power from the diode junction to the input of the rectifier circuit should be neglected.

4.3.2.2 LSSP simulation of the Voltage Doubler

In order to obtain the input impedance variation of the voltage doubler with altering input RF power level, R_{load}, and the operating frequency, LSSP simulation is utilized. For the simulations, the Schottky- diode model HSMS-2850 is chosen, and hence the SPICE parameters are used as given in [76]. The value of R_{load} = 1kΩ and the operation frequency over the band from 1.8 to 2.45 GHz are selected. It is worth to notice that the input RF power range is chosen to cover relatively low (-15 dBm) and moderately high power level (10 dBm). The

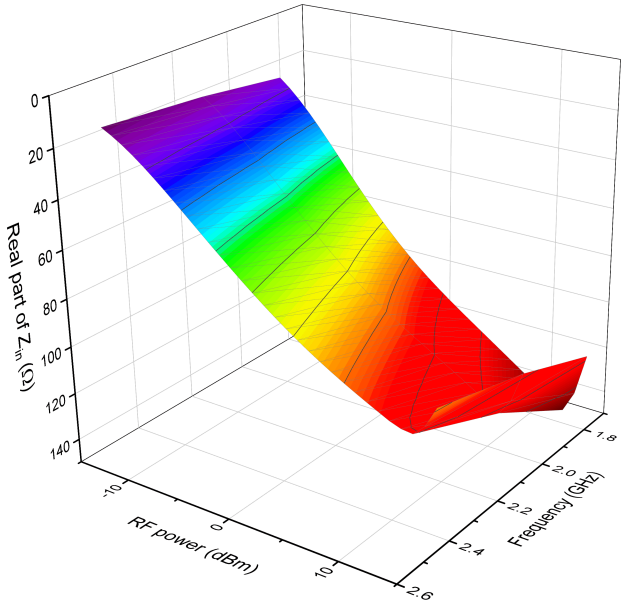

Figure 4.16: Simulated real part of the input impedance of the voltage doubler as a function of input power and frequency when R_{load}=1 kΩ.

large signal input impedance variation with respect to the RF power levels, load resistance value, and the frequency of operation is indicated in Figure 4.15-18, respectively.

As can be seen from Figure 4.15, the imaginary part of the input impedance of the rectifier increases with both frequency of operation and the input power levels. Even the input RF power level reaches the moderately high power levels, the input impedance of the rectifier is highly capacitive. Since both the DC-block &-bypass and junction capacitance of the Schottky profoundly affect the large signal input impedance of the diode.

On the other hand, the real part of the input impedance of the rectifier shows an opposite trend with changing frequency and power levels. Figure 4.18 indicates that when the frequency of operation increases the real part of the input impedance slightly decreases at the same power levels. However, at the same frequency level, when the RF power density increases the real part of the input impedance swiftly increases.

The load value of the rectifier is an important parameter not only for the RF-to-DC conversion efficiency but also for the large signal input impedance. As it is depicted in Figure 4.17 and Figure 4.18, the imaginary part of the input impedance of rectifier gradually decreases with increasing value of the load resistance. In the same manner, the real part of the input impedance of rectifier slightly drops with the increments in the load value.

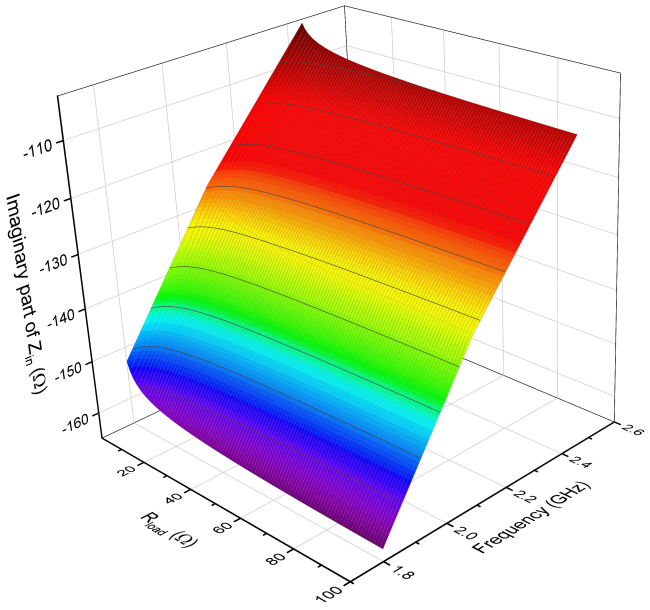

Figure 4.17: Simulated imaginary part of the input impedance of the voltage doubler as a function of R_{load} and frequency when input RF power P_{in}=-15 dBm.

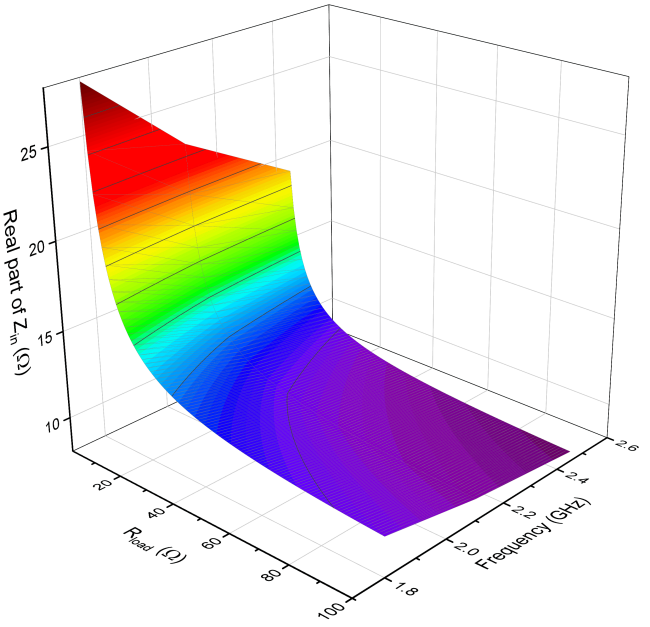

Figure 4.18: Simulated real part of the input impedance of the voltage doubler as a function of R_{load} and frequency when input RF power P_{in}=-15 dBm.

CHAPTER 5

IMPEDANCE MATCHING NETWORK DESIGN

"I used to not like being called a 'woman architect.' I'm an architect, not just a woman architect. The guys used to tap me on the head and say 'you're OK for a girl.' But I see an incredible amount of need from other women for reassurance that it can be done, so I don't mind anymore. "

- Zaha Hadid, *architect, winner of the Pritzker Architecture Prize*

5.1 Introduction- Maximum Power Transfer

In RF/ Microwave circuit design, matching and tuning are an essential part of a design process since it is required for the following reasons [71] & [89]:

1. In order to ensure the maximum power transfer between the generator (receiving antenna) and the load.

2. The signal-to-noise ratio of the system can be improved.

3. Since a matching network reduces the multiple reflections along the mismatched line, the phase and amplitude errors can be alleviated by the impedance matching network.

A conventional Matching Network (MN) is indicated in Figure 5.1. Considering an arbitrary complex impedance of the generator as given $Z_G = R_G + j * X_G$ and the impedance of the load as given $Z_{Load} = R_{Load} + j * X_{Load}$, the matching network can be utilized in two ways [71] :

1. If the matching network transforms the load impedance to the transmission line impedance as $Z_L = Z_0$, so then it ensures that there is no reflection from the load. This type of matching is called as *reflection-less matching*. The power delivered to the load can be expressed as :

$$P = \frac{1}{2}|V_G|^2 \frac{Z_0}{(Z_0 + R_G)^2 + X_G^2} \tag{5.1}$$

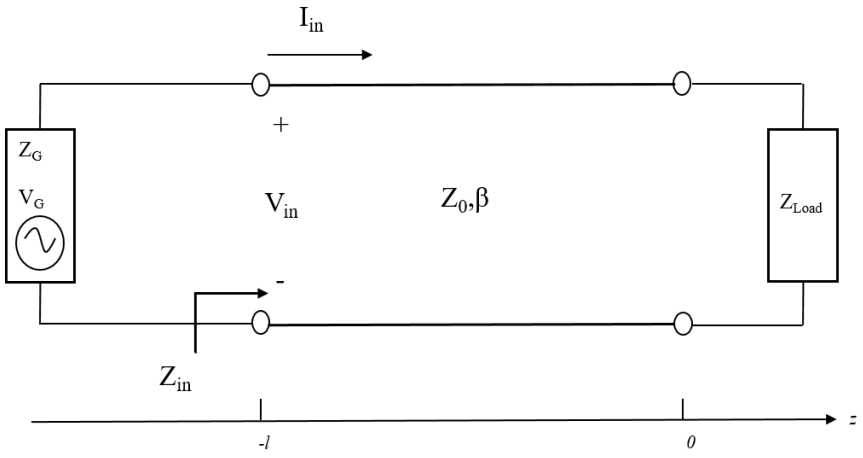

Figure 5.1: Reflectionless and conjugate matching of a transmission line.

2. If the matching network transforms the load impedance to the transmission line impedance as $Z_{in} = Z_G^*$, it yields the maximum power transfer to the load. This type of matching is called as *conjugate matching*. The power delivered to the load can be expressed as:

$$P = \frac{1}{2}|V_G|^2 \frac{1}{4R_G} \tag{5.2}$$

5.2 Fundamentals of a Matching Network

The implementation of a matching network can be realized with lumped elements (Mostly surface-mount device (SMD) capacitor/inductors) and microstrip lines such as stubs (open/short circuited), tapered-lines, a single section quarter-wave matching transformer. A variety of matching technique can be realized by looking at the load impedance and the source impedance. The Smith Chart, which is a graphical aid and an essential tool for the design of the RF circuit, can be used to determine the implementation of different types of matching techniques. In order to understand the freedom of choice for the implementation of a matching technique, an arbitrary complex load impedances, Z_1 & Z_2 shown on the Smith chart can be considered (refer to Figure 5.2).

Both red and blue lines shown on Smith chart indicate that the L-section (network) matching to get an input impedance match for the complex load impedance of Z_1 at the frequency of interest. L-section (network) matching is the simplest type of the MN consisting of a series/parallel L/C section. It can be utilized to obtain an input match by bringing the load impedance at the center of Smith chart. In this way, an arbitrary complex load impedance can

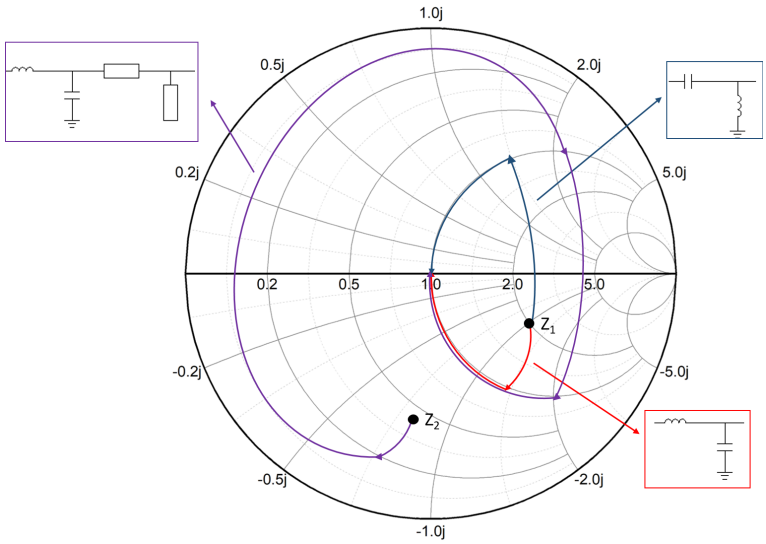

Figure 5.2: Arbitrary complex load impedances with matching network.

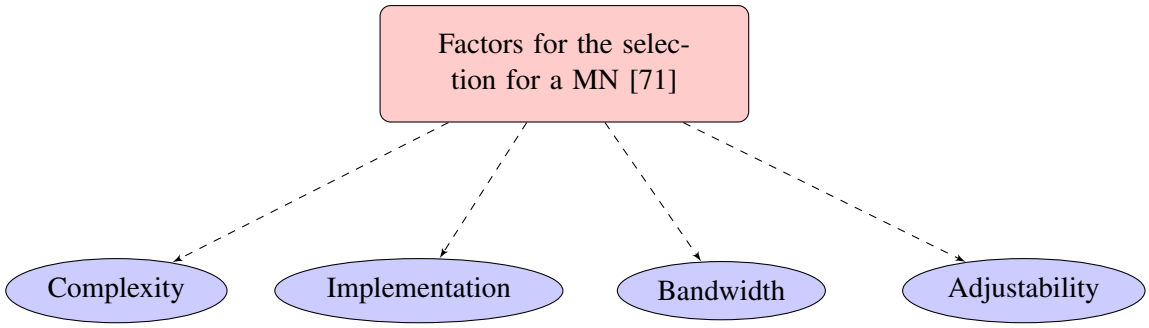

Figure 5.3: Illustration of the important factors for the selection of an MN.

be matched to a generator impedance (or transmission) resulting in both the real part of the input impedance and generator have the same value. The purple line can also be followed to obtain an input match to the 50 Ω using lumped and microstrip lines as indicated on Smith chart.

Even different kinds of matching technique can be implemented to realize an input match between a load and a generator (or transmission line), there are some essential factors that should be considered while choosing a topology for the matching network as follows [71]:

1. Complexity: The most straightforward design is always more preferable regarding cost, size of the overall system with MN, reliability, as well as losses due to the MN. As the large signal input impedance of a non-linear element varies with the input RF power, the load value, and the operation frequency, the realization of a MN for an RF/microwave circuit such

as power amplifiers (PAs) and rectifiers consisting of a non-linear element (transistor and diode) can be a more challenging issue without increasing the complexity of the circuit. Nevertheless, a complex MN employing micro-strip lines (mostly stubs)/ lumped elements may provide an input impedance matching at between antenna and rectifier circuit, but the micro-strip lines /the lumped elements create losses [90]. As it has been shown in [91], the surface currents also become dense in the region of the stub(s), resulting in both conductor and radiation losses becoming more considerable especially at the low input power levels. Therefore the complexity of the MN not only may degrade the performance of the rectifier but also may result in a bulky circuit which is difficult to be integrated into an RF energy harvester (or RF/microwave system).

2. Implementation: Depending on the RF/Microwave circuit requirements, an MN can be realized with just Micro-strip lines or just lumped elements (mostly SMD) or both. For example, in the scope of this thesis after all the experiences with both the micro-strip line and the lumped elements for the realization of an MN, the implementation of the lumped elements on a substrate is rather difficult compared to the micros-trip lines. This difficulty comes from the lumped element models being exploited in the simulation tools (ADS). Although the manufacturers provide the lumped models for both capacitors and inductors, the parameters of the models are extracted at the different frequencies compared with the frequency of interest for the design. Therefore, the provided models in a simulation and the real-life implementation of the lumped elements on the substrate might be entirely different from each other.

3. Bandwidth: A matching network aims to yield a perfect input match (zero reflection, $\Gamma = 0$) at a desired single frequency or over a band of frequencies. However, there are theoretical constraints between the maximum desirable reflection coefficient (Γ_{max}) and the bandwidth. The *Bano-Fano Criterion* which is the well-known qualitative analysis provides a good approximation for the parallel/series RC/RL loads regarding the trade-off between Γ_{max} and the bandwidth. Such an approach can be utilized to optimize the limitation between Γ_{max} and the bandwidth [92]. This criterion is convenient to design more realizable matching networks in practice.

In both passive (*i.e.*, power dividers, directional couplers) and active (*i.e.*, RF amplifiers and rectifiers) RF/microwave circuits, it is desired that they should operate at a specific frequency or over a wide frequency band. However, especially in active RF/microwave circuits, a wide-band operation can be accomplished at the expense of energy efficiency, gain, and linearity [71].

The operation (or fractional) bandwidth is also one of the important design factors for the rectifying circuit design with an MN. Although an MN provides an input matching over the broadband or at multi-band, it does not necessarily guarantee a high RF-to-DC conversion efficiency over the frequency band of interest. For example, a wide-band rectifier circuit with single series Schottky diode topology with HSMS 2850 has been proposed to cover all the Wi-Fi channels [93], the RF-to-DC conversion efficiency is between 48%- 50% on a 60 MHz for an input RF power of -10 dBm when the load value of 1200-1400 Ω. Whereas, for the same single series Schottky- diode with HSMS 2850, the RF-to-DC conversion efficiency is higher than 70% on a narrower bandwidth for the RF input power of -10 dBm when the load value of 1200-1400 Ω [94]. There might be two reasons for this; first one is that even the MN provides an input match between 50 Ω input impedance of the antenna (generator) and the rectifier circuit, it does not necessarily mean that the Schottky diode-can maintain its operation at the same efficiency level at even the range of a few MHz. RF-to-DC conversion efficiency for the Schottky diode also alters within the small range of the frequency. The second reason can be the high-quality factor of the rectifier circuit which is in the reverse relationship with the bandwidth, meaning that a narrower bandwidth indicates a high-quality factor of the rectifier circuit [71]. The high-quality factor of the rectifier circuit can passively amplify the output DC voltage of the rectifier [95]. Therefore RF energy harvesting from a narrower bandwidth may feature a better RF-to-DC efficiency instead of over a broad frequency band.

4. Adjustability: In some cases, MN is required to be adjusted for a variable load on the substrate (or PCB). An MN with lumped components has advantages regarding the adjustability since SMD components can be soldered on the substrate or can be easily removed from the substrate to tune out the MN whereas scaling Micro-strip line on the substrate is very difficult without degrading their electrical properties.

At that point, all the factors given above are crucial for the design of an MN for the RF circuits, but in some cases, one design factor may be more considerable than another. For example, reducing the complexity and correspondingly the losses due to the MN is the primary concern for the scope of this thesis. Because of the losses due to the Schottky-diode as explained in the previous chapter mostly inherent and cannot be alleviated with an MN, reducing both the MN losses and complexity of the design is required for the sake of the energy harvester efficiency.

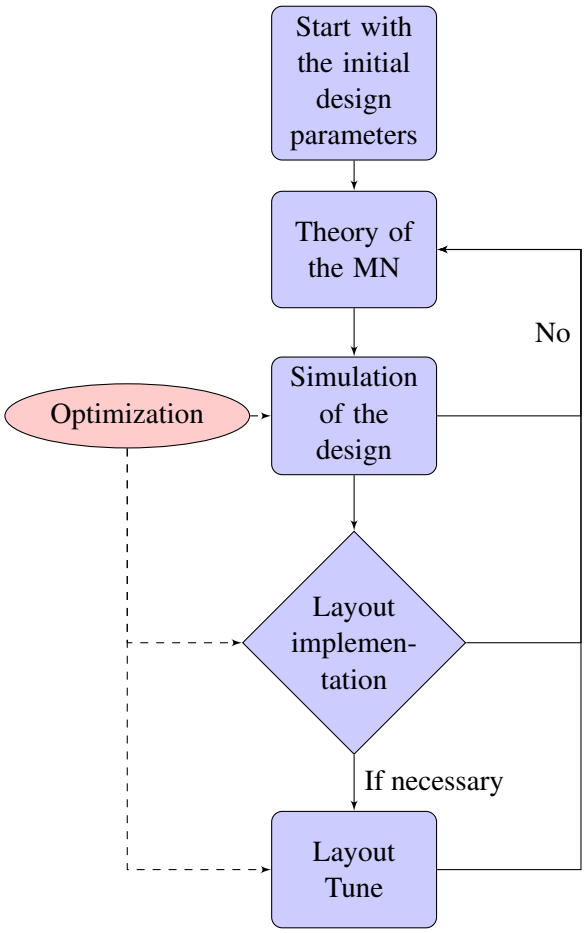

Figure 5.4: Illustration of the design flow in the scope of the MN realization.

5.3 Design Flow for the Impedance Matching Network with Rectifier Circuit

The steps to success in creating a practical and efficient rectifier circuit with MN on a substrate are shown in Figure 5.4. The systematic flow of the rectifier design with MN will be explained in shortly as includes:

1. Start: In the start step, it is worth to notice that the initial design parameters refer to the choice of the Schottky-diode, the RF input power level, the operation frequency, and the optimal load value for the voltage doubler circuit. As it is mentioned in Chapter 4, afore-mentioned initial design parameters profoundly affect the input impedance of the rectifying circuit; therefore, starting-up with those parameters is required to obtain a large signal input impedance of the rectifying circuit to decide an MN technique.

2. Theory: In this step, after the determination of the large signal input impedance of the rectifier circuit with the initial parameters, the corresponding input impedance(s) at the

desired frequency(ies) is/are placed on the Smith Chart to designate a workable MN for the rectifier circuit. It can be benefited from a theoretical approach to decide on the approximate value of the electrical parameters of the micro-strip lines and the discrete parts for both the simulation and the optimization steps. For example, if a tapered line will be utilized to get an input match at the frequency of interest, its both electrical and physical parameters such as width(s) or length can be approximated with the theory and then the theoretical values of the electrical parameters can be taken as a starting point for the simulation step, which will be very practical especially for the optimization step.

3. Simulation: Both the distributed and lumped (SMD) components of the MN and the rectifying circuit are first realized on the schematic and then simulated by means of the circuit simulator of the ADS from *Keysight Technologies*. However, the circuit simulation results are not efficacious in determining the surface current distribution on the micro-strip lines at the desired frequencies and also the radiation from the micro-strip lines. Therefore, Electromagnetic (EM) simulator of the ADS is utilized just for the distributed part, so as to get more accurate results from the RF/microwave physical parts such as micro-strip lines, vias, and ground plane further to take account the conductor and the substrate losses into the evaluation of the RF-to-DC conversion efficiency. Henceforth, the Co-simulation of the ADS enabling both distributed and the lumped parts to be simulated all together is utilized using the LSSP and HB simulators.

4. Layout implementation: LPKF ProtoMat Milling Machine is used to implement the RF/Microwave physical parts of the circuit on Rogers-4003C (PCB board). Murata SMD capacitors, SMD inductors, and SOT packages Schottky-diodes both of them from Farnell are exploited to realize the discrete parts of the rectifier circuit.

5. Layout Tune: After the implementation of the circuit on the substrate, sometimes since both SMD capacitors/inductors and Schottky-diode circuit models are not adequate in the level of simulations, the fine-tuning on the substrate is required to adjust the reflection coefficient (S_{11}) at the desired frequency band.

6. Optimization: Optimization is an essential part of the design flow starting from the simulation step. Optimization of each length & width of the micro-strip lines and, the value of SMD components has been carried out by means of ADS from *Keysight Technologies* by observing both the reflection coefficient and the RF-to-DC conversion efficiency.

In the following sections, first of all, the difference between conventional and the proposed MN will be given in order to obtain more insight. After that, the step-by-step design proce-

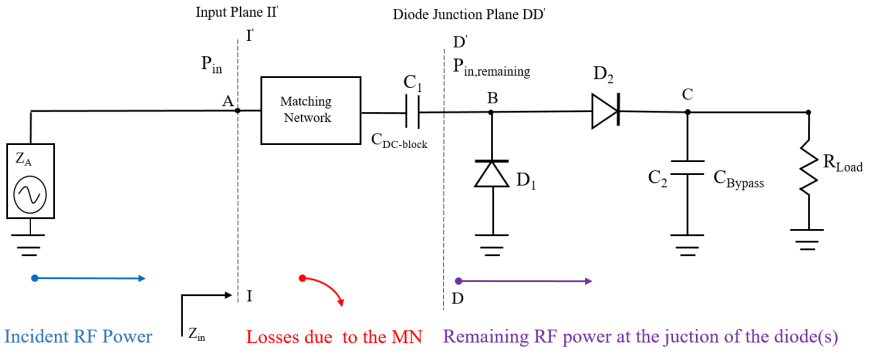

Figure 5.5: Voltage doubler with a conventional matching network.

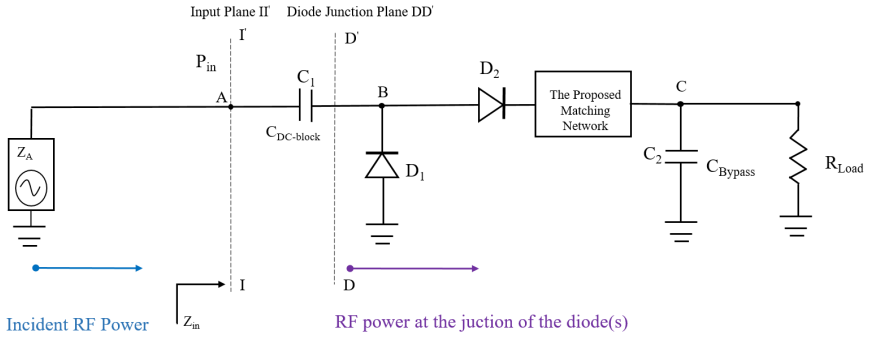

Figure 5.6: Voltage doubler with the proposed matching network.

dures for the proposed MN will be explored.

5.4 Difference Between the Conventional and the Proposed Matching Network

It is mentioned in the previous sections; MN losses become more substantial for the rectifying circuit considering the RF-to-DC conversion efficiency. A novel approach to get an input match at the desired frequency(ies) will be proposed aiming to decrease both the complexity of the MN and also the losses due to the MN.

As a starting point, the purpose of both conventional and the proposed matching networks is to obtain conjugate matching at between the input impedance of the antenna (50 Ω, practically) and the input impedance of the rectifier circuit to attain the maximum power. The difference between the conventional and the proposed matching network can be distinguished regarding the dissipation of an RF input power at point A, shown in Figure 5.5, passing through the MN part.

In a conventional way, attaining the maximum power at the II′ plane can be realized by

inserting an MN at between the antenna port and the rectifier circuit which ensures the input match between Z_{in} and Z_A so as to be Z_{in}=Z_A^* / R_{in}=R_A=50 Ω (practically) and X_{in}=−X_A where Z_{in} is the input impedance as seen by II′ plane whereas Z_A is the antenna input impedance. After reaching the conjugate matching condition, an RF power coming from the antenna, P_{in} appears as the available maximum RF power at the point A, which will be transferred to the load.

The available maximum RF power, P_{in} at the interference between the antenna and the rectifier circuit first passes through the impedance matching circuit (as shown in Figure 5.5), and then some of the RF power is lost in the MN hereafter, the remaining RF power, $P_{in,remaining}$ reaches the diode junction plane, DD′ (at the point B), again some part of the remaining RF power also is dissipated in the diode(s) and finally it is converted into the DC power. So, from the point of view of the RF power consumption, while the MN is aiming to ensure the maximum power transfer between the antenna and the rectifier, at the same time, it can be the source of the losses in the RF energy harvester. To overcome this dilemma, a novel approach has been proposed for the realization of the dual-band matching network.

In the same manner, the proposed MN also ensures the conjugate input impedance match between the antenna and the rectifier circuit so as to get Z_{in}=Z_A^* / R_{in}=R_A=50 Ω (practically) and X_{in}=−X_A. In the same way, P_{in} is the available maximum RF power at the II′ plane shown in Figure 5.6, which will be transferred to the load. The available maximum RF power at the interference between the antenna and the rectifier circuit first passes through the rectifier without exposing too many losses (refer to Figure 5.6). After that, it is first dissipated in the diode(s) and then converted into the DC power. At point between diode (D_2) and C, a certain level of the RF power at both fundamental and harmonics frequency besides DC power exist. The current (at certain level fundamental and harmonics) generated by the RF power at between point diode (D_2) and C by can be used to get an input match at seen by input plane. From the RF power consumption point of view, the proposed matching way, as opposed to conventional MN, aims to use the RF signals (harmonics of the fundamental) at the point between diode (D_2) and C to get a conjugate input match as seen by the II′ plane without substantially degrading the maximum available power at the point A.

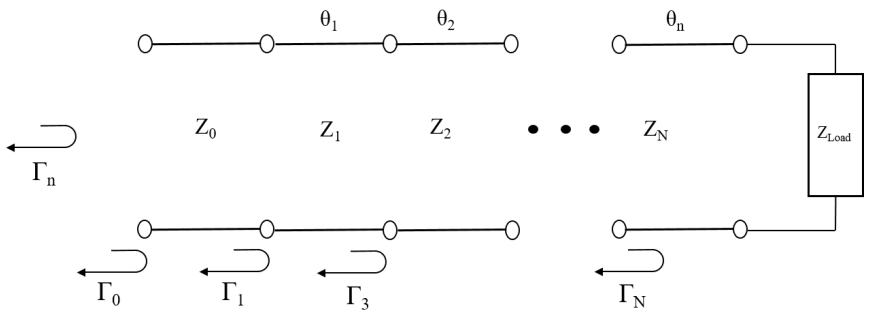

Figure 5.7: Partial reflection coefficients along a multi-section matching transformer.

5.5 A Novel Dual-Band Matching Network Design For Voltage Doubler Rectifying Circuit

5.5.1 Design Initials

As it is mentioned design flow section, initials for the proposed MN are firstly chosen as follows:

1) HSMS 2850 RF Schottky-diode having a low forward voltage value, V_f =150-250 mV is selected as a rectifying element.

2) The level of the input power is determined as -15 dBm, which is close to the diodes turn-on voltage and it is be considered as a moderately low power level in the scope of this work.

3) In order to obtain an input impedance at between 1.8 - 2.45 GHz, the lowest frequency of 1.8 GHz and the highest frequency of 2.45 GHz in the band of interest are selected as the operating frequencies, corresponding to the standards such as GSM-1800 and LAN/Wi-Fi, respectively.

4) In order to maximize the RF-to-DC efficiency, the load value is optimized by means of simulation at the desired frequencies of 1.8 GHz and 2.45 GHz, respectively, and it is found as $R_{load,optimized}$ = 1200 Ω. After the initial conditions are decided, the next step is the realization of the MN.

Before starting the design of the proposed MN, there are two important points that should be noticed;

1. The idea that the MN can be inserted different place rather than at between generator and the rectifier circuit to avoid the losses, is explained by *the theory of small reflection* [89].

In order to approximate the total reflection coefficient at the input plane, it is assumed that

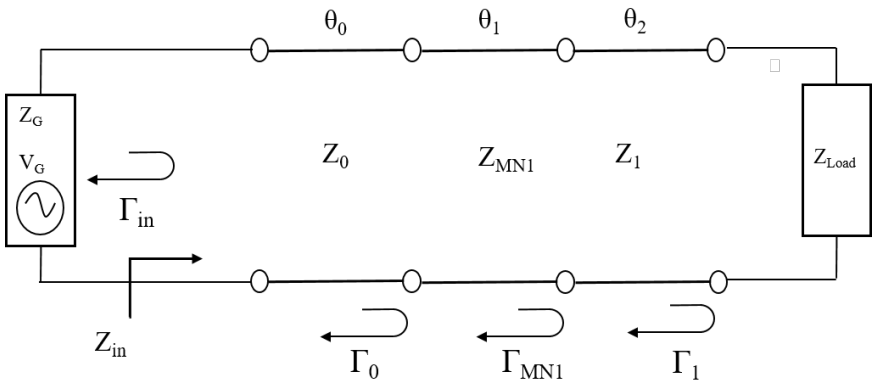

Figure 5.8: The first case; a matching network (MN1) is inserted at between Z_0 to Z_1.

the multi-section transformer shown in Figure 5.7, which consist of N number of transmission lines with equal length. By considering the approximation theory for multi-section quarter wave transformer [89], the partial reflection coefficient at the n^{th} junction can be expressed as follows:

$$\Gamma_n = \frac{Z_{n+1} - Z_n}{Z_{n+1} + Z_n} \tag{5.3}$$

All Z_n are assumed to decrease or increase monotonically across the multi-section transformer and Z_{load} is accepted having a real value. By using the (5.3) and the assumptions, the overall reflection coefficient can be approximately expressed as [71]:

$$\Gamma_n = \sum_{i=1}^{i=n} \Gamma_n e^{-2jn\theta_n} = \Gamma_0 + \Gamma_1 e^{-2j\theta_1} + \Gamma_2 e^{-2j2\theta_2} + ... + \Gamma_n e^{-2jn\theta_n} \tag{5.4}$$

where $\theta_1 = \theta_2 = ... = \theta_n = \theta$.

The conjugate matching condition, $Z_{in} = Z_G^*$ can be also expressed by considering the reflection coefficients corresponding to Z_{in} and Z_G^* as follows:

$$\Gamma_{in} = \Gamma_G^* \Longleftrightarrow Z_{in} = Z_G^* \tag{5.5}$$

By considering (5.3)-(5.5), two cases can be considered as shown in Figure. 5.8 and Figure 5.9. In the first case, the Z_{MN_1} section can be inserted at between generator (besides main line, Z_0) and Z_1, by using (5.4), the total reflection coefficient can be expressed as:

$$\Gamma_{in} = \Gamma_{Total} = \Gamma_0 + \Gamma_{MN_1} e^{-2j\theta_1} + \Gamma_1 e^{-2j2\theta_2} \tag{5.6}$$

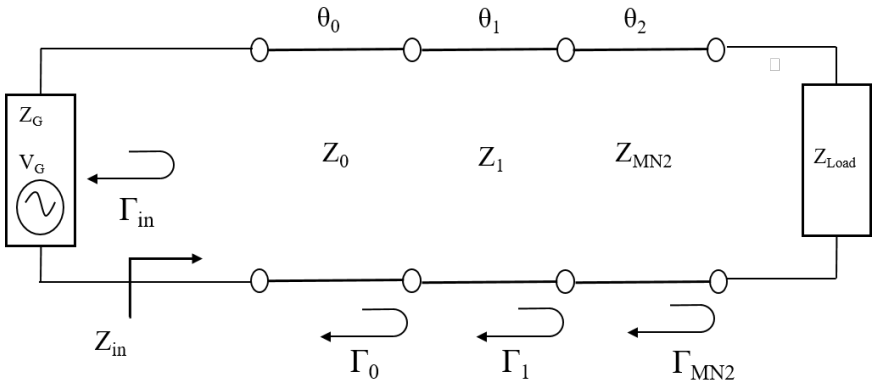

Figure 5.9: The second case; a matching network (MN2) is inserted at between Z_1 to Z_{load}.

where $\theta_1 = \theta_2 = ... = \theta_n = \theta$.

If a suitable Z_{MN_1} ensures the condition of Γ_{in}= Γ_G^*, the conjugate matching and hence the maximum power transfer can be achieved by inserting Z_{MN_1} having convenient electrical parameters.

In the second case, it is assumed that the Z_{MN_2} section is placed at between Z_1 and the load, in the same manner by using (5.4), the total reflection coefficient can be expressed as:

$$\Gamma_{in} = \Gamma_{Total} = \Gamma_0 + \Gamma_1 e^{-2j\theta_1} + \Gamma_{MN_2} e^{-2j2\theta_2} \tag{5.7}$$

where $\theta_1 = \theta_2 = ... = \theta_n = \theta$.

If a Z_{MN_2} with suitable electrical parameters ensures the condition of Γ_{in}= Γ_G^*, the conjugate matching and hence the maximum power transfer can be achieved along the transmission line by inserting Z_{MN_2} as it is shown in Figure. 5.9.

As a consequence of this, (5.6)- (5.7) theoretically prove that as long as an MN ensures conjugate matching at the input plane, the MN can be placed any convenient point in the circuit.

However, there are some restrictions determining in the place of the MN for the rectifying circuit. For example, if an MN is inserted at between capacitor, C_2 and R_{load} (refer to Figure 5.10), since the most of the RF signal at fundamental and harmonics (at a certain level) ideally passes through the C_2, only DC signal exists at between capacitor, C_2 and R_{load} so then it can be assumed that there is not enough RF signal to create surface current at the fundamental and harmonics to get an input match at the corresponding frequency(ies) of operation. Since the harmonics (besides at a certain level fundamental signal) created by both D_1 and D_2 are

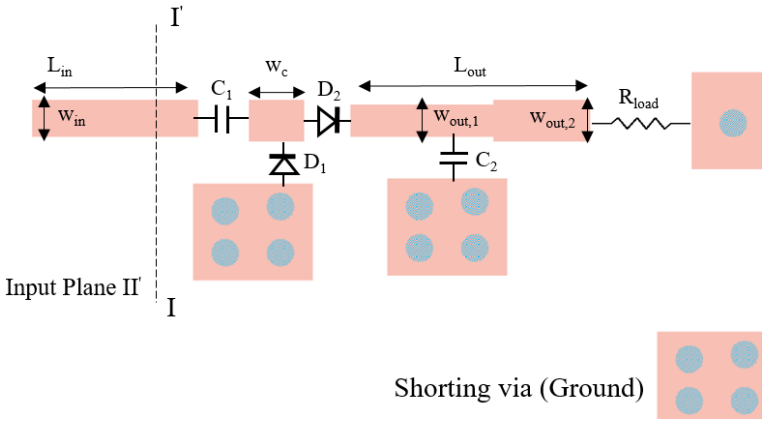

Figure 5.10: Initial rectifier circuit without matching network. w_{in}=1.6 mm, L_{in}= 7 mm, w_c = 1.8 mm, $w_{out,1}$ = 1.2 mm, $w_{out,2}$ = 1.8 mm, L_{out}= 8 mm, C_1= C_2= 47000 pF, D_1=D_2=HSMS 2850.

available at the point between diode, D_2 and C_2 therefore, the proposed MN is placed at that point in order to get input impedance at seen by input plane.

2. *As it is mentioned section 5.3,* as the SMD models of the lumped components are not adequate and further, a relative dielectric permittivity, (ϵ_r), of Roger4003C may change at the frequency band of interest, there are some differences between both EM-co simulation and practical implementation of the rectifier circuit in terms of both the resonance frequency and the reflection coefficient. As a result of the experiences from the MN design for the rectifier circuit for this thesis, it has been observed that the designed resonant frequencies shift towards the lower frequency side of the spectrum. Therefore, in order to obtain an input impedance match nearly GSM-1800, the design frequency offset has been taken in between 2–2.1 GHz and in the same manner, to get an input impedance match around Wi-Fi bands, the frequency offset has been taken in between 2.5–2.55 GHz.

5.5.2 Dual-Band Matching Network Design with a Novel Approach

As a first step, in order to determine the input impedances at 2–2.1 GHz and 2.5–2.55 GHz, the rectifier circuit (refer to Figure 5.10) without MN with the initial parameters is simulated by using EM-co simulators. The width and length of the input line are adjusted as approximately Z_0= 50 Ω and w_{in}= 1.8 and L_{in}= 7 mm to place SMA connector. The values of the w_c, $w_{out,1}$, $w_{out,2}$, L_{out} are selected as shown in Figure 5.10 to easily solder the corresponding components.

The large signal input impedances have been recorded as approximately $Z_{in}(f_1)$ =5-j*36

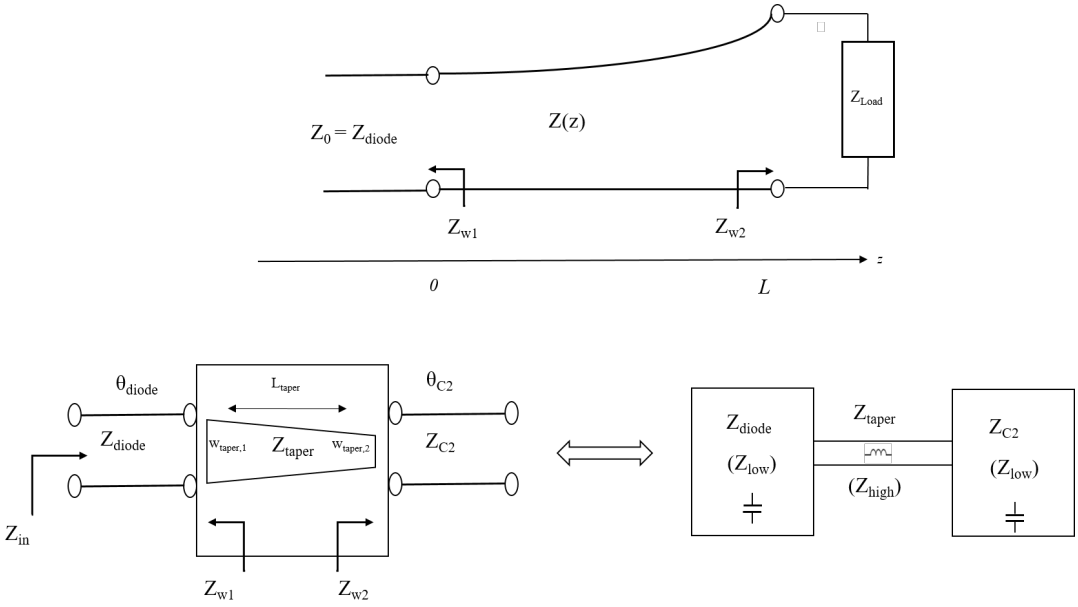

Figure 5.11: The equivalent of the tapered line.

– 4.7- j*32 Ω at between f_1=2-2.1 GHz and $Z_{in}(f_2)$= 4.52- j*18 – 4.5- j*16 Ω at between f_2=2.5-2.55 GHz. Besides, it can be seen that the location of both $Z_{in}(f_1)$ and $Z_{in}(f_2)$ on Smith Chart are not inside the area of R > 1 (R+j*X / (-j*X)) or G > 1 (G+j*B (/-j*B)) on both impedance and admittance Smith Chart.

First of all, it is questioned that what if multiple reflections are created along a single transmission, so then a single transmission line may result in the transformation of the input impedance of the rectifier circuit to the Z_0. The creation of the multiple reflections along the transmission line can be obtained by the implementation of the different discrete sections (refer to Figure. 5.7), as it is suggested in binomial multi-section matching transformer. Therefore, the tapered line is suggested which continuously tapers without a discontinuity along the length of the line [89].

1. The tapered line section design:

If both the Z_{diode} and Z_{C2} are approximated as equivalent transmission line, which is shown in Figure 5.11, it can be seen that both the impedance of Z_{w1} seen at the boundary of $w_{taper,1}$ and the impedance of Z_{w2} seen at the boundary of $w_{taper,2}$ side are highly capacitive.

Similarly to the stepped-impedance low pass filter design [71], by adding the tapered line at between two Z_{low} as shown in Figure 5.11, a resonance at the frequency of interest can be achieved. Hence, it is aimed that the tapered line acts as a Quasi-lumped element which

has the length of $\lambda/4 < L_{taper} < \lambda/8$ at f_2 and at $2f_2$. The physical length of the L_{taper} is calculated using LineCalc Tool of the ADS, and finally initial values for the first solution are approximately determined as 17.6 mm < L_{taper}< 8.6 mm at f_2, 8.8 mm < L_{taper} < 4.2 mm at $2f_2$.

To predict the tapered line reflection coefficient and the impedance of the line as a function of the line length different types of analysis are exploited such as exponential taper, triangular taper, and Klopfenstein Taper [71]. In the analysis of the proposed tapered line, exponential taper approximation is considered as given

$$Z(z) = Z_0 e^{az} \quad for \quad 0 < z < L \tag{5.8}$$

In the determination of the Z_{w1}, it is assumed that the Z_{w1} represents the impedance of at the left boundary (z=0) of the tapered line as shown in Figure 5.11. At that point to evaluate the Z_{w1}, the approximation is done assumed by using (5.8) and then $Z(0)$ is approximated as $Z(0)= Z_0\ e^0$ at z=0, our case is $Z(0)=Z_0=Z_{diode}$ as shown in Figure 5.11. So then, the Z_{w1} can be approximated at z=0 (the left boundary of the intersection between diode and the tapered line) as $Z_{w1} \cong Z(0)$ so then the $Z_{w1} \cong Z_{diode}$.

After this assumption, in order to approximate the width of the tapered line, the real part of the impedance of the diode, which is represented by the diode internal resistance of R_s= 25 Ω for the HSMS 2850 Schottky diode, is taken into account. As a next step, Z_{w1} is initially approximated at between 30 Ω < Z_{w1} < 25 Ω. And finally, the corresponding width values are calculated in LineCalc as 3.7 mm < Z_{w1} < 4.7 mm at f_2.

As it is assumed that the tapered line introduces an inductive reactance to cancel out the capacitive reactance, in order to increase inductive reactance at the side of $w_{taper,2}$, the width of the tapered line is chosen as $w_{taper,1} > w_{taper,2}$ so as to get smooth from capacitive to inductive reactance. In addition, it is aimed to bring the Z_{in} at the center of SC by using a single transmission line. As it is shown in Figure 5.11, the physical meaning of the Z_{high} is smaller width value and hence the physical width of $w_{taper,1}$ is initially selected as 1.6 < $w_{taper,1}$ < 1.2 mm at f_2.

In the next section, the parametric study of the tapered line will be given to understand the effects of the tapered line parameters on the Z_{in}.

1.a. The parametric study for the tapered line section:

As it is mentioned previously, the theoretical approach is used to approximate the initial values of the tapered line. Therefore the parametric study will be presented in order to under-

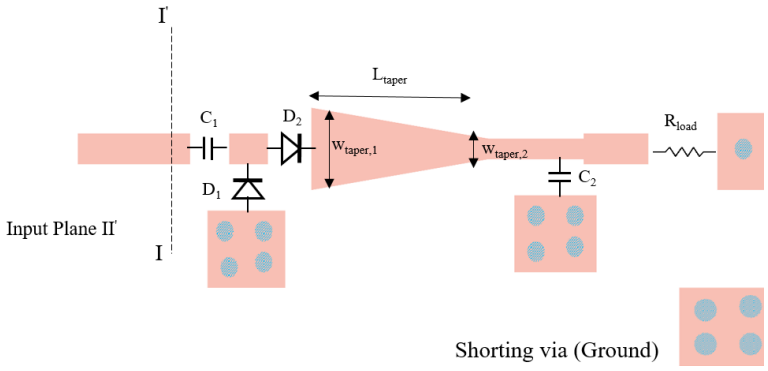

Figure 5.12: The layout of the proposed tapered line matching.

stand the effect of the dimensions of the tapered line on both the reflection coefficient and the Z_{in}. The key parameters, which highly affect the Z_{in} in the frequency range of f_2=2.5–2.55 GHz, are $w_{taper,1}$, $w_{taper,2}$ and, L_{taper}, respectively.

It is worth to notice that in the parametric study section since the Em-co simulation features more realistic results especially for the distributed part of the circuit (refer to Figure 5.12), the corresponding parameters are assigned in the EM layout, and parametric study of each value is carried out by means of Em-co simulation. Mesh density is chosen as 80 Cell/Wavelength for the proposed rectifier simulation with the key parameters. Moreover, the observation of the effect of the parameters is realized by changing one parameter value while the value of other parameters is kept constant.

As it is depicted Figure 5.13, the physical length of the tapered line, L_{taper} is selected as a first parameter to be investigated at the same time the values of $w_{taper,1}$=4.2 mm and $w_{taper,2}$=1.2 mm are kept as given. It is observed that when the tapered line length increases the resonant frequency shifts towards the lower side of the frequency spectrum. On the other hand, when L_{taper} decreases the resonant frequency shifts towards the upper side of the frequency desired frequency range. When the value of L_{taper} is altered at between 9.6-13.6, the capacitive and inductive characteristic of the tapered line changes differently resulting in different resonance frequencies having alternative S_{11}. However, in order to get the input impedance at the desired frequency range (f_2=2.5–2.55 GHz) the most suitable value for the physical length of the tapered line is initially determined as 11.6 mm < L_{taper} < 11.2 mm.

Furthermore, the value of the $w_{taper,1}$ is swept at between 1.2-6 mm while the value of $w_{taper,2}$=1.2 mm and L_{taper}=11.6 mm. Figure 5.14 indicates that how the reflection coefficient S_{11} changes as a function of $w_{taper,1}$. It can be seen from the result when $w_{taper,1}$ increases,

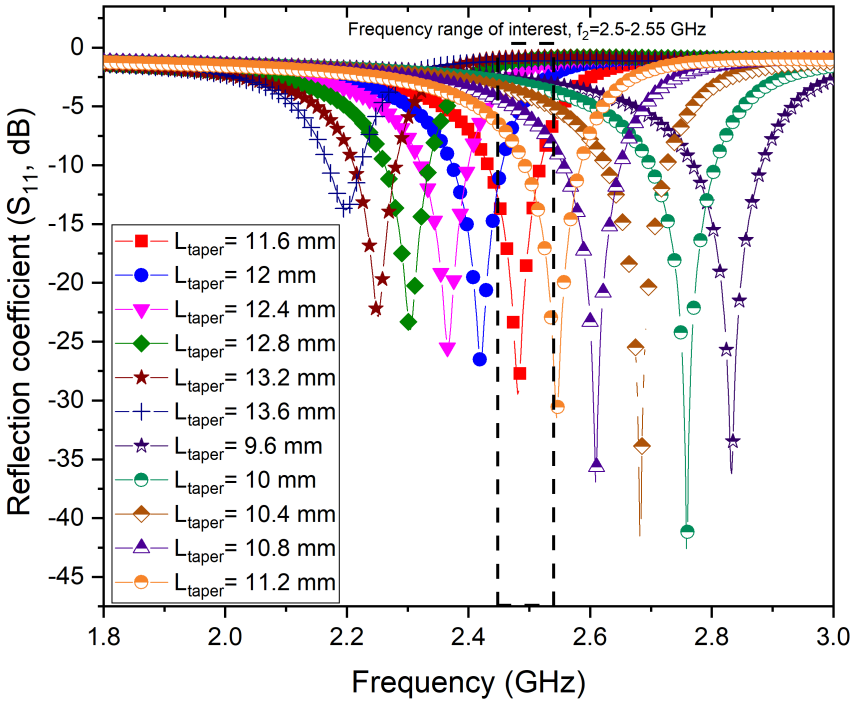

Figure 5.13: Simulated (EM-co) magnitude of the reflection coefficient of the proposed rectifier when L_{taper} is swept at P_{in}=-15 dBm and R_{load}=1200 Ω when w_2=1.2 mm and w_1=4.2 mm.

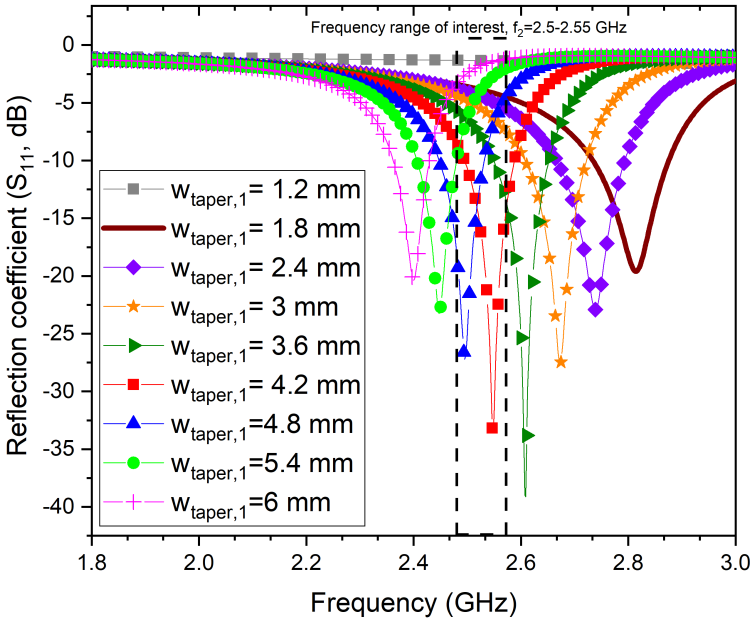

Figure 5.14: Simulated (EM-co) magnitude of the reflection coefficient of the proposed rectifier when $w_{taper,1}$ is swept at P_{in}=-15 dBm and R_{load}=1200 Ω when $w_{taper,2}$=1.2 mm and L_{taper}=11.6 mm.

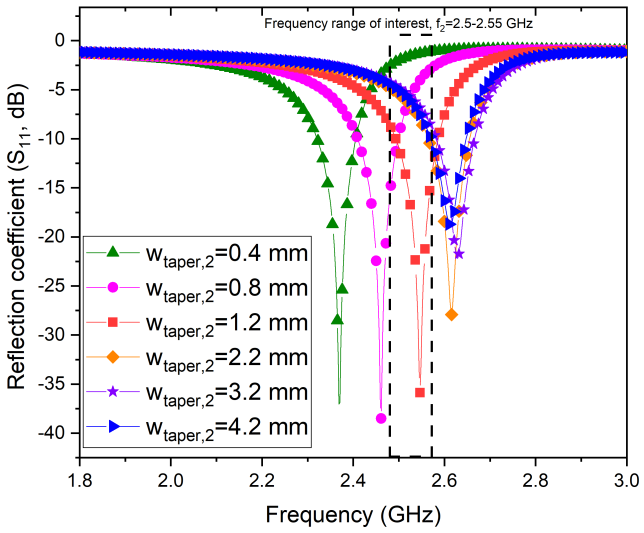

(a)

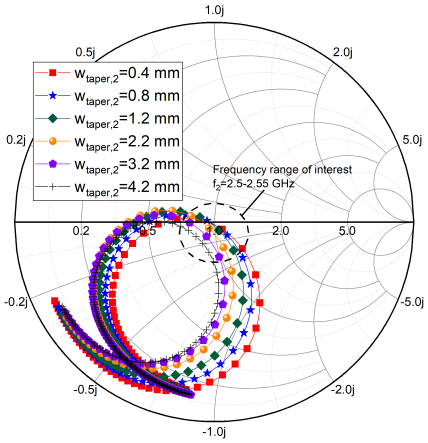

(b)

Figure 5.15: Simulated (EM-co) (a) magnitude of the reflection coefficient of the proposed rectifier (b) Smith Chart result when $w_{taper,2}$ is swept at P_{in}=-15 dBm and R_{load}=1200 Ω when $w_{taper,1}$=4.2 mm and L_{taper}=11.6 mm.

the resonant frequency slightly shifts towards to lower frequency side whereas when the value of $w_{taper,1}$ is kept to decrease, the resonant frequency goes to the upper frequency side. There is an interesting observation from the simulations when the value of $w_{taper,1}$= $w_{taper,2}$=1.2 mm there is no obtained resonance in which S_{11} is less than -4 dBm at between 1.8-3 GHz. Therefore in order to get a resonance at the frequency range of interest (2.5–2.55 GHz), the value of $w_{taper,1}$ should be bigger than the value of the $w_{taper,2}$.

As a result of the parametric study for $w_{taper,1}$, even the value of $w_{taper,1}$ = 3.2 mm features the best S_{11} and Z_{in}, since the obtained resonance is out of the frequency range of interest (refer to Figure 5.14), the most suitable values for the $w_{taper,1}$ to get the input match at the desired frequency range are recorded as 4.8 mm < $w_{taper,1}$ < 4 mm.

In addition, the effect of the $w_{taper,2}$ is investigated in the range of 0.4–4.2 mm when the values of $w_{taper,1}$=4.2 mm and L_{taper}=11.6 mm. On the contrary to the $w_{taper,1}$, it can be seen in Figure 5.15, when $w_{taper,2}$ decreases, the resonant frequency rapidly shifts towards to lower frequency side. When the value of $w_{taper,2}$ increases, in the first place the resonance frequency slightly goes to the upper frequency side; however, if the value of $w_{taper,2}$ is kept to increase, the reflection coefficient (S_{11}) starts to decrease at around the same frequency band.

The parameter study for both $w_{taper,1}$ and $w_{taper,2}$ verifies the assumption made in the theoretical part which states that to get a smooth transition between capacitive to inductive the value of the widths should be selected as $w_{taper,1} > w_{taper,2}$. Therefore, the values of the $w_{taper,1}$ and $w_{taper,2}$ are selected as $w_{taper,1} > w_{taper,2}$.

At the end of the parametric study of the tapered line, the initial approximation done in the theoretical section is verified and then the variables are initially selected as L_{taper}=11.6 mm, $w_{taper,1}$=1.2 mm, and $w_{taper,2}$=4.2 mm, which provide a good input impedance match at the frequency range of interest. After inserting the tapered line, the input impedance is recorded as Z_{in}= 49-j*2 Ω at f_2=2.547 GHz, besides the simulated magnitude of the reflection coefficient is obtained as S_{11}= -33 dB.

The creation of the first input match at between f_2= 2.5-2.55 GHz is achieved by just employing the tapered line (refer to Figure 5.12), and then the assumption of MN can be inserted any place in the circuit is verified. The next step is the creation of the second input impedance match at between f_1= 2-2.1 GHz.

2. Single stub section design:

After adding the tapered line, $Z_{in}(f_1)_{before,taper}$ =5-j*36 – 4.7- j*32 Ω (in EM-co simu) is transformed to $Z_{in}(f_1)_{after,taper}$ =6.4-j*32.5 – 7- j*28.5 Ω at between f_1=2-2.1 GHz. In order

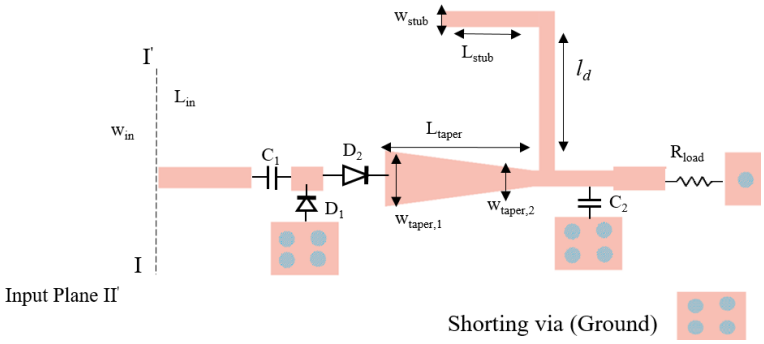

Figure 5.16: The layout of the proposed MN after adding the stub line.

to transform $Z_{in}(f_1)_{after,taper}$ to Z_0, a single shunt stub tunning (open-circuited) is suggested and placed as shown in Figure 5.16.

For a single shunt stub, there are two main parameters such as L_{stub} and l_d, which are the length of the stub and the distance from the load to the stub position, respectively. The given parameters can be analytically derived as given [71]

$$Z = Z_0 \frac{(R_L + j * X_L) + j * Z_0 \tan(\beta l_d)}{Z_0 + j * (R_L + j * X_L) \tan(\beta l_d)} \tag{5.9}$$

The admittance corresponding to the (5.9)

$$Y = G + j * B = \frac{1}{Z} \tag{5.10}$$

where the G and B represents the conductance and susceptance, respectively. To find the values of the corresponding G and B, the formula can be written in terms of l_d as given

$$G = \frac{R_L(1 + (\tan\beta l_d)^2)}{R_L^2 + ((X_L + Z_0 \tan\beta l_d)^2)} \tag{5.11}$$

$$B = \frac{R_L^2 \tan\beta l_d - (Z_0 - X_L \tan\beta l_d)(X_L + Z_0 \tan\beta l_d)}{Z_0[R_L^2 + (X_L + Z_0 \tan\beta l_d)^2]} \tag{5.12}$$

l_d is selected so as to get $G{=}Y_0{=}1/Z_0$. From (5.10), this results in a quadratic equation for $\tan\beta l_d$ written as (to simplify the quadratic equation, k=$\tan\beta l_d$)

$$Z_0(R_L - Z_0)k^2 - 2X_L Z_0 k + (R_L Z_0 - R_L^2 - X_L^2) = 0 \tag{5.13}$$

extracting k term from the (5.12)

$$k = \tan\beta l_d = \frac{X_L \pm \sqrt{R_L[(Z_0 - R_L)^2 + X_L^2]/Z_0}}{R_L - Z_0} \quad \text{for } R_L \neq Z_0 \tag{5.14}$$

(5.13) results in two principal solutions for l_d

$$\frac{l_d}{\lambda} = \begin{cases} \dfrac{1}{2\pi}\tan^{-1} k & k \geq 0 \\ \dfrac{1}{2\pi}(\pi + \tan^{-1} k) & k < 0 \end{cases} \tag{5.15}$$

To obtain the required stub lengths, L_{stub}, firstly the susceptance B_s=$-B$ is found by using (5.12), and then for an open-circuited stub L_{stub} can be expressed as

$$\frac{L_{stub}}{\lambda} = \frac{1}{2\pi}\tan^{-1}(\frac{B_s}{Y_0}) = -\frac{1}{2\pi}\tan^{-1}(\frac{B}{Y_0}) \tag{5.16}$$

By using analytical solution for a open-circuited single stub, the electrical lengths of both L_{stub} and l_d are calculated as given:

First solution: Electrical length for the l_d is θ_{l_d1} found as $6.32^o < \theta_{l_d1} < 18.72^o$, whereas electrical length for L_{stub} is found $\theta_{L_{stub1}} \cong 23.7^o$ for the range of f_1. Their physical values are calculated by using LineCalc Tool of the ADS, and finally the initial values for the first solution are determined as 2.158 mm $< l_{d1} <$ 4.4 6 mm and 5.92 mm $< L_{stub1} <$ 5.38 mm.

Second solution: Electrical length for the l_d is θ_{l_d2} found as $56.6^o < \theta_{l_d2} < 60.12^o$, whereas electrical length for L_{stub} is found $\theta_{L_{stub2}} \cong 159.9^o$ for the range of f_1. Their physical values are calculated by using LineCalc Tool of the ADS, and finally the initial values for the first solution are determined as 12.8 mm $< l_d2 <$ 13.65 6mm and 36.31 mm $< L_{stub2} <$ 39.95 mm for the range of f_1. Furthermore, the width of the stub is chosen as 50 Ω, it is calculated with LineCalc Tool of the ADS and found as approximately w_{stub}= 1.8 mm.

As it is mentioned previously, the theoretical values are used as a starting point for the optimization step. On the other hand, if the stub is represented as an equivalent transmission line as shown in Figure 5.17. Equivalent transmission line of the stub having characteristic impedance of Z_{se} and electrical length of θ_{se} will change the input impedance of $Z_{in}(f_2)$ after adding the open-circuited stub, $Z_{in,after,stub}(f_2)$ can be expressed as

$$Z_{in}(f_2)_{after,stub} = Z_{se}\frac{Z_0 + j * Z_{se}tan\theta_{se}}{Z_{se}tan\theta_{se} + j * Z_0} \tag{5.17}$$

where $Z_{in,before,stub} \cong Z_0 \cong$ 49-j*2 Ω at f_2= 2.547 GHz.

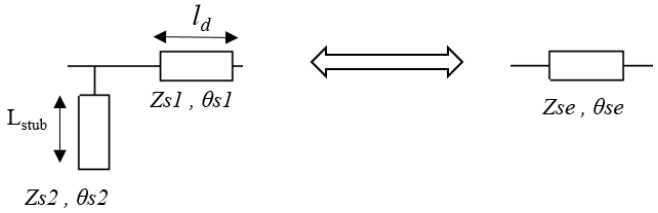

Figure 5.17: The equivalent of the proposed stub line.

As it can be seen from the (5.17), especially the length of the stub profoundly alters the $Z_{in}(f_2)$; therefore, as it will be given in the parametric study section, the only feasible physical length of the stub is taken into account. For example for the value of 36.31 mm < L_{stub2} < 39.95 mm in the range of f_1 is not feasible due to the fact that it highly alters the $Z_{in}(f_2)$ and also it increases the size of the MN. Hence, the suitable values for the stub parameters are taken initially into the account of the parametric study.

2.a. The parametric study for the single stub section:

The key parameters, which highly affect the Z_{in} in the frequency range of f_1=2–2.1 GHz, are L_{stub} and l_d. The observation of the parameters is realized by changing one parameter value while the values of other parameters are kept constant. For example, the tapered line parameters are kept in their initial values as $w_{taper,1}$=4.2 mm, $w_{taper,2}$=1.2 mm and, L_{taper}=11.6 mm. The only parameters that are changed for the sake of parameter study are L_{stub} and l_d.

As it is depicted Figure 5.18, the physical length of the stub, L_{stub} is selected as a first parameter to be investigated while the value of l_d=10.8 mm, and then L_{stub} is swept at between 10.4-3.4 mm. It is observed that when the stub line length (L_{stub}) increases the resonant frequency shifts towards the lower side of the frequency spectrum whereas L_{stub} decreases the resonant frequency shifts towards the upper side of the frequency desired frequency range. In addition to this, the input impedance at between f_2=2.5-2.55 GHz shifts toward the frequency range of 2.65-3 GHz after adding the stub and it relocates with the increment/decrement in L_{stub}.

Furthermore, the value of the l_d is swept at between 6.8-13.8 mm while the value of L_{stub}=7.4 mm. As a result of this, the resonant frequency changes as a function of l_d which is depicted in Figure 5.19. It can seen from the results when l_d increases, the resonance frequency shifts towards to the lower frequency side whereas when the value of l_d is kept to decrease, it goes to the upper frequency side. As it can be observed in Figure 5.19, the location of the second resonance still remains frequency band from 2.65-3 GHz.

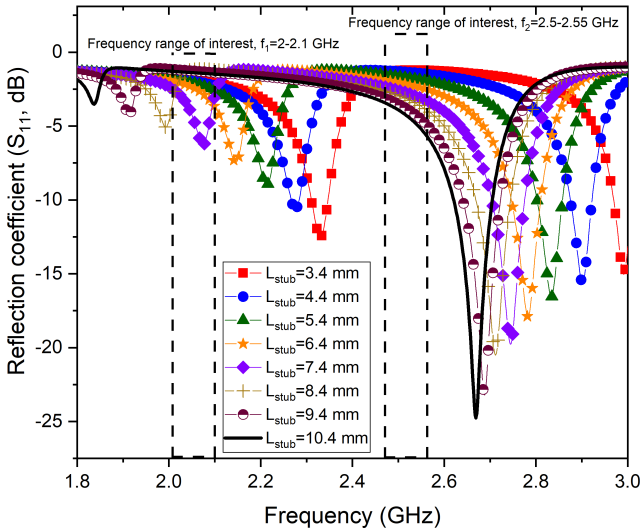

(a)

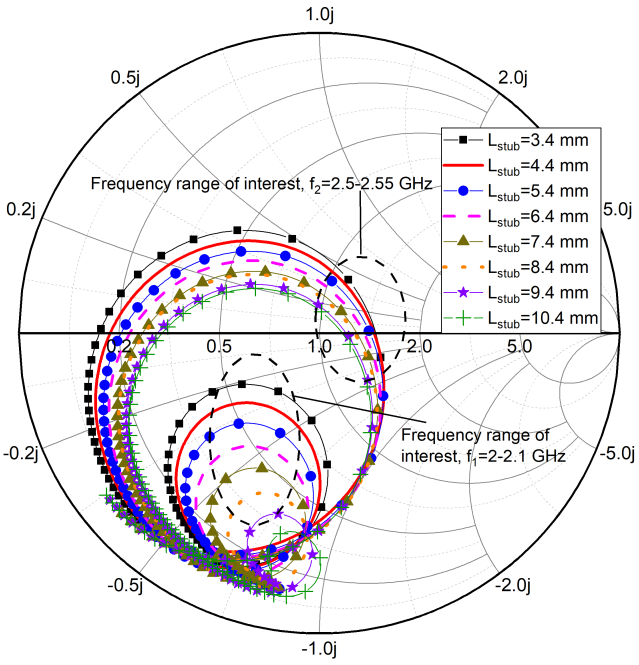

(b)

Figure 5.18: Simulated (EM-co) (a) magnitude of the reflection coefficient of the proposed rectifier (b) Smith Chart result when when L_{stub} is swept at P_{in}=-15 dBm and R_{load}=1200 Ω when l_d=10.8 mm, $w_{taper,1}$=4.2 mm, $w_{taper,2}$=1.2 mm and, L_{taper}=11.6 mm.

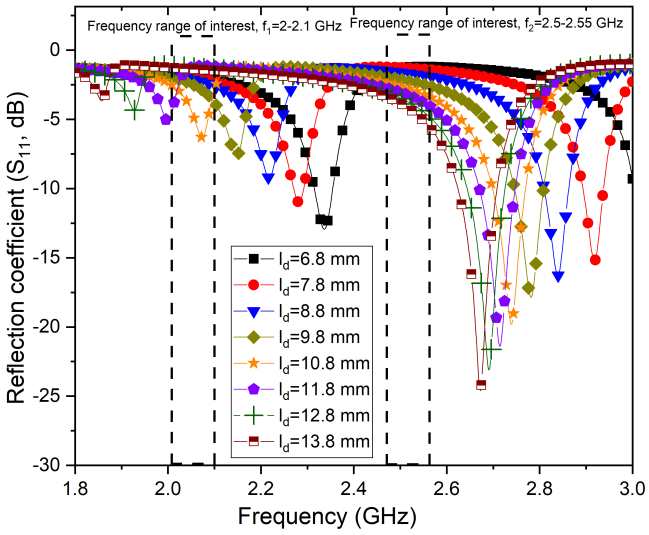

(a)

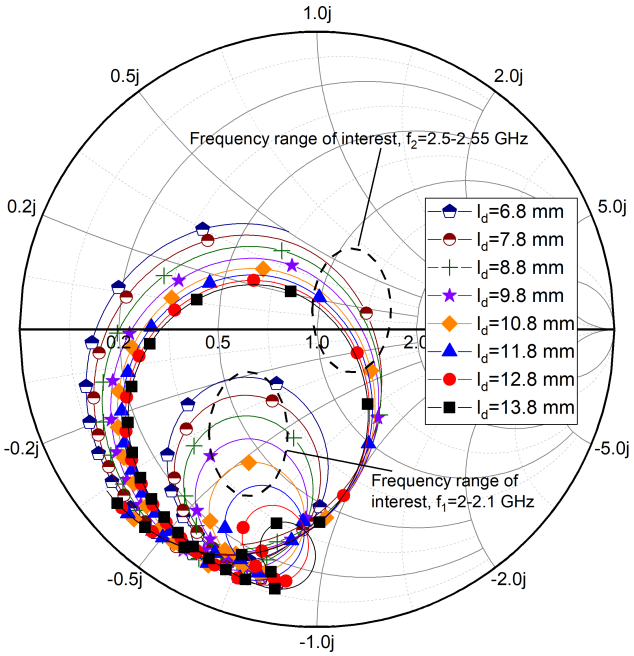

(b)

Figure 5.19: Simulated (EM-co) (a) magnitude of the reflection coefficient of the proposed rectifier (b) Smith Chart result when when l_d is swept at P_{in}=-15 dBm and R_{load}=1200 Ω when L_{stub}=7.4 mm, $w_{taper,1}$=4.2 mm, $w_{taper,2}$=1.2 mm and, L_{taper}=11.6 mm.

As a result of the parametric study of the stub section, since the theoretical values of the stub parameter profoundly shifted the first resonant at f_2=2.5–2.55 GHz, the approximated values for the open-circuited (shunt) stub parameters, which are derived from the analytical solution, could not be taken. Therefore, the transformation of Z_{in} at between $f_1 = 2-2.1$ GHz to Z_0 has not achieved by adding a single (shunt/open) stub. However, the stub section has brought the $Z_{in}(f_1)$ very closely to the 1-j*B circle on admittance Smith Chart at the frequency range of 2.05-2.07 GHz (refer to Figure 5.19). Therefore, if the capacitive reactance of the input impedance is canceled out by adding an inductive reactance, the transformation of Z_{in} at $f_1 = 2-2.1$ GHz can be still achieved. Hence, as a next step, adding an inductance section is proposed.

3. Inductor section:

It is worth to notice that the primary intention to add an inductor section is to cancel out the capacitive reactance of $Z_{in}(f_1)$ as it is mentioned previously. As the rectifier circuit with MN can also be considered a series resonant circuit, the inductor section is intentionally inserted at between II′ plane to AA′ plane as shown in Figure 5.20 to form a resonance with High–Quality factor. The reason for this, the rectifier circuit with high loaded Q-factor may results in high RF signal amplitude at the resonance, and hence the greater RF signal can enhance the DC output voltage [95].

Loaded Quality (Q-)Factor

The Q–factor in the resonance circuit is a quantity that indicates how much energy is lost from the energy stored at the resonant, which is expressed as [71]

$$Q = \omega \frac{\text{average energy stored}}{\text{energy loss}} = \omega \frac{W_m + W_e}{P_{loss}} \tag{5.18}$$

The loaded Q_L can be defined as

$$\frac{1}{Q_L} = \frac{1}{Q_0} + \frac{1}{Q_e} \tag{5.19}$$

where Q_0 is the unloaded Q-factor and for the series resonant circuit is expressed as

$$Q_0 = \frac{\omega_0 L}{R} \tag{5.20}$$

where Q_e is the external Q-factor and for the series resonant circuit is expressed as

$$Q_e = \frac{\omega_0 L}{R_L} \tag{5.21}$$

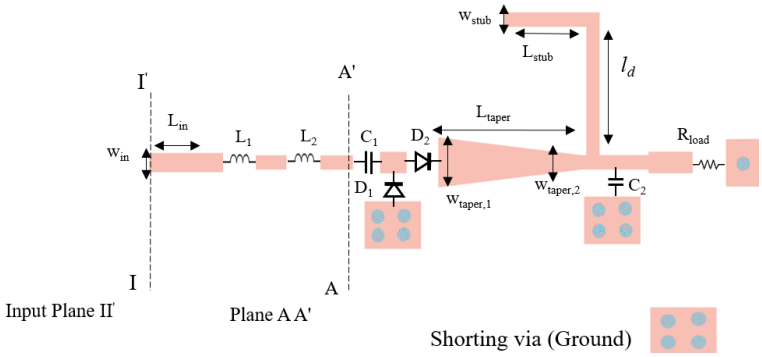

Figure 5.20: The layout of the proposed matching network after adding the inductor section.

Table 5.1: Optimized parameter values for the distributed part

Parameter	Value
$w_{taper,1}$	4.2 mm
$w_{taper,2}$	1.2 mm
L_{taper}	13 mm
w_{stub}	1.2 mm
L_{stub}	7.4 mm
l_d	10.8 mm

As it can be seen from (5.18)–(5.21) enhancement in the stored magnetic energy at the resonant can increase the Q_L results in greater RF signal amplitude. Therefore, it is assumed that if the inductor section is inserted at the input of the rectifier circuit (refer to 5.20), it can passively amplify the RF signal amplitude coming from the antenna and hence the RF-to-DC conversion efficiency can be boosted.

Finally, the optimization of all parameters for both the tapered line and stub section is repeated; firstly to bring the input impedance match in the range of f_2=2.5–2.55 GHz and secondly, to keep the $Z_{in}(f_1)$ very closely to 1-j*B circle on admittance Smith Chart in the range of $f_1 = 2 - 2.1$ GHz.

As a consequence of the parameter study, Table 5.1 indicates all the optimized parameters for the distributed part of the proposed MN. Furthermore, the values of the inductors have been selected to cancel out the capacitive part of $Z_{in}(f_1)$ so as to improve the S_{11} at f_1. Table 5.2 depicts all values for the discrete part in the simulation and the practical implementation. After all the parameters are tuned-out, the MN is simulated with the optimized values given in Table 5.1 and 5.2.

Figure 5.21 shows S_{11} of the proposed MN with and without inductor section. It can be

Table 5.2: Simulated and practical implementation values for the discrete part

Parameter	Simulated Value	Practical implementation Value
C_1	4700 pF	10 pF
C_2	4700 pF	6.8 pF
L_1	2.2 nH	1.5 nH
L_2	2.2 nH	1.5 nH

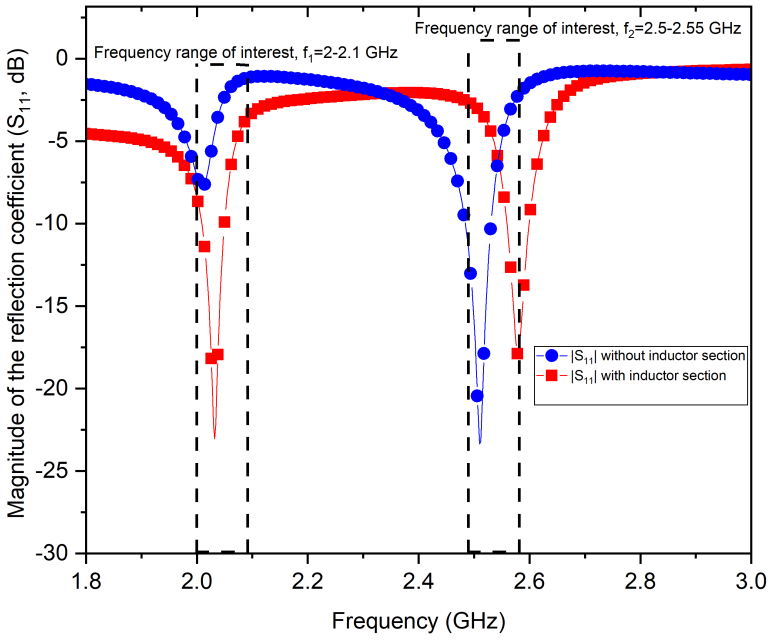

Figure 5.21: Simulated (EM-co) magnitude of the reflection before/after adding the inductor section.

seen from the results, after adding the inductor section, the input impedance at both the desired frequency of f_1 and f_2 is well-achieved.

Furthermore, as the Q-factor and the fractional bandwidth of the resonance circuit are inversely proportional to each other, the fractional bandwidth of the rectifier with and without inductor section are compared at the resonance. The bandwidth of the rectifier with and without inductor section is separately obtained from the simulation results in order to verify the assumption of which inductor section can enhance the Q- factor. Since S_{11} of the f_1 is above the -10 dB, the fractional bandwidth is evaluated as targeting the f_2. The fractional bandwidth of the rectifier without inductor section is taken for a target S_{11} = -10 dB, and then it is calculated as 1.83%. In the same manner, the fractional bandwidth of the rectifier with the inductor section is evaluated as 1.5%. The fractional bandwidth results indicate that the rectifier with inductor section features less fractional bandwidth at the resonance (f_2) and hence, it possesses greater Q-factor compared to the rectifier without the inductor section.

It is worthy of notice since there are some differences between the simulation and the practical implementation values of the discrete part of the proposed MN as shown Table 5.2, the parametric study for the discrete part will not be provided.

At the end, the rectifier circuit with the proposed MN is fabricated. Figure 5.22 depicts the latest Em-co layout and the fabricated prototype of the proposed MN with the optimized values given in Table 5.1 and 5.2. As a next step, the performance of the rectifier circuit in terms of S_{11} and RF-to-DC conversion efficiency will be discussed in the next section.

5.5.3 Performance Evaluation of the Rectifying Circuits with the Proposed Dual-Band Matching Network

5.5.3.1 Magnitude of the Reflection Coefficient Measurements

It is worth to notice that mesh density deliberately is chosen as 300 Cell/Wavelength in the final Em-co simulation of the rectifier with the optimized parameters (refer to Table 5.1 and 5.2). The measured and simulated reflection coefficient (S_{11}) of the rectifier circuit with the proposed MN are shown in Figure 5.23. The bands of interest involved in the design are enclosed with dashed line rectangles. The results have thoroughly matched with our frequency offset approach. The measured S_{11} of the rectifier circuit as a function of input RF power is also provided in Figure 5.24. As it can be seen, when the input RF power increased as 0 dBm, the S_{11} of the rectifier at the frequency range of interest still remains under -10 dBm.

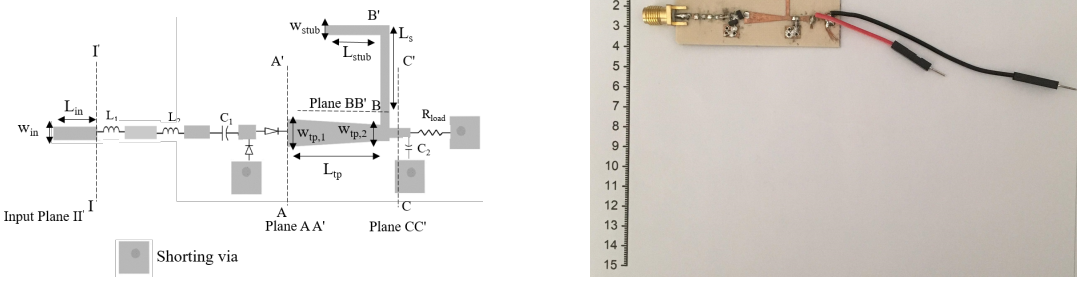

(a) (b)

Figure 5.22: (a) The layout of the rectifier with the proposed Matching Network (b) The fabricated prototype of the proposed rectifier.

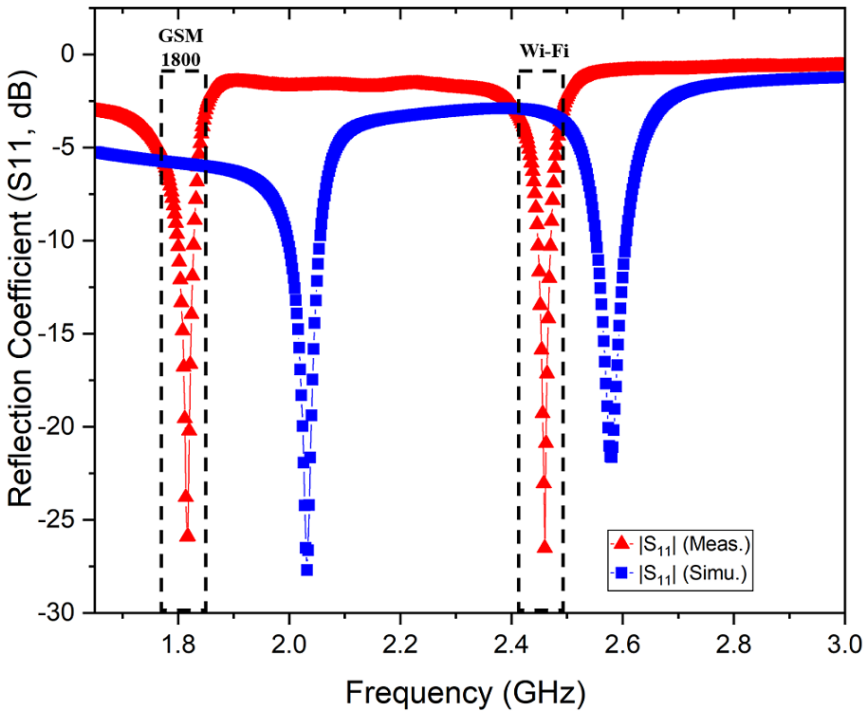

Figure 5.23: Measured and simulated (EM-co) magnitude of the reflection coefficient of the proposed rectifier at P_{in}=-15 dBm and R_{load}=1200 Ω.

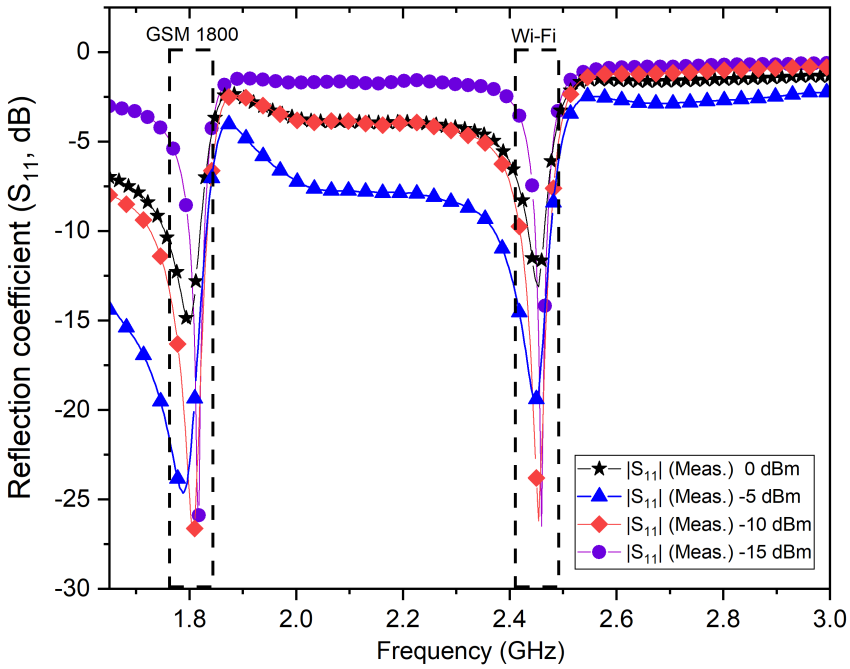

Figure 5.24: Measured reflection coefficient of the proposed rectifier as a function of RF power when R_{load}=1200 Ω.

5.5.3.2 RF-to-DC Conversion Efficiency Evaluation

The RF-to-DC conversion efficiency of the rectifier can be evaluated as follows:

$$\eta_{RF-DC} = P_{DC}/P_{RF} = V_{DC}^2/P_{RF}R_{Load} \tag{5.22}$$

where P_{DC} is the DC output power, P_{RF} is the RF power to the input of the rectifier, V_{DC} is the output DC voltage, R_{Load} is the value of load resistance.

By using (1), RF-to-DC conversion efficiency has been calculated at a single tone for both frequencies of 1.8 GHz and 2.45 GHz, respectively. Figure 5.25 reports the RF-to-DC conversion efficiency with respect to the input RF power. The measured RF-to-DC conversion efficiency of the dual-band rectifier is 46%, 56%, and 69%, for the different input power levels of -10, -5, 0 dBm, respectively at 1.8 GHz. On the other hand, it features efficiencies of 27%, 38%, and 48%, for the different input power levels of -10, -5, 0 dBm, respectively at 2.45 GHz. The peak conversion efficiency has been recorded as 72.2% at 4 dBm at 1.8 GHz and 53% at 7 dBm at 2.45 GHz.

The proposed rectifier performance in terms of the aggregated output DC voltage is depicted in Figure 5.26 and Figure 5.27. The measured output DC voltage of the dual-band rectifier is 0.25 V, 0.46 V, and 0.9 V, for the different input power levels of -10, -5, 0 dBm, respectively

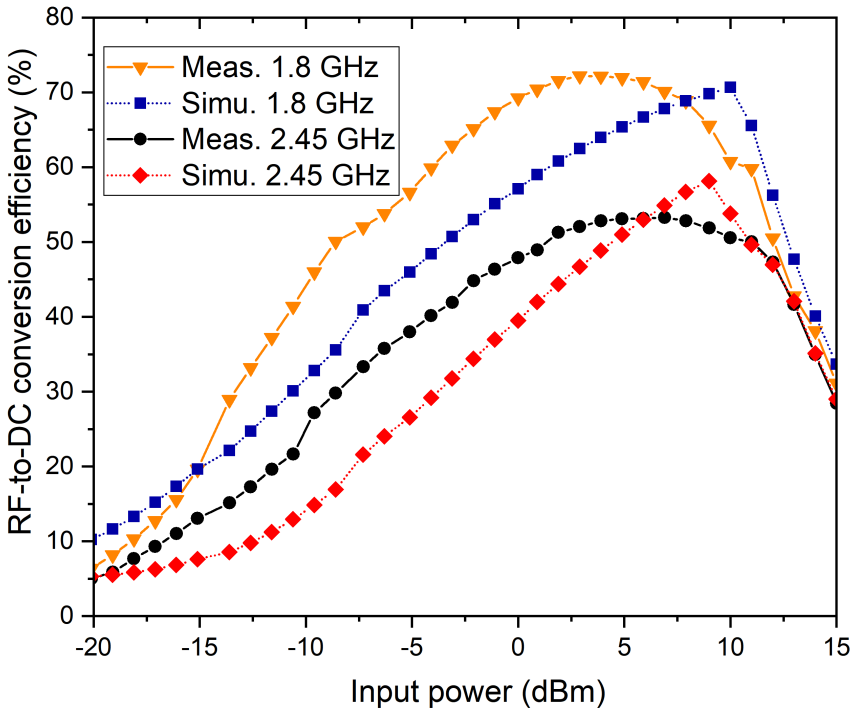

Figure 5.25: Measured and simulated RF-to-DC efficiency vs input power at 1.8 GHz and 2.45 GHz when R_{load}=1200 Ω.

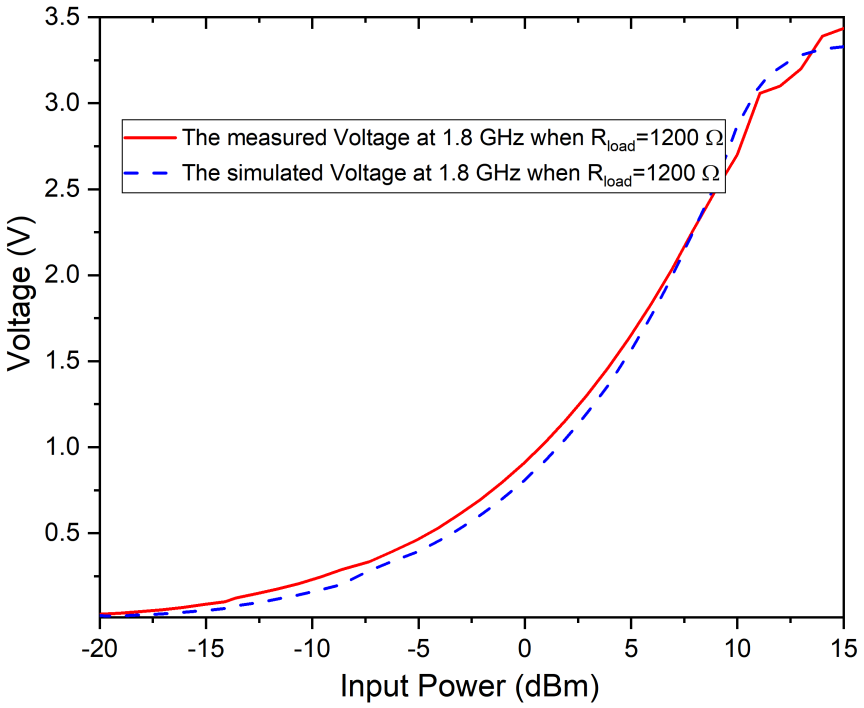

Figure 5.26: Measured and simulated output voltage vs input power at 1.8 GHz when R_{load}=1200 Ω.

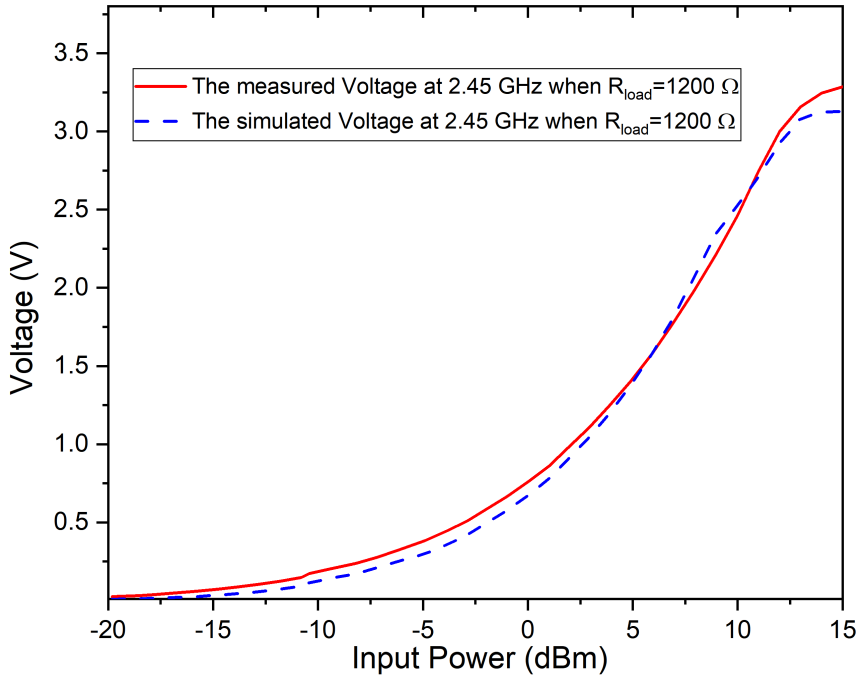

Figure 5.27: Measured and simulated output voltage vs input power at 2.45 GHz when R_{load}=1200 Ω.

at 1.8 GHz. On the other hand, it features output DC voltage of 0.17 V, 0.38 V, and 0.76 V, for the different input power levels of -10, -5, 0 dBm, respectively at 2.45 GHz. As it is depicted in Figure 5.25–5.27, the performance of the rectifier at 1.8 GHz is better than 2.45 GHz, this might be due to the diode and the substrate losses that increase with the frequency.

In order to demonstrate that the range of load resistance in which the rectifier features the maximum RF-to-DC conversion efficiency, the measured and simulated conversion efficiency as a function of the load resistance value at two frequency of interest are plotted in Figure 5.28 and Figure 5.29. It can be seen from both the measured and simulated results, the optimal load resistance value changes with the RF input power level. For example, the optimal load resistance value for the maximum RF-to-DC conversion efficiency changes at between R_{load}= 1800–3800 Ω when the input RF power is -15 dBm whereas, the maximum attainable RF-to-DC conversion efficiency alters at between R_{load}= 1000–2800 Ω for the RF input power range of -10 dBm to 0 dBm.

The variation of the optimal load value for the maximum RF-to-DC conversion efficiency is well expected because of the electrical properties of the Schottky diode such as video resistance. As it is explored in *Chapter 4*, video resistance profoundly changes with the RF input power levels and then it affects the optimal load value. Therefore, the different values

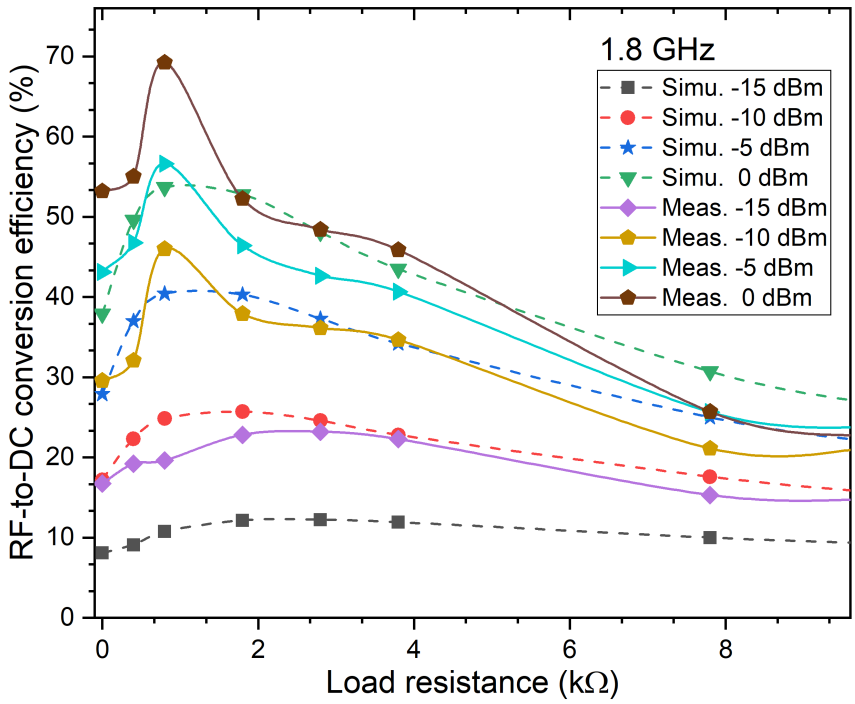

Figure 5.28: Simulated and measured RF-to-DC conversion efficiency of the proposed rectifier versus load resistance at f_1=1.8 GHz.

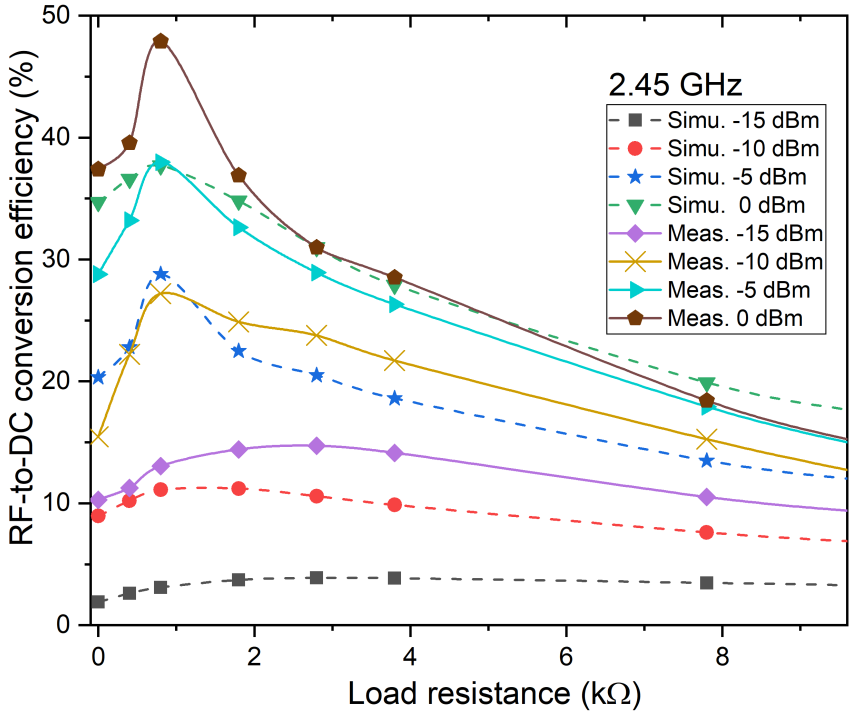

Figure 5.29: Simulated and measured RF-to-DC conversion efficiency of the proposed rectifier versus load resistance at f_2=2.45 GHz.

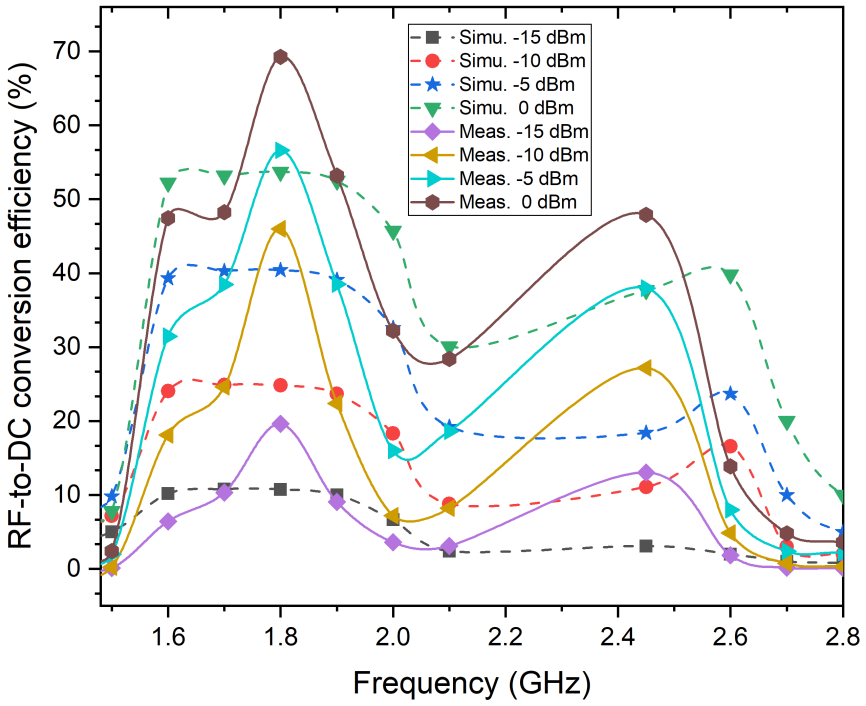

Figure 5.30: Simulated and measured RF-to-DC conversion efficiency of the proposed rectifier versus frequency when R_{load}=1200 Ω.

of the video resistance at the different RF power levels (bias levels) result in different optimal load resistance value for the maximum conversion efficiency. Additionally, it can be observed from the results, the optimal load resistance values at two frequencies of interest almost alter at between R_{load}= 1000–1800 Ω for the range of RF input power level of -10 dBm to 0 dBm.

The performance of the proposed rectifier with respect to the frequency is given in Figure 5.30. It should be noticed that RF-to-DC conversion efficiency reaches the maximum values of 16.57% and 23.7% at -10 dBm and -5 dBm, respectively at around 2.5-2.6 GHz in the simulation results whereas the measured conversion efficiency varies slightly at around 2.4–2.45 GHz with the maximum efficiencies of 27%, 38%. The difference between the simulation and the measured results in the frequency bands of 2.4–2.45 GHz and 2.5-2.6 GHz is due to the design frequency offset which is taken at around 2.5-2.6 GHz in the simulations. Therefore, the maximum attainable RF-to-DC conversion efficiency shifts towards the band of 2.5-2.6 GHz in simulation results.

Furthermore, the simulated RF-to-DC conversion efficiency is almost constant at the frequency band of 1.6-2 GHz at the different input power levels, however as it is seen from the measurements results, the RF-to-DC conversion efficiency is at the highest value at around

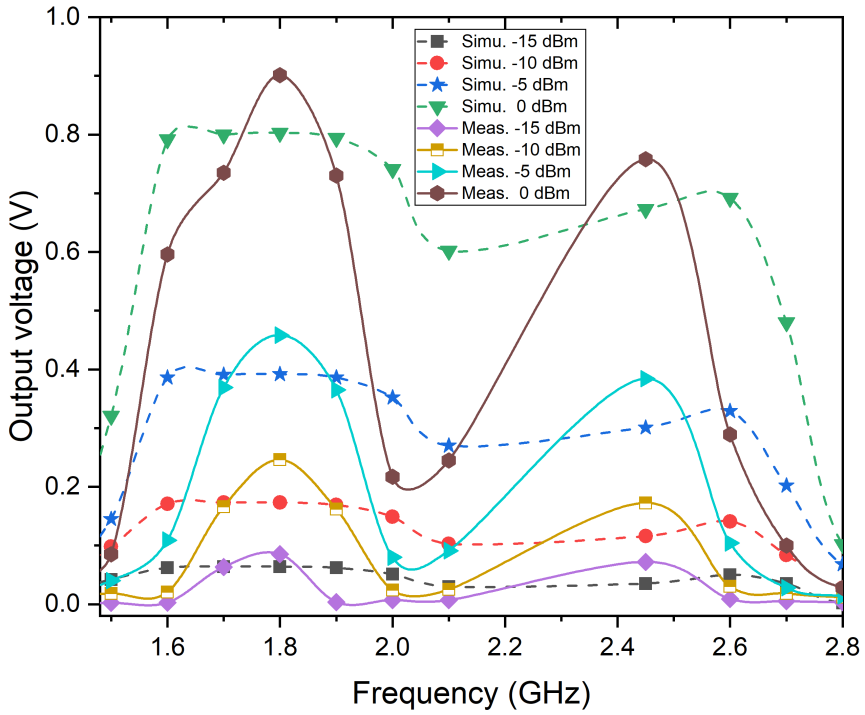

Figure 5.31: Simulated and measured output DC voltage for a single tone sweep of the proposed rectifier versus frequency when R_{load}=1200 Ω.

1.8-1.85 GHz and it decreases as the operation frequency goes to the frequency bands of 1.5–1.7 GHz and 1.9–2.2 GHz, respectively. The difference between the simulation and measurement results might be due to the fact that the response of the Schottky diode which is idealistically approximated in the simulation. Therefore, as the non-linear behavior of the diode varies comparatively over the frequency from 1.6 to 2 GHz in the simulation, it may result in slight changes in the RF-to-DC conversion efficiency as the frequency of operation changes. However, in the practical laboratory measurements, the response of the Schottky diode at the different operation frequency has been observed. According to the measurement results, the response of the Schottky diode alters considerably when the operation frequency changes. Furthermore, the performance of the proposed rectifier in terms of the DC output voltage as a function of frequency is plotted in Figure 5.31. It can be seen from both the simulated and the measured results, the trend of change in the DC output voltage is the same as the trend of change in the RF-to-DC conversion efficiency when the operation frequency alters.

CHAPTER 6

EXPERIMENTAL STUDIES OF RECTENNA

"I want to shatter all stereotypes. The dream is to continue combining physics and dance. "

- Merritt Moore , *The professional ballerina and quantum physicist*

6.1 Rectenna Measurements in a Controlled Environment

In order to evaluate the performance proposed rectenna in a controlled environment, an experiment in a laboratory is conducted using the setup shown in Figure 6.1. The proposed broadband fractal slotted antenna (R_x) is aligned with the transmitter antennas (T_x) in order to bring their phase centers at the same level as accurate as possible. At the transmitter side, same broadband fractal slotted antennas are used, and all the antennas are placed on foam.

It is noteworthy that in order to observe the power transmission at the far-field of the proposed broadband fractal slotted antenna, the T_x and the R_x have to be sufficiently separated from each other so that to get interaction between T_x and the R_x is only because of the radiated EM field. Otherwise, the reactive effects might be observed, and it can alter the power transmission. Therefore, the T_x and R_x should be located in the Fraunhofer region, which is determined by the well-known formula given as

$$R = \frac{2D^2}{\lambda_0} \tag{6.1}$$

where R indicates the distance between the phase center of the antennas, D is the largest dimension of the T_x antenna, and λ_0 is the wavelength of the operating frequency in free-space. So then, the distance between the T_x and R_x is selected as 33 cm.

The measurement steps are given as; 1) two power generators (Agilent E4428C and R&S

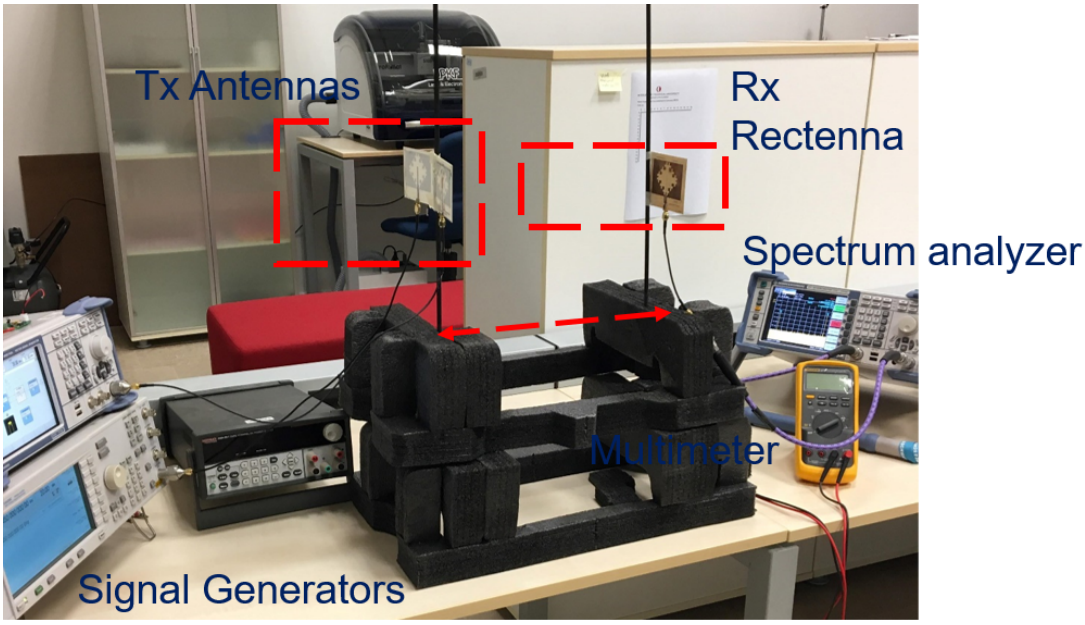

Figure 6.1: Experimental setup for the rectenna measurement in a controlled laboratory environment.

SMBV 100A), each incident power is swept at between 5-26 dBm, and are connected to transmitter antennas.

2) a spectrum analyzer (R&S 2VL) is used to measure the amount of the received power in dBm. The measured power as a function of frequency was recorded to obtain the received power in dBm at each frequency.

3) the total power density in W/m^2 is estimated with the well-known formula as follows:

$$P_{density,total} = \frac{4\pi}{c^2} \frac{\sum_{i=1}^{i=n} P_{fi}}{\sum_{i=1}^{i=n} \frac{G_{fi}}{F_i^2}} \tag{6.2}$$

where $P_{density,total}$ is the total power density, P_{fi} is the input power level as a function of frequency, G_{fi} is the gain of the receiving antenna at each frequency, c is the speed of the light and F_i is the corresponding frequency of 1.8 GHz and 2.45 GHz. Using (2), the total power density is calculated.

4) after finding the total power density, the proposed dual-band rectifier was connected to the proposed antenna without disturbing the alignment condition. Moreover, the open and loaded voltage values at the output terminals of the rectenna were measured using a multimeter (Fluke) and recorded.

Figure 6.2 indicates the measured RF-to-DC conversion efficiency of the rectenna and Figure 6.3 shows the DC output voltage with respect to the RF power density at the condition

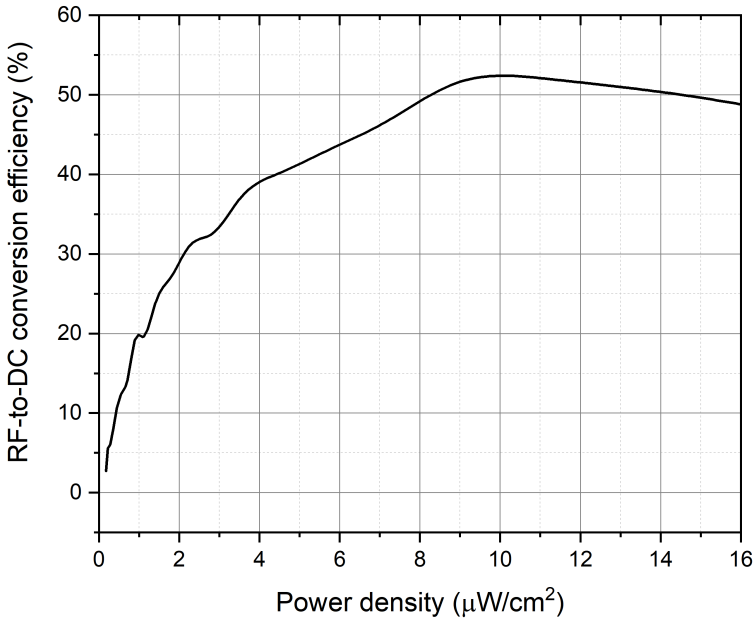

Figure 6.2: Measured RF-to-DC conversion efficiency as a function of the incident power for two frequencies of 1.8 & 2.45 GHz.

of two tone signal. As it can be seen from the results, rectenna features the highest RF-to-DC conversion efficiency of 51.9% when the total power density of two tone signal is 11.1 μW/cm^2.

In order to evaluate the energy harvesting capability of the rectenna with the dedicated RF source, the measurements conditions are kept the same as shown in Figure 6.1. Only a temperature sensor, which has a supply voltage value 1.5 V to operate and read the temperature, is connected at the output of the rectenna as shown in Figure 6.4. The proposed rectenna is able to actuate the low power temperature sensor when the total power density of at around 15 μW/cm^2 when the two-tone signal is available.

In order to investigate the energy harvesting capability of the proposed rectenna in a realistic scenario, microwaves oven which operates at the at the ISM S-band is selected as a dedicated source. RF spectrum measurement was conducted to determine the frequency bands and the available power density near to the microwave oven. First of all, portable measuring equipment for electromagnetic field (EMF) from Narda was placed at a distance of 50 cm from the microwave oven.

The instant screen image is obtained from the Narda. The measured frequency bands and the available power densities are shown in Figure 6.5. It is important to notice that, the available frequency bands and power densities were intermittently changing. For example,

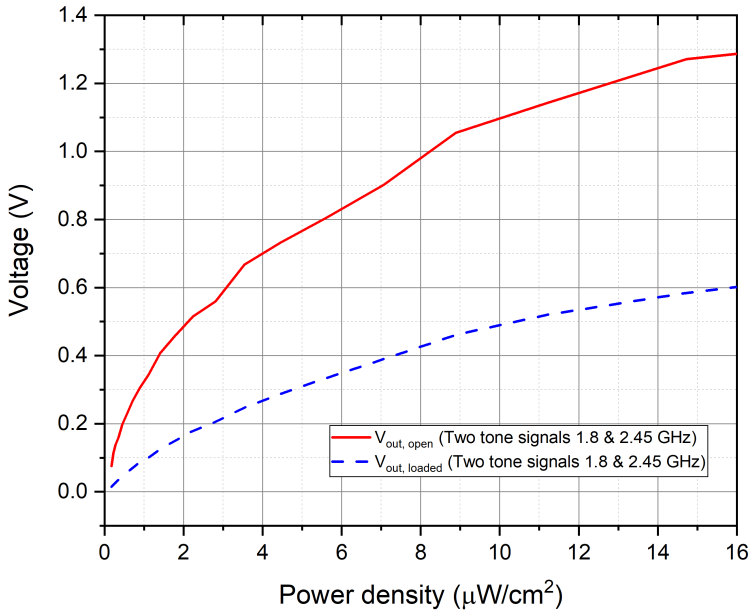

Figure 6.3: Measured DC output voltage as a function of the incident power for two frequencies of 1.8 & 2.45 GHz.

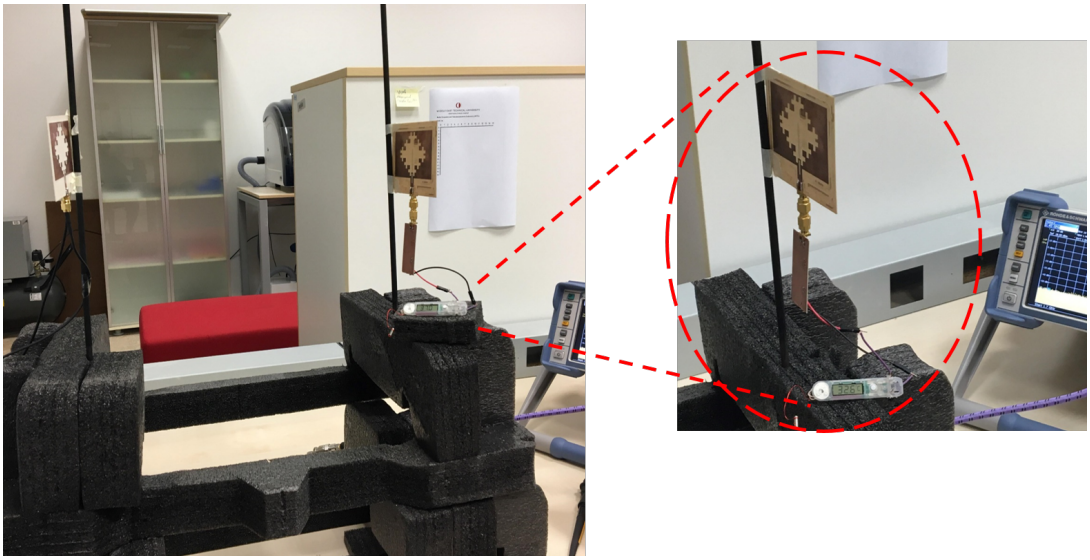

Figure 6.4: The proposed rectenna with the temperature sensor.

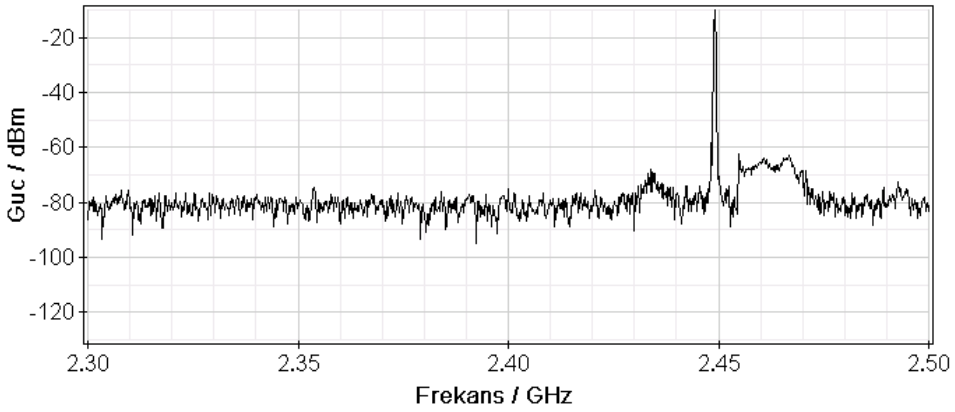

Figure 6.5: The instant available frequency bands and the power near to the microwave oven.

the frequency band was changing at between 2.4-2.48 GHz whereas the available power was altering at between -20 – -70 dBm. Under this condition, as it can be seen from the Figure 6.6 when the rectenna is placed closely (the distance of nearly 30 cm) to the microwave oven, it is able to actuate the temperature sensor.

6.2 Rectenna Measurements in Ambient

Harvesting RF energy from the ambient is more challenging and difficult due to the RF power levels in the environment are relatively low and unstable. Therefore, in order to determine the available frequency bands and then the RF power densities, a simple RF spectrum study and a field measurement to cover the standards of GSM-900, GSM-1800, DECT, 3G (UMTS), and WLAN are conducted in Middle East Technical University Northern Cyprus Campus (METU-NCC). The surveyed areas have been decided according to the mobile base station position which is near to the academic buildings as depicted in Figure 6.7. Field measurement device has been used in spectrum mode to obtain the available frequency bands and the corresponding power densities.

Figure 6.8-6.11 show the RF power distributions which are a function of frequency. Table 6.1 summarizes the total power densities and specifies the range of each frequency bands in which the available power is averaged. As seen from the results, it is recommended that RF energy harvesting from the standards of GSM-900 and 3G (UMTS) is more suitable in the METU-NCC.

Under the available frequency bands and the power densities condition, in order to evaluate the performance of the proposed rectenna in ambient, different locations in the campus

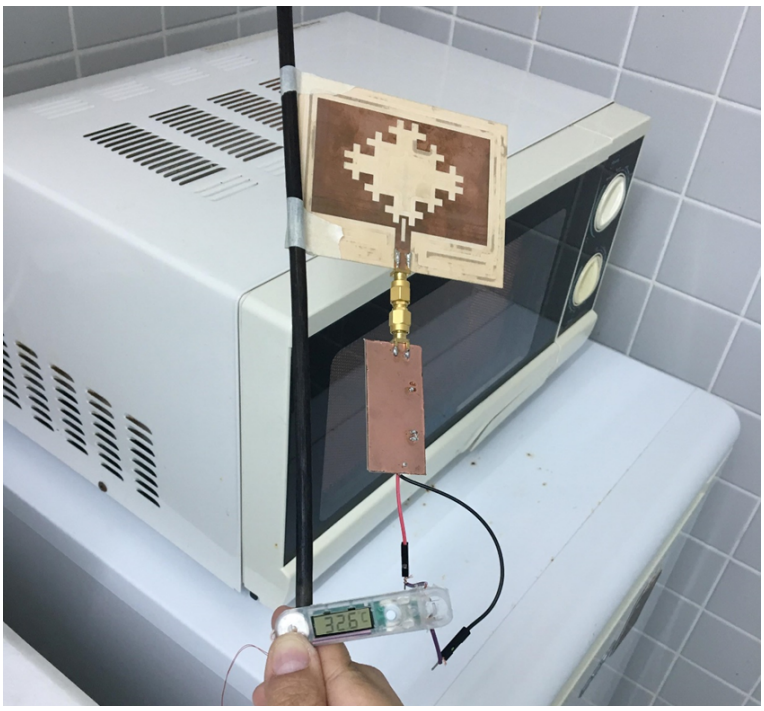

Figure 6.6: Possible practical scenario for the proposed rectenna: dedicated RF energy harvesting from microwave oven.

Figure 6.7: Measurement locations in METU-NCC.

Table 6.1: Measured ambient electric field densities from different standards

Standard	Frequency Range (MHz)	Total Value (V/m)
GSM-900	890-960	4.137
GSM- 1800	1710-1876	0.026
DECT	1881-1900	0.008
3G (UMTS)	1920-2170	1.818
WLAN	2400-2483	0.021

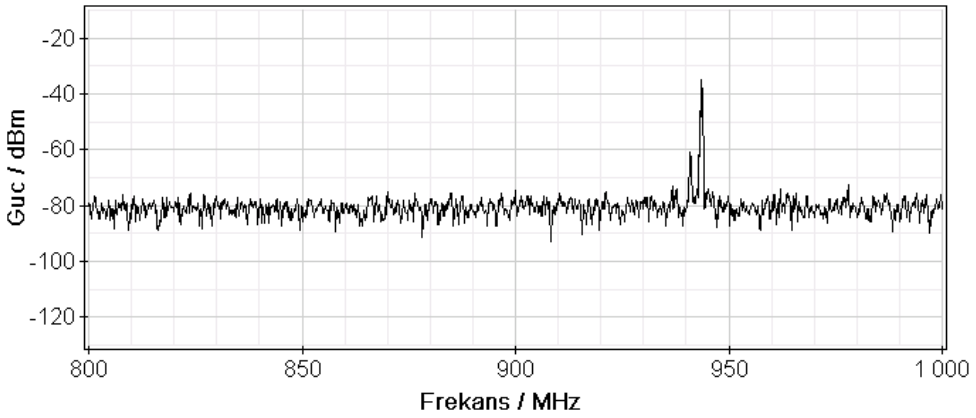

Figure 6.8: Measured received power reading from the spectrum analyzer for GSM-900.

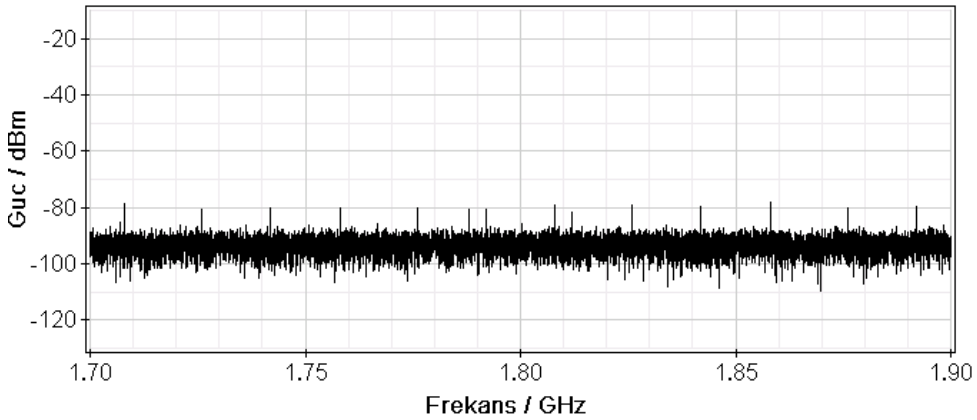

Figure 6.9: Measured received power reading from the spectrum analyzer for GSM- 1800.

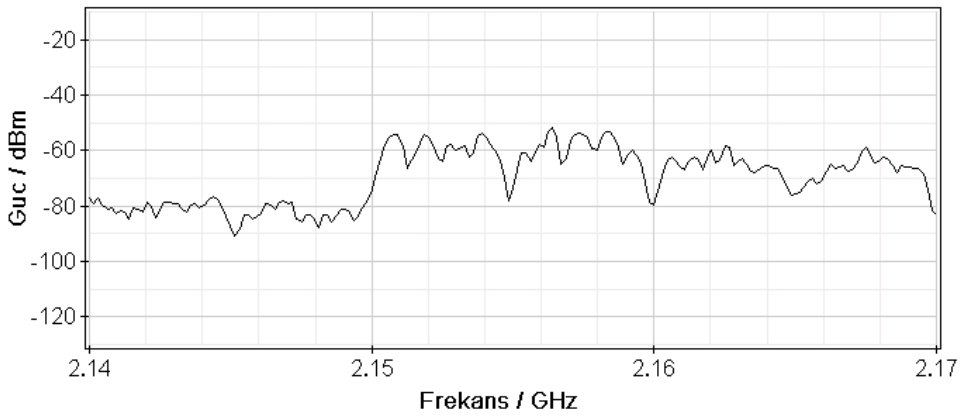

Figure 6.10: Measured received power reading from the spectrum analyzer for DECT.

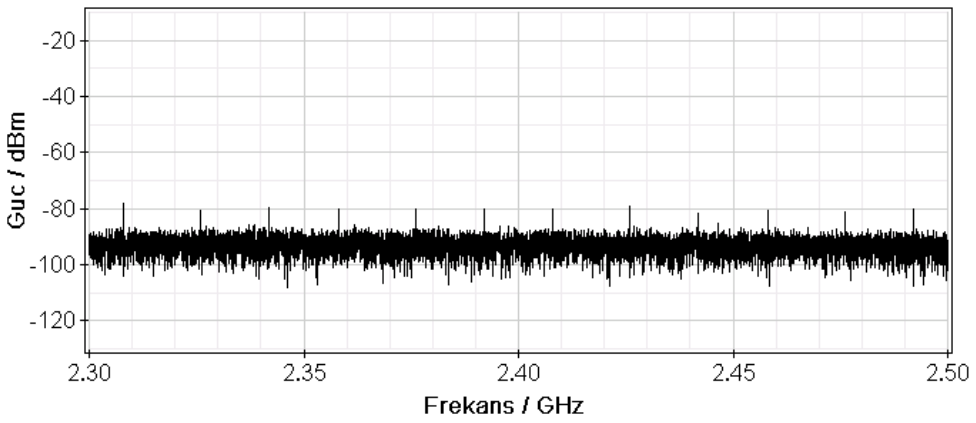

Figure 6.11: Measured received power reading from the spectrum analyzer for WLAN.

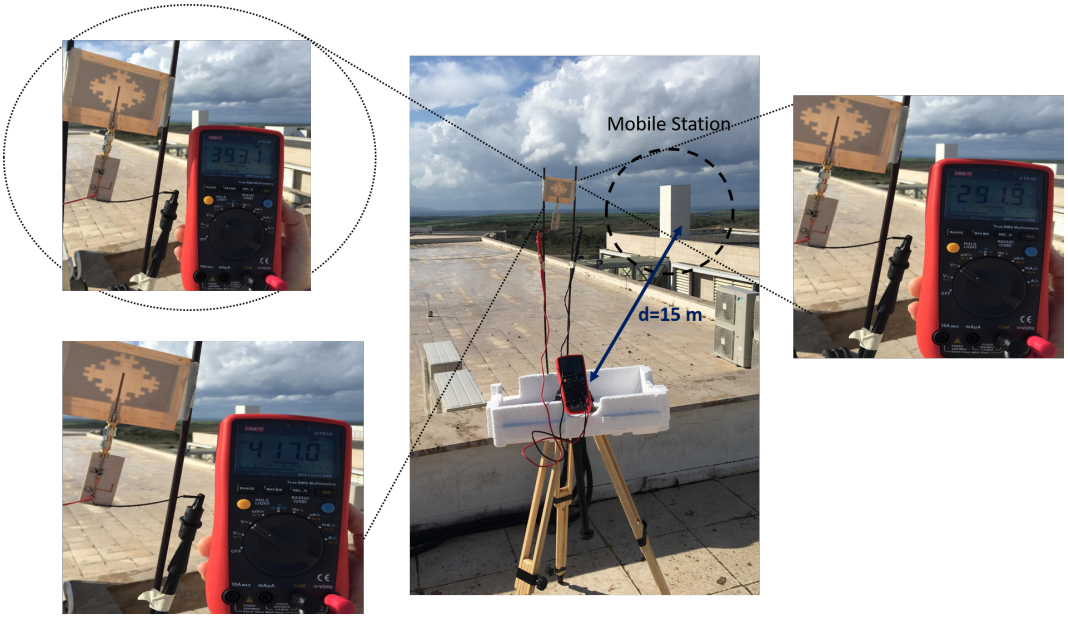

Figure 6.12: Proposed rectenna measurement in ambient at the location of P3.

Table 6.2: Measurement locations and the open voltage values of the proposed rectenna when the measurement duration is approximately 10 min.

Measurement Point	Height	Distance (m)	Open Voltage Value (HSMS2850) (mV)
P1	Ground level	20	9-20
P2	Top of the building	15	50-90
P3	Top of the building	15	195-417
P4	Top of the building	10	45-120

are selected. Figure 6.7 indicates the detailed locations in which the measurements are conducted. The rectenna measurement areas were selected close to the mobile station as shown in Figure 6.7 and the rectenna measurements were conducted at between 13:00-15:00 on the weekend. Figure 6.12 illustrates the measurement setup of the rectenna. The open voltage of the proposed rectenna was measured with UT61D voltmeter at each measurement point, and the output voltage was observed during approximately 10 minutes for each point. Table 6.2 summarizes the open-voltage value for the proposed rectenna at each location. As a result of this, it can be seen that the open-voltage of the rectenna was intermittently changing, and then the highest value was recorded in the range of 417-195 mV at the location of P3.

CHAPTER 7

CONCLUSION AND FUTURE WORK

"Don't be afraid of hard work. Nothing worthwhile comes easily. Don't let others discourage you or tell you that you can't do it. In my day I was told women didn't go into chemistry. I saw no reason why we couldn't "

- Gertrude Elion, *Biochemist, winner of the Nobel Prize*

7.1 Conclusion

In this thesis, a detailed methodology for the design and implementation of an RF energy harvester (rectenna) was presented with numerical and experimental results. The feasibility of the proposed rectenna was investigated and it was shown that designed rectenna can be utilized to actuate a low power sensor.

In the receiving antenna design, it was aimed to study bandwidth enhancement technique. Therefore, a fractal-slotted antenna is proposed to cover the most frequently encountered frequency bands are situated around 1800/1900 MHz, 2.1 GHz, 2.4 GHz, 2.45 GHz corresponding to standards like GSM, UMTS, ISM, WLAN respectively. First of all, the proposed antenna was simulated via ADS, and then antenna with size of 76.99 mm $\times$ 47.45 $\times$ 1.8 mm was fabricated on a Roger4003C substrate. In order to validate the numerical simulations, the return loss, radiation pattern, and gain measurements were carried out. Measurement results demonstrated that the antenna resonates from 1790 MHz to 2930 MHz with the FBW of 48.3% which covers the aforementioned frequency bands. In the antenna design, the bandwidth enhancement was achieved by employing the proposed fractal shape. As a result of the radiation pattern measurements, it was validated that the proposed antenna shows a bi-directional radiation pattern and dual-polarization. The maximum measured gains were found as 2.44 dBi, 2.89 dBi, and 4.43 dBi at the frequencies of 1800 MHz, 2100 MHz, and 2450

MHz, respectively. The only unexpected result was the gain results of the proposed antenna at the frequencies of 1800 MHz and 2100 MHz.

In the rectifier design, a new approach for the realization of a matching network to get an input impedance match at two different frequency of interest was proposed to reduce both the complexity and the losses introduced by a matching network. The proposed rectifier circuit with the proposed matching network with size of 50 mm $\times$ 19 $\times$ 1.8 mm was fabricated on a Roger4003C substrate. In order to validate the numerical simulations, the return loss and the RF-to-DC conversion efficiency measurements were carried out. It was shown with the return loss measurements; the proposed matching network enables a compact rectifying circuit and besides, since the proposed matching network with voltage doubler rectifying circuit resonates at the GSM 1800, and Wi-Fi bands for S_{11} less than -10 dB, the frequency offset approach mentioned in *Chapter 5* was thoroughly validated. Moreover, it was observed that the rectifier circuit yields the RF-to-DC conversion efficiency of 46%, 56%, and 69%, for the different input power levels of -10, -5, 0 dBm, respectively at 1.8 GHz. On the other hand, it features efficiencies of 27%, 38%, and 48%, for the different input power levels of -10, -5, 0 dBm, respectively at 2.45 GHz. The peak conversion efficiency has been recorded as 72.2% at 4 dBm at 1.8 GHz and 53% at 7 dBm at 2.45 GHz. As a result of the conversion efficiency measurements, it was demonstrated that the proposed rectifying circuit provides a good efficiencies in the range of -10 dBm to 0 dBm.

Ultimately, the rectenna which is the combination of both the proposed antenna and the dual-band rectifier circuit has been tested in both controlled environment (laboratory) and ambient. This research has established that the RF-to-DC conversion efficiency of the proposed rectenna can be higher than 50% for the power density level of 11.1 μW/cm^2. Besides, it has been shown that the proposed rectenna can actuate a low–power temperature sensor when the total power density of 15 μW/cm^2 is available from a dedicated source. The feasibility of the proposed rectenna aiming to be utilized to actuate a low power sensor was validated with the measurements. In addition, as a part of this study, the energy harvesting capability of the proposed rectenna has been tested and verified in the Middle East Technical University–Northern Cyprus Campus. As a result of this, it has been observed that the proposed rectenna can feature an open voltage in the range of 195–417 mV in ambient. The ambient measurements have demonstrated that since the available power densities in METU–NCC are low and the available frequency bands are not enough, the one unit of the proposed rectenna was not enough to produce a DC power to actuate an electronic device in ambient.

7.1.1 Thesis Contributions

This thesis study provides a couple of contributions to the field of RF energy harvesting, which can be presented as follows:

1. Chapter 3 discusses the combination of the cavity perturbation technique and the fractal topology to give a better understanding of the effect of the fractal shape on the antenna characteristics. Further, it has demonstrated that the fractal shape slot can be utilized to enhance the bandwidth of the antenna.

2. Chapter 4 presents practical laboratory measurements of different Schottky diodes for the evaluation of how the diode's parameters affect the conversion loss, RF-to-DC conversion efficiency, and output DC voltage. Besides, the practical measurements provide an insight for the selection of the suitable Schottky diode for the sake of RF-to-DC conversion efficiency.

3. Chapter 5 offers a new matching technique for the rectifier circuit to reduce both the complexity and the losses introduced by a matching network. Comprehensive design analysis of the proposed matching network with the rectifier circuit is given in detail.

4. Chapter 6 demonstrates a rectenna which is designed for the first time in the Middle East Technical University–Northern Cyprus Campus. Furthermore, the potential of the RF energy harvesting by using the proposed rectenna has been investigated for the first time in the Middle East Technical University–Northern Cyprus Campus.

7.1.2 Future Work

Below provides a list of several future works to improve the works done in this dissertation, including:

1. Antenna gain enhancement: As expressed in Chapter 3, as the unexpected results in the gain of the proposed antenna at the frequencies of 1800 MHz and 2100 MHz were obtained, gain enhancement methods for the proposed antenna at the frequencies as mentioned earlier may be investigated. For example, an antenna array may be realized with the combination of the proposed broadband fractal antenna to increase the realizable gain.

2. Rectifier band enhancement: As noted in Chapter 5, as the proposed matching network provides dual-band operation at the frequencies of 1.8 GHz and 2.45 GHz, the proposed rectifier circuit does not operate efficiently at the frequency of 2.1 GHz. Therefore, a multi-band rectifier design utilizing the proposed matching network may be implemented in order to enhance the rectifier performance over the frequency of 2.1 GHz.

3. Rectenna architecture enhancement: As given in Chapter 6, the aggregated DC output voltage of the rectenna intermittently changes in ambient conditions. Therefore, in order to keep (or to boost) the DC voltage at a stable level, the integration of the proposed rectenna with a DC-DC step-up converter may be investigated. In addition to this, the proposed rectenna can be realized in an array structure in order to increase the harvested DC power from ambient. Furthermore, as the major challenge associated with RF energy harvesting in METU–NCC is the low RF power density which is available in ambient, the combination of the proposed rectenna with an alternative energy harvester such as solar energy harvester may be investigated. This hybrid energy harvester may be utilized to realize a truly autonomous (battery-less) sensor platforms (electronic devices) in METU–NCC.

REFERENCES

[1] W. C. Brown, "The history of power transmission by radio waves," *IEEE Trans. Microw. Theory Techn.*, vol. MTT-32, pp. 1230-1242, Sept. 1984.

[2] S. Hemour and K. Wu, "Radio-frequency rectifier for electromagnetic energy harvesting: Development path and future outlook," *Proc. IEEE*, vol.102, no. 11, pp. 1667-1691, Nov. 2014.

[3] P. J. Soh, G. A. E. Vandenbosch, M. Mercuri, and D. M. M. P. Schreurs, "Wearable wireless health monitoring," *IEEE Microw. Mag.*, vol.16, no. 4, pp. 55-70, Apr. 2015.

[4] C. Ayyildiz et al., "Structure health monitoring using wireless sensor networks on structural elements," *Ad Hoc Networks 82*, vol.82, no. 4, pp. 68-76, Jan. 2019.

[5] L. Lombardo, S. Corbellini, M. Parvis, A. Elsayed, E. Angelini, S. Grassini, "Wireless sensor network for distributed environmental monitoring," *IEEE Trans. Instrum. Meas.*, vol.67, no. 5, pp. 1214-1122, May 2018.

[6] J. Kimionis et al. , "Zero-Power sensors for smart objects: novel zero-power additively manufactured wireless sensor modules for Iot applications," *IEEE Microw. Mag.*, vol.19, no. 6, pp. 32-47, Sept.-Oct. 2018.

[7] S. Kim, et al. , "Ambient RF energy-harvesting technologies for self-sustainable standalone wireless sensor platforms," *Proc. IEEE* , vol.102, no. 11, pp. 1649-1666, Nov. 2014.

[8] S. Priya and D. J. Inman, *Energy Harvesting Technologies*, vol. 21, New York: Springer, 2009.

[9] M.-L. Ku, W. Li, Y. Chen, and K. J. R. Liu , "Advances in energy harvesting communications: Past, present, and future challenges," *IEEE Commun. Surveys Tut.*, vol.18, no. 2, pp. 1384-1412, 2nd Quart. 2016.

[10] J. A. Paradiso and T. Starner, "Energy scavenging for mobile and wireless electronics," *IEEE Pervasive Comput.*, vol.4, no. 1, pp. 18-27, Jan.-Mar. 2014.

[11] S. Sudevalayam and P. Kulkarni, "Energy harvesting sensor nodes: Survey and implications," *IEEE Commun. Surv. Tuts.*, vol. 13, no. 3, pp. 443-461, 3rd Quart. 2011.

[12] W. S. Wang, T. ODonnell, N. Wang, M. Hayes, B. OFlynn, and C. OMathuna, "Design considerations of sub-mW indoor light energy harvesting for wireless sensor systems," *ACM J. Emerg. Technol.Comput. Syst.*, vol. 6, no. 2, pp. 1-18, Jun. 2010.

[13] P. Gonçalves A. et al, *New Approaches to Thermoelectric Materials. In: Zlati V., Hewson A.C. (eds) Properties and Applications of Thermoelectric Materials*, pp. 51-67, Springer Netherlands, 2009.

[14] V. Leonov, "Thermoelectric energy harvesting of human body heat for wearable sensors," *IEEE Sensors J.*, vol. 13, no. 6, pp. 2284-2291, Jun. 2013.

[15] P. D. Mitcheson, E. M. Yeatman, G. K. Rao, A. S. Holmes, and T. C. Green, "Energy harvesting from human and machine motion for wireless electronic devices," *Proc. IEEE*, vol. 96, no. 9, pp. 1457-1486, Sep. 2008.

[16] L. Xie and M. Cai, "Human motion: Sustainable power for wearable electronics," *Proc. IEEE*, vol. 13, no. 4, pp. 42-49, Oct.-Dec. 2014.

[17] G. Orecchini, L. Yang, M. M. Tentzeris, and L. Roselli, "Wearable battery-free active paper printed RFID tag with human-energy scavenger," *in IEEE MTT-S Int. Microw. Symp. Dig.*, Baltimore, MD, USA, Jun. 2011.

[18] X. Lu, P. Wang, D. Niyato, D. I. Kim, and L. Roselli, "Wireless networks with RF energy harvesting: A contemporary survey," *IEEE Commun. Surv. Tuts.*, vol. 17, no. 2, pp. 757-789, 2nd Quart. 2015.

[19] A. Daga, J. M. Miller, B. R. Long, R. Kacergis, P. Schrafel and J. Wolgemuth, "Electric Fuel Pumps for Wireless Power Transfer: Enabling rapid growth in the electric vehicle market," *IEEE Power Electron. Mag.*, vol. 4, no. 2, pp. 24-35, Jun. 2017.

[20] M. R. Basar, M. Y. Ahmad, J. Cho, and F. B. Ibrahim, "An improved wearable resonant wireless power transfer system for biomedical capsule endoscope," *IEEE Trans. Ind. Electron.*, vol. 65, no. 10, pp. 7772-7781, Oct. 2018.

[21] Y. Zeng, D. Qiu, X. Meng, B. Zhang and S. C. Tang, "Optimized design of coils for wireless power transfer in implanted medical devices," *IEEE J. Electromagn., RF Microw. Med. Biol.* , vol. 2, no. 4, pp. 277-285, Dec. 2018.

[22] J. Bito, J. G. Hester, and M. M. Tentzeris, "Ambient RF energy harvesting from a two-way talk radio for flexible wearable wireless sensor devices utilizing inkjet printing technologies," *IEEE Trans. Microw. Theory Techn.*, vol. 63, no. 12, pp. 4533-4543, Dec. 2015.

[23] H. Ozdemir, T. Nesimoglu, "Microwave energy harvesting by using a broadband fractal antenna and a dual-band rectifier," *18th Mediterranean Microwave Symposium*, pp. 279-282, Nov. 2018, Istanbul, Turkey.

[24] X. Gu, S. Hemour, L. Guo, and K. Wu, "Integrated cooperative ambient power harvester collecting ubiquitous radio frequency and kinetic energy," *IEEE Trans. Microw. Theory Techn.*, vol. 66, no. 9, pp. 4178-4190, Sep. 2018.

[25] J. Bito, R. Bahr, J. G. Hester, S. A. Nauroze, A. Georgiadis, and M. M. Tentzeris, "A novel solar and electromagnetic energy harvesting system with a 3-D printed package for energy efficient Internet-of-Things wireless sensors," *IEEE Trans. Microw. Theory Techn.*, vol. 65, no. 5, pp. 1831-1842, May 2017.

[26] R. J. Vyas, B. S. Cook, Y. Kawahara, and M. M. Tentzeris, "E-WEHP: A batteryless embedded sensor-platform wirelessly powered from ambient digital-TV signals," *IEEE Trans. Microw. Theory Tech.*, vol. 61, no. 6, pp. 2491-2505, Jun. 2013.

[27] M. Pinuela, P. D. Mitcheson, and S. Lucyszyn, "Ambient RF energy harvesting in urban and semi-urban environment," *IEEE Trans. Microw. Theory Tech.*, vol. 61, no. 7, pp. 2715-2726, Jul. 2013.

[28] C. Song, Y. Huang, J. Zhou, S. Yuan, Q. Xu, and P. Carter, "A broadband efficient rectenna array for wireless energy harvesting," *9th European Conference on Antennas and Propagation*, pp. 2164–3342, Aug. 2015, Lisbon, Portugal.

[29] K. Mimis , D. R. Gibbins, S. Dumanli, G. T. Watkins, "The ant and the elephant: ambient RF harvesting from the uplink," *IET Microw., Antennas Propag.*, vol. 11, no. 3, pp. 3865-393, Apr. 2017.

[30] U. Muncuk, K. Alemdar, J. D. Sarode, and K. R. Chowdhury, "Multiband ambient RF energy harvesting circuit design for enabling batteryless sensors and IoT," *IEEE Internet Things J.*, vol. 5, no. 4, pp. 2700-2714, Aug. 2018.

[31] Z. Harouni, L. Cirio, L. Osman, A. Gharsallah, and O. Picon, "A dual circularly polarized 2.45-GHz rectenna for wireless power transmission," *IEEE Antennas Wireless Propag. Lett.*, vol. 10, pp. 306-309, 2011.

[32] B. Strassner and K. Chang, "5.8-GHz circularly polarized rectifying antenna for wireless microwave power transmission," *IEEE Trans. Microwave Theory Tech.*, vol. 50, no. 8, pp. 1870-1876, Aug. 2002.

[33] K. Niotaki et al., "A compact dual-band rectenna using slot-loaded dual band folded dipole antenna," *IEEE Antennas Wireless Propag. Lett.*, vol. 12, pp. 1634-1637, 2013.

[34] Y.-J. Ren, M. F. Farooqui, and K. Chang, "A compact dual-frequency rectifying antenna with high-orders harmonic-rejection," *IEEE Trans. Antennas Propag.*, vol. 55, no. 7, pp. 2110-2113, Jul. 2007.

[35] H. Sun, Y.-X. Guo, M. He, and Z. Zhong, "A dual-band rectenna using broadband yagi antenna array for ambient RF power harvesting," *IEEE Antennas Wireless Propag. Lett.*, vol. 12, pp. 918-921, 2013.

[36] S. Shen, C.-Y. Chiu, and R. D. Murch, "A dual-port triple-band L-probe microstrip patch rectenna for ambient RF energy harvesting," *IEEE Antennas Wirless Propag. Lett.*, vol. 17, pp. 3071-3074, 2007.

[37] V. Kuhn, C. Lahuec, F. Seguin, and C. Person, "A multi-band stacked RF energy harvester with RF-to-DC efficiency up to 84%," *IEEE Trans. Microw. Theory Techn.*, vol. 63, no. 5, pp. 1768-1778, May 2015.

[38] C. Song et al, "A novel six-band dual CP rectenna using improved impedance matching technique for ambient RF energy harvesting," *IEEE Trans. Antennas Propag.*, vol. 64, no. 7, pp. 3160-3171, Jul. 2016.

[39] K. M. Mak, H. W. Lai, and K. M. Luk, "A 5G wideband patch antenna with antisymmetric L-shaped probe feeds," *IEEE Trans. Antennas Propag.*, vol. 66, no. 2, pp. 957-961, Feb. 2018.

[40] P. A. Dzagbletey and Y.-B. Jung, "Stacked microstrip linear array for millimeter-wave 5G baseband communication," *IEEE Antennas Wireless Propag. Lett.*, vol. 17, no. 5, pp. 780-783, May 2018.

[41] S. Lemey, S. Agneessens, P. Van Torre, K. Baes, J. Vanfleteren, and H. Rogier, "Wearable flexible lightweight modular RFID tag with integrated energy harvester," *IEEE Trans. Microw. Theory Techn.*, vol. 64, no. 7, pp. 2304-2314, Jul. 2016.

[42] X. Liu, Y. Liu, and M. M. Tentzeris, "A novel circularly polarized antenna with coin-shaped patches and a ring-shaped strip for worldwide UHF RFID applications," *IEEE Antennas Wireless Propag. Lett.*, vol. 14, pp. 707-710, Sep. 2015.

[43] T. Karacolak, R. Cooper, J. Butler, S. Fisher, and E. Topsakal, "In vivo verification of implantable antennas using rats as model animals," *IEEE Antennas Wireless Propag. Lett.*, vol. 9, pp. 334-337, Apr. 2010.

[44] C. Liu, Y. X. Guo, and S. Xiao, "Capacitively loaded circularly polarized implantable patch antenna for ISM-band biomedical applications," *IEEE Trans. Antennas Propag.*, vol. 62, no. 5, pp. 2407-2417, May 2014.

[45] K. Zhang et al., "A conformal differentially fed antenna for ingestible capsule system," *IEEE Trans. Antennas Propag.*, vol. 66, no. 4, pp. 1695-1703, Apr. 2018.

[46] N. Wang, L. Talbi, Q. Zeng., "Wideband fabry-perot resonator antenna with electrically thin dielectric superstrates," *IEEE Access*, vol. 6, pp. 14966-14973, Apr. 2018.

[47] S. X. Ta and T. K. Nguyen, "AR bandwidth and gain enhancement of patch antenna using single dielectric superstrate," *Electron. Lett.*, vol. 53, no. 15, pp. 1015-1017, Jul. 2017.

[48] M. Asaadi and A. Seba, "Gain and bandwidth enhancement of 2×2 square dense dielectric patch antenna array using a holey superstrate," *IEEE Antennas Wireless Propag. Lett.*, vol. 16, pp. 1808-1811, 2017.

[49] D. Sarkar and K. V. Srivastava, "A compact four-element MIMO/diversity antenna with enhanced bandwidth," *IEEE Antennas Wireless Propag. Lett.*, vol. 16, pp. 2469-2472, 2017.

[50] S. Shi, W. Che, W. Yang, and Q. Xue, "Miniaturized patch antenna with enhanced bandwidth based on signal-interference feed," *IEEE Antennas Wireless Propag. Lett.*, vol. 14, pp. 281-284, 2015.

[51] L.-J. Xu, Y.-X. Guo, "Bandwidth enhancement of an implantable antenna," *IEEE Antennas Wireless Propag. Lett.*, vol. 14, pp. 1510-1513, 2015.

[52] J. Yeo and J.-I. Lee, "Bandwidth enhancement of double–dipole, quasi yagi antenna using stepped slotline structure," *IEEE Antennas Wireless Propag. Lett.*, vol. 15, pp. 694-697, 2016.

[53] A. Petosa and A. Ittipiboon, "Dielectric resonator antennas: A historical review and the current state of the art," *IEEE Antennas Propag. Mag.*, vol. 52, no. 5, pp. 91-116, Oct. 2010.

[54] K. B. Ng, C. H. Chan, H. Zhang, and G. Zeng, "Bandwidth enhancement of planar slot antenna using complementary source technique for millimeter-wave applications," *IEEE Trans. Antennas Propag.*, vol. 62, no. 9, pp. 4452-4458, Sep. 2014.

[55] H.-Y. Zhang, F.-S. Zhang, F. Zhang, T. Li, and C. Li, "Bandwidth enhancement of a horizontal polarized omnidirectional antenna by adding parasitic strips," *IEEE Antennas Wireless Propag. Lett.*, vol. 16, pp. 880-883, Sept. 2016.

[56] Y. Cui , L. Wu, and R. Li, "Bandwidth enhancement of a broadband dual-polarized antenna for 2G/3G/4G and IMT base stations," *IEEE Trans. Antennas Propag.*, vol. 66, no. 12, pp. 7368-7373, Dec. 2018.

[57] J.-Y. Sze and K.-L. Wong, "Bandwidth enhancement of a microstrip-line-fed printed wide-slot antennas," *IEEE Trans. Antennas Propag.*, vol. 49, no. 7, pp. 1020-1024, Jul. 2001.

[58] Y. F. Liu, K. L. Lau, Q. Xue, and C. H. Chan, "Experimental studies of printed wide-slot antenna for wide-band applications," *IEEE Antennas Wireless Propag. Lett.*, vol. 3, pp. 273-275, 2004.

[59] K.-R. Chen, C. Sim, and J.-S. Row, "A compact monopole antenna for super wideband applications," *IEEE Antennas Wireless Propag. Lett.*, vol. 10, pp. 488-491, May 2011.

[60] H. D. Chen, "Broadband CPW-fed square slot antennas with a widened tuning stub," *IEEE Trans. Antennas Propag.*, vol. 51, no. 8, pp. 1982-1986, Aug. 2003.

[61] C. A. Balanis, *Antenna Theory: Analysis and Design*. John Wiley & Sons, 2016.

[62] H. Peitgen, H. Jürgens, and D. Saupe, *Chaos and fractals: new frontiers of science*. Springer Science & Business Media, 2006.

[63] B. Ghosh, S. N. Sinha, and M. V. Kartikeyan, *Fractal Apertures in Waveguides, Conducting Screens and Cavities: Analysis and Design.*, vol. 187 Springer, 2014.

[64] D. M. Pozar, "Microstrip antennas," in *Proc. IEEE*, vol. 80, no. 1, pp. 79–91, 1992.

[65] M. C. Bailey and W. F. Croswell, "Pattern measurements of slot radiators in dielectric-coated metal plates," *IEEE Trans. Antennas Propag.*, vol. 15, pp. 824-826, Nov. 1967.

[66] C. A. Balanis, *Advanced Engineering Electromagnetics*. John Wiley & Sons, 1989.

[67] L. B. Felsen, "Radiation from a tapered surface wave antenna," *IEEE Trans. Antennas Propag.*, vol. 8, pp. 577-586, Nov. 1960.

[68] R. F. Harrington, *Time–Harmonic electromagnetic fields*. John Wiley & Sons–IEEE, 2001.

[69] D. H. Werner and S. Ganguly, "An overview of fractal antenna engineering research," *IEEE Antennas Propag. Mag.*, vol. 45, no. 1, pp. 38-56, Feb. 2003.

[70] C. Song, Y. Huang, J. Zhou, J. Zhang, S. Yuan, and P. Carter, "A high efficiency broadband rectenna for ambient wireless energy harvesting," *IEEE Trans. Antennas Propag.*, vol. 63, no. 8, pp. 3486-3495, Aug. 2015.

[71] D. M. Pozar, *Microwave engineering*. John Wiley & Sons, 2009.

[72] S. M. Sze and K. Ng. Kwok, *Physics of semiconductor devices*. John Wiley & Sons, 2006.

[73] R. Cory, *Schottky diodes*. Skyworks Solutions, Inc., pp. 1-5, Feb. 2009.

[74] S. A. Maas, *The RF and microwave circuit design cookbook*. Boston, MA: Artech House, 1998.

[75] S. J. Moloi and M. McPherson, "Capacitance–voltage behaviour of schottky diodes fabricated on p-type silicon for radiation–hard detectors," *Radiat. Phys. Chem.*, vol. 85, pp. 73-82, 2013.

[76] *Agilent HSMS-285x Series Surface Mount Zero Bias Schottky Detector Diodes, Data Sheet.* Agilent Technologies, Inc., Sept. 2005.

[77] *Principles, Applications and Selection of Receiving Diodes, Data Sheet.* M/A-COM Technology Solutions Inc.

[78] *The schottky diode mixer, Application Note 995.* Hewlett-Packard Co., U.S.A., 1986.

[79] R. Ludwig and P. Bretchko, *RF circuit design, theory and applications.* Upper Saddle River, NJ: Prentice-Hall, 2000.

[80] T. Doi, "On large signal frequency domain analysis of circuits containing junction diodes and bipolar transistors," *IEEE Trans. Circuits Syst.*, vol. CAS–24, no. 6, pp. 329-341, Jun. 1977.

[81] A. Boaventura, A. Collado, N. B. Carbalho, and A. Georgiadis, "Optimum behavior: Wireless power transmission system design through behavioral models and efficient synthesis techniques," *IEEE Microw. Mag.*, vol. 14, no. 2, pp. 26-35, Mar. 2013.

[82] *Dynamic Range Extension of Schottky Detectors, Application Note 956-5.* Agilent Technologies, Inc., 1999.

[83] Mini Circuit, " High power bi-directional coupler," *BDCA-10-25 datasheet*.

[84] T. Yoo and K. Chang, "Theoretical and experimental development of 10 and 35 GHz rectennas," *IEEE Trans. Microw. Theory Tech.*, vol. 40, no. 6, pp. 1259-1266, Jun. 1992.

[85] E. Falkenstein, "Characterization and design of a low-power wireless power delivery system," *Ph.D. dissertation, Dept. Electr., Comput. Energy Eng., Univ. Colorado Boulder*, Boulder, CO, USA, Jan. 2012.

[86] M. Abramowitz and I. Stegun, Eds., *Handbook of mathematical functions with formulas, graphs, and mathematical tables*, 9th ed. National Bureau of Standards, 1970.

[87] *Harmonic Balance Simulator.* Agilent Technologies, Inc.

[88] Q. W. Lin and X. Y. Zhang, "Differential rectifier using resistance compression network for improving efficiency over extended input power range," *IEEE Trans. Microw. Theory Techn.*, vol. 64, no. 9, pp. 2943-2954, Sept. 2016.

[89] R. E. Collin, *Foundations for microwave engineering*, John Wiley & Sons–IEEE, 2001.

[90] C. Song et al., "Matching network elimination in broadband rectennas for high-efficiency wireless power transfer and energy harvesting," *IEEE Trans. Ind. Electron.*, vol. 64, no. 5, pp. 3950-3961, May 2017.

[91] N.-C. Kuo, C.-N. Chiu, H.-C. Hsieh, and J.-S. Chen,"Radiation minimization of single-stub microstrip impedance transformers," *IEEE Trans. Microw. Theory Techn.*, vol. 61, no. 3, pp. 1018-1029, Mar. 2013.

[92] R. Fano,“Theoretical limitations on the broad–band matching of arbitrary impedances,” *Research Laboratory Of Electronics Massachusetts Institute Of Technology*, Technical Report No. 41, Jan. 1948.

[93] Yong Huang, N. Shinohara, H. Toromura, “A wideband rectenna for 2.4 GHz–band RF energy harvesting,” *IEEE Wireless Power Transfer Conference*, pp. 1-3, May 2016, Aveiro, Portugal.

[94] H. Sun, Y.-X. Guo, M. He, and Z. Zhong,“Design of a high–efficiency 2.45-GHz rectenna for low-input–power energy harvesting,” *IEEE Antennas Wireless Propag. Lett.*, vol. 11, pp. 929-932, Aug. 2012.

[95] T. Le, K. Mayaram, and T. Fiez,“Efficient far–field radio frequency energy harvesting for passively powered sensor networks,” *IEEE J. Solid-State Circuits*, vol. 43, no. 5, pp. 1287-1302, May 2008.

PROGRAM

Sustainable Environment And Energy Systems **(SEES)** ☐

Political Science and International Relations (**PSIR**) ☐

English Language Teaching (**ENLT**) ☐

Electrical and Electronics Engineering (**EEE**) ☐

Computer Engineering (**CNG**) ☐

Mechanical Engineering (**MECH**) ☐

YAZARIN / AUTHOR

Soyadı / Surname: .....

Adı / Name: .....

Bölümü / Department: .....

TEZİN ADI / TITLE OF THE THESIS (**İngilizce** / English): .....

.....

TEZİN TÜRÜ / DEGREE:

Yüksek Lisans / Master ☐

Doktora / PhD ☐

1.Tezimin tamamından kaynak gösterilmek şartıyla fotokopi alınabilir. ☐

2.Tezimin içindekiler sayfası, özet, indeks sayfalarından ve/veya bir bölümünden kaynak gösterilmek şartıyla fotokopi alınabilir. ☐

3.Tezimden bir (1) yıl süreyle fotokopi alınamaz. ☐

Yazarın imzası/ Signature ..... **Tarih** /Date .....